Master's thesis

Dynamics of transversal patterns in optical micro-cavities

Submitted by

Prapti Pal

March 27, 2023

First examiner
PD Dr. Svetlana Gurevich

Second examiner
Dr. Julien Javaloyes

Westfälische Wilhelms-Universität Münster
Fachbereich Physik
Institut für Theoretische Physik

Contents

1 Introduction

Light waves are electromagnetic radiation that consists of spatially-varying electromagnetic field, traveling in the propagation direction, carrying momentum and energy [1]. The transverse field direction refers to the plane perpendicular to the field propagation, whereas longitudinal field direction is the plane of field propagation. Within an optical cavity, both transverse and longitudinal modes are induced.

Structures that enable confinement of light in micro-scale volumes are called optical micro-cavities [2]. Due to finite size of the spatial dimensions in micro-cavities, specific optical effects act on the optical field. Optical cavities that allow for circulation of a beam of light in a closed path are called optical resonators [2]. In a resonator, due to the wave nature of light, longitudinal standing modes are induced that may interact with each other. Another type of optical micro-cavity constricts light beams in the transverse dimension only, allowing for longitudinal propagation, e.g., optical fibers [3].

In optical fibers, the dynamics of the optical pulse propagation is governed by the effects of dispersion and Kerr nonlinearity [4]. Dispersion is a characteristic of the fiber medium which causes different spectral components of pulse propagation to travel at different speeds in the medium, leading to pulse broadening in certain frequency ranges. Whereas, the nonlinear dependence of the refractive index on the pulse intensity, called Kerr nonlinearity, is induced at high intensity regime and leads to phase modulation of the pulse. The interplay between these two effects leads to the formation of shape-preserving optical pulses called solitons in the conservation system with negligible fiber losses [4].

Additional effects of higher order dispersion into this optical system have been investigated recently [5, 6, 7, 8] both analytically as well as experimentally. In this thesis, the effects of quadratic and quartic dispersion along with Kerr nonlinearity are investigated.

In laser micro-cavities, however, the light matter interaction within the active components in the micro-cavity, e.g., gain medium or nonlinear optical absorbers, causes the nonlinear response, while the spatial coupling is largely dependent on the effects of diffraction and diffusion. For lasing action, the optical micro-cavity acts as a resonator, introducing diffractive effects due to finite size as well as cavity losses with each round-trip within the resonator leading to a dissipative system.

One such laser configuration is investigated in this thesis, called Mode-Locked Integrated External-Cavity Surface-Emitting Laser (MIXSEL), where a micro-cavity with integrated nonlinear absorber is externally coupled to a feedback cavity. The spatial distribution of the laser field in a ring configuration micro-cavity, dependent on the effects of diffraction and field diffusion, resulted in the presence of localized structures called Light Bullets were found [9]. In this thesis, the induced instability due to the weak aberrations, approximated by an additional Bilaplacian term, and nonlinearity is studied. Additionally, a potential is considered on the system domain that acts as a wavefront curvature to the field within the micro-cavity.

Formation of transverse patterns in nonlinear optical systems is caused due to spontaneous symmetry breaking leading to spontaneous emergence of spatial order [10]. The combined effects of spatial coupling and self-focusing nonlinearity at certain parameter regimes which induces instability in the system leads to spontaneous pattern formation. The role of nonlinearity generally includes selection of the type of patterns induced in the domain out of various different possibilities, whereas the inhomogeneous spatial distribution is due to spatial coupling, e.g., diffraction, dispersion etc. in optical systems. The stability of these periodic structures is dependent on the geometric as well as intrinsic symmetries of optical interactions.

Such nonlinear optical micro-cavities can be theoretically modeled using nonlinear partial differential equations to analyze the solutions and their stability in the dynamical system. Dynamical system equations of this type are usually studied using numerical methods. Direct numerical analysis is one method that can be used to solve the system equation numerically to examine steady state and dynamical solutions of the system. Another approach is path continuation and bifurcation analysis that allows for studying the evolution of steady state solutions in the control parameter space.
In this thesis, both numerical methods are presented to analyze dynamical systems of two types of optical micro-cavities and different forms of transversal patterns that might emerge in the system solutions. In Chapter 2, the theoretical models for two optical micro-cavities are described, along with the numerical methods used to study these nonlinear dynamical systems and their implementations. Chapter 3 presents the analysis and continuation results of the solutions to the Quartic Dispersion Nonlinear Schrödinger equation. The formation of transversal patterns as oscillating tails in the soliton-like solutions is investigated in parameter space and their stability is analyzed. In Chapter 4, the analytical solutions of the MIXSEL model equation are presented and the dynamics of transversal patterns of these solutions are detailed. Linear stability of this equation is presented in Chapter 5, as well as induced instability in the system that leads to formation of transversal patterns in the one-dimensional spatial domain. Finally, the transverse spatial pattern solutions of the MIXSEL model equation in two-dimensions is presented in Chapter 6.

2 Theoretical Concepts

2.1 Theoretical Modeling of Optical Micro-Cavities

2.1.1 Generalized Nonlinear Schrödinger Equation

The propagation of nonlinear optical pulses in optical fibers for a slowly-varying complex pulse envelope of the electric field $\psi = \psi(\tau, z)$ which modulates the underlying carrier wave is described by the Nonlinear Schrödinger Equation (NLSE) [4]

$$\frac{\partial \psi}{\partial z} + i\,\frac{\beta_2}{2}\,\frac{\partial^2 \psi}{\partial \tau^2} - i\,\gamma \mid \psi \mid^2 \psi = 0, \tag{2.1}$$

where τ is the retarded time in the frame of the pulse, z is the propagation distance, β_2 is the quadratic dispersion or group velocity dispersion parameter and γ is the Kerr nonlinearity parameter. The quadratic dispersion parameter β_2 is obtained by the Taylor expansion of the dispersion relation $\beta(\omega)$ around the carrier frequency ω_0 of the pulse envelope $\psi(\tau, z)$ as

$$\beta(\omega) = \beta_0 + (\omega - \omega_0)\beta_1 + \frac{1}{2}(\omega - \omega_0)^2\beta_2 + \frac{1}{6}(\omega - \omega_0)^3\beta_3 + \frac{1}{24}(\omega - \omega_0)^4\beta_4 + ..., \tag{2.2}$$

where

$$\beta_m = \left(\frac{\mathrm{d}^m \beta}{\mathrm{d}\omega^m}\right)\Bigg|_{\omega=\omega_0} \quad (\text{for } m = 1, 2, ...). \tag{2.3}$$

For the NLSE (2.1), in the retarded frame, the higher order dispersion terms ($m = 3, 4, ..$) are assumed to be negligible due to finite spectral width. Equation (2.1) has bright soliton solutions [4] for anomalous quadratic dispersion $\beta_2 < 0$ with positive Kerr nonlinearity $\gamma > 0$ that maintain their shape upon propagation of the form

$$\psi(\tau, z) = \sqrt{\frac{2\mu}{\gamma}}\,\mathrm{sech}\left(\frac{2\mu}{\mid \beta_2 \mid}\tau\right)\exp\{i\mu z\}, \tag{2.4}$$

where parameter μ is the rate of change of phase due to nonlinearity that vary the peak powers and widths of each soliton solution. This parameter is also referred to as the energy or the chemical potential coefficient. Similarly, experimentally observed Pure Quartic Solitons (PQS) in a photonic crystal waveguide at a carrier frequency, where quadratic dispersion parameter β_2 and cubic dispersion parameter β_3 were negligible, leading order of dispersion being quartic β_4, were also confirmed [7].
The Quartic Dispersion Nonlinear Schrödinger Equation (QDNLSE) extends the Nonlinear Schrödinger Equation for high-intensity nonlinear pulses by adding an additional quartic dispersion term β_4 obtained by the Taylor expansion of the dispersion relation in (2.2)

$$\frac{\partial \psi}{\partial z} + i\,\frac{\beta_2}{2}\,\frac{\partial^2 \psi}{\partial \tau^2} - i\,\frac{\beta_4}{24}\,\frac{\partial^4 \psi}{\partial \tau^4} - i\,\gamma \mid \psi \mid^2 \psi = 0, \tag{2.5}$$

where $\beta_3 = 0$.
Analytical solutions of this equation for $\beta_2 < 0$, $\beta_4 < 0$ and $\gamma = 1.0$ was reported by Karlsson and Höök [11] :

$$\psi(\tau, z) = 3\sqrt{\frac{{\beta_2}^2}{5 \mid \beta_4 \mid}}\,\mathrm{sech}^2\left(\sqrt{\frac{3{\beta_2}^2}{5 \mid \beta_4 \mid}}\tau\right)\exp\left\{i\frac{24{\beta_2}^2}{25 \mid \beta_4 \mid}z\right\}. \tag{2.6}$$

This represents a family of solutions corresponding to a fixed peak power, width and

$$\mu = \frac{24{\beta_2}^2}{25 \mid \beta_4 \mid}, \tag{2.7}$$

where μ is a free parameter. The Karlsson and Höök family of solutions (2.6) are a part of a general super-family of solutions of Eq. (2.5) called the Generalized Dispersion Kerr Solitons (GDKS) [12]. The solutions of Eq. (2.5) in the $\beta_2 > 0$ and $\beta_4 < 0$ parameter regime is later investigated in detail.

2.1.2 MIXSEL Model Equation

The Mode-Locked Integrated External-Cavity Surface-Emitting Laser (MIXSEL) is a type of saturable absorber-gain integrated Surface-Emitting Laser that allows for passive mode-locking in a micro-cavity setup coupled to an external cavity [13]. A model of an integrated micro-cavity of Distributed Bragg Reflectors (DBRs) coupled to an external cavity that is used for describing the theoretical model in the following is shown in Fig. 2.1.

Mode-locking in a laser refers to the phenomenon where the induced oscillating longitudinal modes within the laser resonator cavity develop a fixed definite phase relationship between each other [14]. One method for achieving mode-locking is passive mode-locking where, usually, a saturable absorber, with short upper state life-time, is used which exploits the nonlinear effects of saturation.

The Haus master equation [15] for Passive Mode-Locking, adapted to the long cavity limit dynamics [16, 17], describes the slow evolution of the three dimensional intra-cavity field $E(r_\perp, t, \theta)$ due to the dynamics of the population inversion in the gain medium N_1 and saturable absorber N_2 as

$$\frac{\partial E}{\partial \theta} = [(1 - i\alpha_1)N_1 + (1 - i\alpha_2)N_2 - k + \mathcal{L}]\, E, \tag{2.8}$$

$$\frac{\partial N_1}{\partial t} = \gamma_1[J_1(r_\perp) - N_1] - N_1 \mid E \mid^2, \tag{2.9}$$

$$\frac{\partial N_2}{\partial t} = \gamma_2(J_2 - N_2) - sN_2 \mid E \mid^2 . \tag{2.10}$$

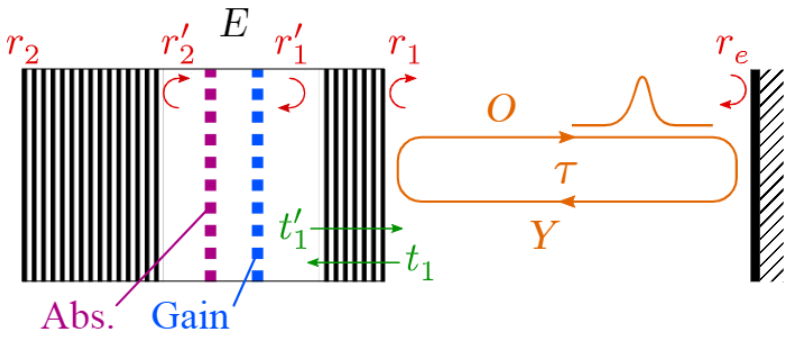

Figure 2.1: A micro-cavity of Distributed Bragg Reflectors (DBRs) with a gain medium (blue) and a saturable absorber (purple) coupled to an external cavity output mirror [18].

Here, $t \in [0, \tau]$ represents the round-trip time in the external cavity with τ being the time taken for one round-trip, θ is another dimensionless time scale normalized to τ,

corresponding to the slow evolution of the temporal profile under the combined effects of gain, absorption and spatio-temporal filtering and the two transverse dimensions are $r_\perp = (x, y)$. The parameter k is the round-trip cavity losses while $\alpha_{1,2}$ are the line-width enhancement factors of the gain and absorber, respectively, that relax with time-scales $\gamma_{1,2}^{-1}$ towards the current $J_{1,2}$. The saturation parameter s is the ratio of saturation fluence of the absorber to the gain. Spatially localized optical pumping is taken into account by the spatial dependence of $J_1(r_\perp) > 0$ while saturable absorption is obtained using $J_2 < 0$.

In the long cavity limit, the spatio-temporal distribution of the carriers $N_{1,2}(r_\perp, t)$ is dependent on the evolution of the optical field $E(r_\perp, t, \theta)$ and, therefore, are not explicitly dependent on the normalized time-scale θ. In this case, it can be assumed that a full recovery of the carriers between pulses takes place, i.e., $\gamma_{1,2}\tau \gg 1$. Hence, the Dirichlet condition $N_1(r_\perp, 0) = J_1(r_\perp)$ and $N_2(r_\perp, 0) = J_2$ can be applied for each round-trip in the cavity. Since the intra-cavity field $E(r_\perp, t, \theta)$ is spatio-temporally localized in the cavity, periodic boundary conditions can be used in the variables $(r_\perp, t)$.

For the effective cavity spatio-temporal linear operator $\mathcal{L}$, the Fresnel Transform [19] method is used to analytically calculate the transverse effects occurring at each round-trip from the full round-trip Gauss ABCD matrix of the two micro-cavities in Fig. 2.1, which includes diffraction and wavefront curvature incurred due to the quasi-4F cavity telescope as well as the diffraction and thermal lensing (in the parabolic approximation) that takes place in the micro-cavities. Additionally, the influence of weak spherical aberrations are also considered due to the presence of wider angular distributions of the optical fields at collimator lenses with short focal lengths.

In an optical setup, the self-imaging condition is met when a single round-trip through the optical cavity results in the feedback mirror out-coupling aperture to be imaged at its own plane. Deviation from this condition by introducing a small transversal offset to the system results in an unstable cavity with diffraction losses. In this model, close to self-imaging condition is taken into account, with the effects of the wavefront curvature, diffraction as well as the spherical aberrations as small perturbations to the field profile at each round-trip. Hence, in the limit of quasi self-imaging, and considering temporal diffusion d_f due to finite bandwidth of gain curve of the micro-cavities, the effective linear operator $\mathcal{L}$ reads

$$\mathcal{L} = d_f \frac{\partial^2}{\partial t^2} + \mathcal{L}_\perp, \tag{2.11}$$

$$\mathcal{L}_\perp = i\tilde{C} r_\perp^2 + \left(d + i\tilde{B}\right) \nabla_\perp^2 + iS\nabla_\perp^4. \tag{2.12}$$

A real transverse diffusion parameter d accounts for the finite size of the lenses and the numerical aperture of the optical system that penalizes high transverse spatial frequencies. The parameters for effective wavefront curvature $\tilde{C}$, the effective diffraction $\tilde{B}$ and aberration parameter S are given by the following relations

$$\tilde{C} = \frac{\pi}{\lambda} C \frac{h\eta}{(1+\eta)^2} \tag{2.13}$$

$$\tilde{B} = \frac{\lambda B}{4\pi} \frac{h\eta}{(1+\eta)^2} + l_{1,\perp}^2 + l_{2,\perp}^2, \tag{2.14}$$

$$S = \left(\frac{\lambda}{2\pi}\right)^3 \sigma {f_0}^2, \tag{2.15}$$

where h is intra-cavity coupling parameter related to the reflectivities of the two micro-cavity mirrors, η is the out-coupling feedback mirror reflectivity, λ is the wavelength, $l_{1,2,\perp}$ are the normalized micro-cavity diffraction lengths, σ is a small aberration coefficient at short focal length f_0, and the coefficients B, C are obtained from the ABCD matrix of the micro-cavity.
New's method [20] of Passive Mode-Locking exploits the scale separation between pulse evolution, the fast stage in which stimulated emission is dominant and the slow stage that is controlled by the gain recovery process. Under the strong approximation that the spatio-temporal profile $E(r_\perp, t, \theta)$ can be factored as

$$E(r_\perp, t, \theta) = A(r_\perp, \theta)p(t), \tag{2.16}$$

where $p(t)$ is a normalized temporal profile that corresponds to Temporal Localized States (TLS) [21]. Therefore, using the Eqs. (2.8) and (2.12), one obtains an approximate equation for the slow evolution of the transverse profile $A(r_\perp, \theta)$ as

$$\begin{aligned}\frac{\partial A}{\partial \theta} = \Big[(1 - i\alpha_1)\, J_1\, g\,(\mid A \mid^2) \;+\; (1 - i\alpha_2)\, J_2\, g\,(s \mid A \mid^2) \;-\; k \;+\; i\tilde{C} r_\perp^2 \\ +\; \left(d + i\tilde{B}\right) \nabla_\perp^2 \;+\; iS\nabla_\perp^4 \Big] A,\end{aligned} \tag{2.17}$$

where J_1 and J_2 are the current biases of the gain and absorber respectively. Here, the fact that the stimulated terms are dominant in Eqs. (2.8), (2.9) and (2.10) during emission is utilized to yield the exponential terms in the nonlinear response function of the two active media to a pulse P

$$g(P) = \frac{1 - \exp\{-P\}}{P}. \tag{2.18}$$

Equation (2.17) forms the MIXSEL model PDE for analysis of transversal dynamics of passively mode-locked integrated semiconductor laser micro-cavities at the limit of quasi self-imaging.
For a spatially uniform pumping profile, the gain bias $J_1(r_\perp) = J_1$ and is no longer dependent on the transverse dimensions, given for a pulse P as

$$J_1(P) = \frac{k - J_2\, g(sP)}{g(P)}. \tag{2.19}$$

The threshold bias of the gain, J_{th} is reached when the nonlinear response function in Eq. 2.18 approaches $g(P) \to 1$ at saturation and is given by the following relation

$$J_{th} = k - J_2 = 1 - \frac{h\eta}{1 + \eta} - J_2. \tag{2.20}$$

The effective cavity losses parameter k is given by

$$k = 1 - \frac{h\eta}{1 + \eta}. \tag{2.21}$$

The equivalent 1D MIXSEL model equation is given by

$$\begin{aligned}\frac{\partial A}{\partial \theta} = \Big[(1 - i\alpha_1)\, J_1\, g\,(\mid A \mid^2) \;+\; (1 - i\alpha_2)\, J_2\, g\,(s \mid A \mid^2) - \; k \\ +\, i\,\tilde{C}\, x^2 \;+\; \left(d + i\tilde{B}\right) \frac{\partial^2}{\partial x^2} \;+\; i\, S\, \frac{\partial^4}{\partial x^4} \Big] A,\end{aligned} \tag{2.22}$$

which is further analyzed in detail in later chapters.

2.2 Direct Numerical Simulation

A commonly used approach in solving nonlinear differential equations is through Direct Numerical Simulation. With an initial condition as the starting point, the differential equation is integrated numerically step-wise in time, as the solution evolves to stable steady solutions or unstable dynamic states, depending on the defined state parameters. Different methods and algorithms exist for simulation of nonlinear dynamical systems. One such method called the Split-Step Method is described below along with two types of discretization and integration techniques.

2.2.1 Split-Step Method

A pseudo-spectral numerical method called the Split-Step Fourier method is used for solving nonlinear Partial Differential Equations. In this method, the nonlinear differential equation is split into two components, linear and nonlinear, and with the use of the Fourier transform successive forward steps in time is executed.
For instance, the solution for a complex system variable $A(x,t)$ of a partial differential equation can found be using the Split-Step method as follows:
First, the partial differential equation is split into two parts $\hat{L}$ and $\hat{N}$ consisting of the linear and nonlinear terms respectively.

$$\frac{\partial A}{\partial t} = \left[\hat{L} + \hat{N}\right] A. \tag{2.23}$$

$\hat{L}$ is a functional that consists of linear terms, e.g., derivatives and partial derivatives and $\hat{N}$ is a functional that gathers all the nonlinear terms. In order to take a step dt forward in time, the two terms are evaluated separately. This leads one purely linear and other purely nonlinear differential equations that need to be solved in sequential order.

$$\frac{\partial A}{\partial t} = \hat{L}A, \tag{2.24}$$

$$\frac{\partial A}{\partial t} = \hat{N}A. \tag{2.25}$$

The solution of Eq. (2.23) is given by

$$A(x, t+dt) = \exp\Big\{(\hat{L} + \hat{N})[A(x,t)]dt\Big\} \times A(x,t) \tag{2.26}$$

Generally, $\hat{L}$ and $\hat{N}$ do not commute and so a simple splitting of the exponential does not lead to high accuracy. Therefore, alternate splitting schemes are used to solve the Eq. (2.23). It essentially means that the sequential order of integration of the linear and nonlinear terms with each step size is done according to various schemes which results in more accurate solutions.
For each step in the simulation, the linear and nonlinear parts can be solved using the Euler method or by the spectral method, which is particularly useful in solving the linear terms since it utilizes the Fourier space.

$$A(x, t+dt) = \mathcal{F}^{-1}\left[\exp\Big\{\mathcal{F}[\hat{L}]dt\Big\} \times \mathcal{F}[A(x,t)]\right] \tag{2.27}$$

Here, $\mathcal{F}$ and $\mathcal{F}^{-1}$ refers to Fourier and inverse Fourier transform. While, the nonlinear part may be solved using the Euler method as

$$A(x,t+dt) = A(x,t) \times \exp\Big\{\hat{N}[A(x,t)]dt\Big\}. \tag{2.28}$$

Periodic boundary conditions are automatically imposed in the $x-$direction as a consequence of differentiation in Fourier space. This method requires the use of a good estimate as initial approximation that converges to a solution.
The advantage of using the Split-Step method is the treatment of the simulation in the Fourier space which can be computationally cheaper if the Fast Fourier Transform (FFT) algorithm is used.

2.2.2 Semi-Implicit Euler Scheme

A more precise time step estimation can be done using the Semi-Implicit Euler half-step scheme where intermediate half steps $dt/2$ are taken in the Fourier space to evaluate the linear part, while this central estimate is used to correct the nonlinear step. The algorithm for this method is given in the following equations:

$$A_f(x,t+dt/2) = \mathcal{F}^{-1}\left[\exp\Big\{\mathcal{F}[\hat{L}]dt/2\Big\} \times \mathcal{F}[A(x,t)]\right], \tag{2.29}$$

$$A_t(x,t+dt/2) = A_f(x,t+dt/2) \times \exp\Big\{\hat{N}[A_f]\, dt/2\Big\}, \tag{2.30}$$

$$A_N(x,t+dt) = A_f(x,t+dt/2) \times \exp\Big\{\hat{N}[A_t]\, dt\Big\}, \tag{2.31}$$

$$A(x,t+dt) = \mathcal{F}^{-1}\left[\exp\Big\{\mathcal{F}[\hat{L}]\, dt/2\Big\} \times \mathcal{F}[A_N(x,t+dt)]\right]. \tag{2.32}$$

An Euler half-step is taken in the Fourier space first to evaluate A_f for the linear part using the spectral method, which is then used to calculate an estimate for the central nonlinear approximation A_t with an explicit Euler half-step. Then, an implicit Euler full step is taken using the central nonlinear approximation to evaluate the nonlinear part A_N, which in turn is used to calculate the other linear half step in the Fourier space.
Using this semi-implicit scheme allows for greater accuracy in the calculated solution due to the additional implicit Euler corrective step taken. The algorithm above described in Eqs. (2.29)-(2.32) is used in iterative steps sequentially to calculate the solution of the nonlinear system equation at every time step dt over the defined time t.
This scheme has been used for numerical simulation of solutions of the QDNLSE (2.5) whose results are shown in later chapters.

2.2.3 Second Order Split-Step Scheme

The solution of the differential equation (2.23) given in Eq. (2.26) can be split in the second order as

$$A(x,t+dt) = \exp\Big\{\hat{N}[A]\, dt/2\Big\} \exp\Big\{\hat{L}[A]\, dt\Big\} \exp\Big\{\hat{N}[A]\, dt/2\Big\} \times A(x,t) \tag{2.33}$$

In this form the solution corresponds to first traversing a half-step in the nonlinear part of the solution and using that half-step approximation to traverse a full step in the linear part. Finally with another half-step, using the linear central approximation, in the nonlinear part results in one full step forward for the entire dynamical system equation. The algorithm for this method is given in the following equations:

$$A_N(x, t + dt/2) = E + (dt/2) \times \hat{N}[A(x, t)], \tag{2.34}$$

$$A_L(x, t + dt) = \mathcal{F}^{-1}\left[\exp\left\{-\mathcal{F}[\hat{L}]\, dt\right\} \times \mathcal{F}[A_N(x, t + dt/2)]\right], \tag{2.35}$$

$$A(x, t + dt) = E + (dt/2) \times \hat{N}[A_L(x, t + dt)]. \tag{2.36}$$

First, an explicit Euler half-step is taken in the nonlinear part of the system equation to find a nonlinear central approximation of the solution. Next, a full step is executed using spectral method to find the linear part of the solution using the central approximate. Finally, the other explicit Euler half-step is executed using the full-step linear solution estimate in order to complete a full-step forward in the whole dynamical system.
Using the Eqs. (2.34)-(2.36) in iterative sequential order with time step dt over the defined time period t, gives the time simulation solution of the nonlinear differential equation. This scheme has been used for direct numerical simulation of solutions of the MIXSEL model Equation (2.17) whose results are discussed in later chapters.

2.3 Numerical Path Continuation

Numerical Path Continuation can be used to study the steady and stationary states of nonlinear PDEs in parameter space and their stability. Parameter continuation is a technique that helps in the study of bifurcation points and different branches of states of a nonlinear PDE with varying control parameters.

2.3.1 Principles of Continuation

The basic principle in Path Continuation is to determine branches of steady state solutions ($\partial_t u = 0$), through the parameter space of a system of differential equations

$$\partial_t u = G(u, \lambda), \tag{2.37}$$

with system variables u and control parameter λ [22]. An initial guess solution u_0 is used to begin continuation and the control parameter λ is varied by small step sizes to find a new solution of Eq. (2.37). Calculating the new solution involves two distinct steps, namely, prediction of the solution at the new control parameter value, and correcting the predicted solution by solving Eq. (2.37) for a new control parameter value. This predictor-corrector method is a well known method for analyzing differential equations and different methods are employed for the prediction and correction steps [23].
This continuation treatment, i.e., increasing the control parameter λ by a fixed step size is called natural parameterization. With this parameterization, each solution along the continuation branch depends on the control parameter λ and next solution along the branch is "pulled" depending on this parameter. However, this kind of parameterization fails at points where the solution branch folds or turns. An alternate method can be used where the solution u as well as the parameter λ is parameterized with a different parameter to avoid this problem.
One such method is called pseudo-arclength parameterization where the arclength s of the solution branch is used as the continuation parameter. Both u and λ become functions of the arclength parameter s, i.e., $u = u(s)$ and $\lambda = \lambda(s)$. Therefore, the additional system equation to be solved for the extended system is the pseudo-arclength parameterization equation is given by

$$\dot{u} \cdot (u - u_0) + \dot{\lambda}(\lambda - \lambda_0) = \Delta s, \tag{2.38}$$

where $z = (\dot{u}, \dot{\lambda})$ is tangent or the direction of the branch given by the differential with respect to continuation parameter arclength s, and Δs is the step size in s.
Two predictor methods that are used to predict the next solution along a continuation branch are tangent predictor and secant predictor. In the tangent predictor method, the initial guess for the next solution state $({u_0}^{j+1}, {\lambda_0}^{j+1})$ is found by following the direction of the tangent of the previous solution state (u^j, λ^j) along the branch.

$$({u_0}^{j+1}, {\lambda_0}^{j+1}) = (u^j, \lambda^j) + \Delta s \; z \tag{2.39}$$

While for the secant predictor method, the next solution state is predicted from the difference of the last two continuation steps as

$$({u_0}^{j+1}, {\lambda_0}^{j+1}) = (u^j, \lambda^j) + \Delta s(u^j - u^{j-1}, \lambda^j - \lambda^{j-1}). \tag{2.40}$$

The most commonly used corrector is the Newton's method which converges well with small enough step size Δs. For continuation with additional constrains can be easily integrated into the system equations and one additional parameter is allowed to vary for each constraint.

2.3.2 Stability and Bifurcations

The stability of the solutions obtained from continuation can be determined by calculating the eigenvalues of the Jacobian $\partial_u G(u, \lambda)$ of the system Eq. (2.37). If there exists at least one eigenvalue whose real part is positive, it indicates that the steady state solution is unstable, i.e., small perturbations to the state leads to the solution diverging exponentially from the steady state. However, if the real parts of all eigenvalues are negative, it indicates stable steady state solutions, i.e., nearby states rapidly converge to the steady state solution. In case the real part of the largest eigenvalue by magnitude is zero, then higher order terms in the Taylor expansion around the steady state determines its stability.
If at a particular steady state (u_i, λ_i), the real component of the eigenvalues of the Jacobian changes sign, that point is called a local bifurcation point. It is accompanied by a sudden change in the phase portrait of the dynamical system for a small variation in the control parameter. These bifurcation points can be classified into different types of bifurcations depending on the stability of the steady state solutions at either direction from the bifurcation point. Two such bifurcations are discussed below.
A saddle-node bifurcation occurs when two steady states, one stable and the other unstable, collide and vanish. It is also sometimes called a fold bifurcation point since the steady state solution tends to fold back in the control parameter space.
At an Andronov-Hopf bifurcation point, a periodic orbit emerges from a steady state as the steady state changes its stability. Periodic orbits refer to trajectories of the system that are closed and the state traverses the same orbit path periodically. Andronov-Hopf bifurcation points are detected for two or more dimensional systems when a complex conjugated pair of eigenvalues of the Jacobian crosses the imaginary axis.

2.3.3 pde2path

The MATLAB [24] continuation and bifurcation package pde2path [25] is used for systems of nonlinear PDEs which allows for adding auxiliary equations, such as constrains

for mass conservation, and study of bifurcation diagrams for continuation of stationary and traveling waves. With the use of arclength continuation for a control parameter and tangent predictors, different branches of states and bifurcation points are navigated for a system of nonlinear PDEs.
In order to use pde2path to analyze the systems described by the Eqs. (2.5) and (2.22), it is necessary to transform each equation into a set of nonlinear PDEs with appropriate boundary conditions as constrains.
The pde2path continuation and bifurcation package treats PDE systems of the form

$$M_d \frac{\partial u}{\partial t} = -G(u,\lambda) \coloneqq \nabla \cdot (c\nabla u) - au + b \otimes \nabla u + f, \tag{2.41}$$

where $u = u(x,t) \in \mathbb{R}^N$ with N components, $t \geq 0$, $x \in \mathbb{R}^d$ with d being the dimensionality of the system, $M_d \in \mathbb{R}^{N\times N}$ is the mass matrix, $\lambda \in \mathbb{R}^p$ is the parameter vector, and the coefficients c, a, b and nonlinearity f may depend on x, u or λ. Auxiliary equations can also be added for $n_Q \geq 1$ constrains as

$$Q_j(u,\lambda) = 0. \tag{2.42}$$

The parameter vector λ consists of all parameters required to describe the system of equations, including n_Q free parameters and the rest as fixed or control parameters.
The Finite Element Method (FEM) [26] uses spatial discretization for numerical analysis which leads to a set of higher dimensional algebraic equations and is defined as follows for steady states

$$G(u,\lambda) \coloneqq K_{total}(u,\lambda) \cdot u - F_{total}(u,\lambda) = 0, \tag{2.43}$$

where $u = u(t) \in \mathbb{R}^{n_u}$ with $n_u = Nn_p$, n_p is the number of nodes in the FEM mesh and N is the number of system equations. K_{total} is called the stiffness matrix composed of N^2 blocks which may depend on u and F_{total} is the discretization of the nonlinearity terms of the system of equations $f = f(u)$ which can be combined with the mass matrix for ease of analysis.
In the case of semilinear problems where the coefficient c in Eq. (2.41) does not depend on u, the stiffness matrix K can be preassembled into a linear differential matrix $\mathcal{K}$ composed of the Laplacian and mass matrix M, whereas the other terms are accounted for in the matrix $F(u,\lambda)$. This allows for easier implementation of the Jacobian $\partial_u G(u)$ with the equation

$$\partial_u G(u,\lambda) = \mathcal{K} - \partial_u F(u,\lambda), \tag{2.44}$$

where $\partial_u F(u,\lambda) = M\,\partial_u f$, i.e., the Jacobian is built from the differential matrix $\mathcal{K}$ and M matrix times the local derivatives of the nonlinearity terms f. The eigenvalues of the Jacobian matrix are used for stability analysis of the states and to detect bifurcation points.
The implementation of the nonlinear PDEs given in Eqs. (2.5) and (2.22) is described in detail in the following subsections.

2.3.4 Quartic Dispersion Nonlinear Schrödinger Equation

In Eq. (2.5), the field $\psi(\tau,z)$ is a complex quantity ($\psi \in \mathbb{C}$) and contains a fourth order partial derivative term, along with a nonlinear term. Using the ansatz, $\psi(\tau,z) = u(\tau - vz)\exp^{i\mu z}$, with $u \in \mathbb{C}$ being the complex temporal profile with a variable rate of

change of phase μ, v being the velocity of this profile, and substituting into Eq. (2.5), we get the following form after removing the phase exponential

$$v\,\frac{\partial u}{\partial \tau} - i\,\mu\,u - i\,\frac{\beta_2}{2}\,\frac{\partial^2 u}{\partial \tau^2} + i\,\frac{\beta_4}{24}\,\frac{\partial^4 u}{\partial \tau^4} + i\,\gamma\mid u\mid^2 u = 0. \tag{2.45}$$

Since for the path continuation implementation, the system variables are taken to be real, we assume $u = u_1 + iu_2$ where $(u_1, u_2) \in \mathbb{R}$. Substituting this into the above equation gives a set of two equations with the use of separation of variables method for the linear terms consisting of u_1 and u_2

$$v\,\frac{\partial u_1}{\partial \tau} + \mu\,u_2 + \frac{\beta_2}{2}\,\frac{\partial^2 u_2}{\partial \tau^2} - \frac{\beta_4}{24}\,\frac{\partial^4 u_2}{\partial \tau^4} - \gamma\,u_2\,\left({u_1}^2 + {u_2}^2\right) = 0, \tag{2.46}$$

$$v\,\frac{\partial u_2}{\partial \tau} - \mu\,u_1 - \frac{\beta_2}{2}\,\frac{\partial^2 u_1}{\partial \tau^2} + \frac{\beta_4}{24}\,\frac{\partial^4 u_1}{\partial \tau^4} + \gamma\,u_1\,\left({u_1}^2 + {u_2}^2\right) = 0. \tag{2.47}$$

In the implementation of the FEM matrices for this system, the second order derivative is easily implemented using the differential matrix K_{total} due to the Bilaplacian in the definition of Eq. (2.41) for a semilinear system. However, to account for the fourth order derivative, additional system variables are defined as follows

$$\begin{aligned} u_3 &= \frac{\partial^2 u_1}{\partial \tau^2} = \partial_{\tau\tau} u_1, \\ u_4 &= \frac{\partial^2 u_2}{\partial \tau^2} = \partial_{\tau\tau} u_2. \end{aligned} \tag{2.48}$$

Combining all the resulting equations, the system is defined as a set of four PDEs and periodic boundary conditions with four real system variables $U = (u_1, u_2, u_3, u_4) \in \mathbb{R}$ and a set of parameters $\lambda = (\beta_2, \beta_4, \gamma, \mu, v) \in \mathbb{R}$.

$$v\,\partial_\tau u_1 + \mu\,u_2 + \frac{\beta_2}{2}\,u_4 - \frac{\beta_4}{24}\,\partial_{\tau\tau} u_4 - \gamma\,u_2\,\left({u_1}^2 + {u_2}^2\right) = 0 \tag{2.49}$$

$$v\,\partial_\tau u_2 - \mu\,u_1 - \frac{\beta_2}{2}\,u_3 + \frac{\beta_4}{24}\,\partial_{\tau\tau} u_3 + \gamma\,u_2\,\left({u_1}^2 + {u_2}^2\right) = 0 \tag{2.50}$$

$$\partial_{\tau\tau} u_1 - u_3 = 0 \tag{2.51}$$

$$\partial_{\tau\tau} u_2 - u_4 = 0 \tag{2.52}$$

This set of equations forms a steady state system of PDEs and the FEM matrices can be easily generated for continuation where the nonlinearity f is taken as

$$f = \begin{pmatrix} \mu\,u_2 + \frac{\beta_2}{2}\,u_4 - \gamma\,u_2\,\left({u_1}^2 + {u_2}^2\right) \\ -\mu\,u_1 - \frac{\beta_2}{2}\,u_3 + \gamma\,u_1\,\left({u_1}^2 + {u_2}^2\right) \\ -u_3 \\ -u_4 \end{pmatrix}. \tag{2.53}$$

Due to the periodic boundary conditions, additional auxiliary constrains have to be implemented in order to maintain the symmetry of the phase shift between the real u_1 and complex u_2 components as well as translational invariance of the temporal profile

$u(\tau - vz)$. The phase shift symmetry condition q_1 and the translational invariance condition q_2 form the constrain equations $Q_j = 0$. From the Goldstone modes of translation and rotation symmetry breaking, the symmetry conditions are given as

$$Q_j = \begin{pmatrix} q_1 \\ q_2 \end{pmatrix} = \begin{pmatrix} {u_1}^k \cdot ({u_2}^{k+1} - {u_2}^k) - {u_2}^k \cdot ({u_1}^{k+1} - {u_1}^k) \\ \partial_\tau U^k \cdot (U^{k+1} - U^k) \end{pmatrix}, \tag{2.54}$$

where ${u_j}^k$ is the $j-$th component of the system variables vector U at the $k-$th iteration of continuation. This set of constrains allows for defining two free parameters, namely μ which modulates the temporal phase and velocity v of the steady state solution.

2.3.5 MIXSEL Model Equation

In Eq. (2.17), the transverse field envelope $A(r_\perp, \theta)$ is a complex quantity. Using a simple one-dimensional ansatz in the co-moving frame for simplicity, $A(x, \theta) = \phi(x - v\theta)e^{-i\omega\theta}$ where ω is the frequency shift parameter and v is the velocity of the complex profile ϕ. Substituting this ansatz into Eq. (2.17) and using $\phi = \phi_1 + i\phi_2$, where $(\phi_1, \phi_2) \in \mathbb{R}$, to separate the real and complex terms into two equations results as

$$\begin{aligned} v\,\frac{\partial \phi_1}{\partial x} - \omega\,\phi_2 + (\phi_1 + \alpha_1\phi_2)J_1\,g(|\,\phi\,|^2) + (\phi_1 + \alpha_2\phi_2)J_2\,g(s\mid\phi\,|^2) - k\phi_1 \\ -\tilde{C}x^2\phi_2 + d\frac{\partial^2\phi_1}{\partial x^2} - \tilde{B}\frac{\partial^2\phi_2}{\partial x^2} - S\frac{\partial^4\phi_2}{\partial x^4} = 0, \end{aligned} \tag{2.55}$$

$$\begin{aligned} v\,\frac{\partial \phi_2}{\partial x} + \omega\,\phi_1 + (\phi_2 - \alpha_1\phi_1)J_1\,g(|\,\phi\,|^2) + (\phi_2 - \alpha_2\phi_1)J_2\,g(s\mid\phi\,|^2) - k\phi_2 \\ +\tilde{C}x^2\phi_1 + d\frac{\partial^2\phi_2}{\partial x^2} + \tilde{B}\frac{\partial^2\phi_1}{\partial x^2} + S\frac{\partial^4\phi_2}{\partial x^4} = 0. \end{aligned} \tag{2.56}$$

As described in the previous section for the QDNLSE, similarly to account for the fourth order partial derivative additional system variables are defined as follows,

$$\begin{aligned} \phi_3 &= \frac{\partial^2\phi_1}{\partial x^2} = \partial_{xx}\phi_1 \\ \phi_4 &= \frac{\partial^2\phi_2}{\partial x^2} = \partial_{xx}\phi_2 \end{aligned} \tag{2.57}$$

Hence, using the above results, the MIXSEL model is defined as a system of four equations and periodic boundary conditions with system variables vector $\Phi = (\phi_1, \phi_2, \phi_3, \phi_4)$ where $(\phi_1, \phi_2, \phi_3, \phi_4) \in \mathbb{R}$ and parameter vector $\lambda = (\alpha_1, \alpha_2, J_1, J_2, h, s, \eta, d, \tilde{B}, \tilde{C}, S) \in \mathbb{R}$.

$$\begin{aligned} v\,\partial_x\phi_1 - \omega\,\phi_2 + (\phi_1 + \alpha_1\phi_2)J_1\,g(|\,\phi\,|^2) + (\phi_1 + \alpha_2\phi_2)J_2\,g(s\mid\phi\,|^2) - k\phi_1 \\ -\tilde{C}x^2\phi_2 + d\phi_3 - \tilde{B}\phi_4 - S\partial_{xx}\phi_4 = 0 \end{aligned} \tag{2.58}$$

$$\begin{aligned} v\,\partial_x\phi_2 + \omega\,\phi_1 + (\phi_2 - \alpha_1\phi_1)J_1\,g(|\,\phi\,|^2) + (\phi_2 - \alpha_2\phi_1)J_2\,g(s\mid\phi\,|^2) - k\phi_2 \\ +\tilde{C}x^2\phi_1 + d\phi_4 + \tilde{B}\phi_3 + S\partial_{xx}\phi_3 = 0 \end{aligned} \tag{2.59}$$

$$\partial_{xx}\phi_1 - \phi_3 = 0 \tag{2.60}$$

$$\partial_{xx}\phi_2 - \phi_4 = 0 \tag{2.61}$$

These four equations form the steady state system of PDEs with the nonlinearity f is defined as

$$f = \begin{pmatrix} f_1 \\ f_2 \\ f_3 \\ f_4 \end{pmatrix}, \tag{2.62}$$

where

$$\begin{aligned} f_1 = -\omega\ \phi_2 + (\phi_1 + \alpha_1\phi_2)J_1\ g(\mid \phi \mid^2) + (\phi_1 + \alpha_2\phi_2)J_2\ g(s \mid \phi \mid^2) \\ -k\phi_1 - \tilde{C}x^2\phi_2, \end{aligned} \tag{2.63}$$

$$\begin{aligned} f_2 = \omega\ \phi_1 + (\phi_2 - \alpha_1\phi_1)J_1\ g(\mid \phi \mid^2) + (\phi_2 - \alpha_2\phi_1)J_2\ g(s \mid \phi \mid^2) \\ -k\phi_2 + \tilde{C}x^2\phi_1, \end{aligned} \tag{2.64}$$

$$f_3 = -\phi_3, \tag{2.65}$$

$$f_4 = -\phi_4. \tag{2.66}$$

The FEM matrices for continuation are generated similarly to the previous section for this steady state system of equations, along with the constrain equations Q_f for both phase shift symmetry and translational invariance of the steady states as defined in Eq. (2.54). The two free parameters which compensate for these constrains are ω and v.
The analytical Jacobian of the system equations, (2.58)-(2.61), which is used for extracting the stability information of the solutions obtained from continuation is calculated according to the Eq. (2.44), where the local derivative of the nonlinearity f with respect to the system variable matrix Φ is

$$\partial_\Phi f = \begin{pmatrix} \partial_{\phi_1} f_1 & \partial_{\phi_2} f_1 & \partial_{\phi_3} f_1 & \partial_{\phi_4} f_1 \\ \partial_{\phi_1} f_2 & \partial_{\phi_2} f_2 & \partial_{\phi_3} f_2 & \partial_{\phi_4} f_2 \\ \partial_{\phi_1} f_3 & \partial_{\phi_2} f_3 & \partial_{\phi_3} f_3 & \partial_{\phi_4} f_3 \\ \partial_{\phi_1} f_4 & \partial_{\phi_2} f_4 & \partial_{\phi_3} f_4 & \partial_{\phi_4} f_4 \end{pmatrix}, \tag{2.67}$$

where $\partial_\phi = \partial/\partial\phi$. Similarly, the Jacobian for the auxiliary contrain condition is also calculated for the contrain matrix in Eq. (2.54).

3 Generalized Dispersion Kerr Solitons

The solutions of the Quartic Dispersion Nonlinear Schrödinger Equation (2.5) can be analyzed by considering the linear part of the PDE, assuming weak Kerr nonlinearity in the low-power regime for negative quartic dispersion. Using the following ansatz for stationary solutions, which maintain the shape of the solitons, throughout propagation

$$\psi(\tau, z) = u(\tau)e^{i\mu z}, \tag{3.1}$$

where $u(\tau) \in \mathbb{R}$ is the temporal profile of the solution and μ is the frequency shift, the Eq. (2.5) takes the form of a nonlinear Ordinary Differential Equation (ODE).

$$-\mu u - \frac{\beta_2}{2}\frac{\mathrm{d}^2 u}{\mathrm{d}\tau^2} - \frac{|\beta_4|}{24}\frac{\mathrm{d}^4 u}{\mathrm{d}\tau^4} + \gamma u^3 = 0 \tag{3.2}$$

For low-power tails, discarding the nonlinear term, the ODE has solutions that are linear combinations of $e^{\lambda\tau}$, where roots λ are given by

$$\lambda^2 = -\frac{6\beta_2}{\mid \beta_4 \mid} \pm \sqrt{\frac{36{\beta_2}^2}{{\beta_4}^2} - \frac{24\mu}{\mid \beta_4 \mid}}. \tag{3.3}$$

The roots λ are either real or complex conjugate pairs and the critical value of μ for which the discriminant in Eq. (3.3) vanishes is

$$\mu_0 = \frac{3{\beta_2}^2}{2 \mid \beta_4 \mid}. \tag{3.4}$$

The parabola (black) in Fig. 3.1 illustrates the critical value μ_0 as a function of parameter β_2. Thus, the Generalized Dispersion Kerr Solitons (GDKS) which are a family of solutions of Eq. (2.5) can be classified into several regimes depending on the variations in the values of μ and β_2. For $\beta_2 < 0$ and $\mu < \mu_0$, the roots λ are real and the solutions have exponentially decaying tails without oscillations, e.g., Karlsson and Höök solutions given in Eq. (2.6). For $\beta_2 > 0$ and $\mu < \mu_0$, the roots λ are imaginary, the linear tails become purely oscillatory and no localized pulse-like solutions exist. In case of $\mu > \mu_0$, for any β_2, λ is complex and solutions with exponentially suppressed oscillating tails exist with decreasing exponential decay rate of oscillatory tails as β_2 increases. In the following, $\beta_4 < 0$ is always assumed.
These analytical findings are further confirmed in the following sections where first the system is implemented assuming real field solutions and then it is extended for complex field solutions to analyze pattern formation in this optical system with positive quadratic dispersion, β_2.

3.1 Real Field Implementation

Arclength Path Continuation of the Quartic Dispersion Nonlinear Schrödinger Equation given in Eq. (2.5) is implemented as described in Section 2.3.4 for real field envelope $\psi(\tau, z) \in \mathbb{R}$ as solution using the Eqs. (2.49) and (2.51) as system equations, along with the condition for translational invariance as constrain. Accordingly, the velocity v in the ansatz for the co-moving frame, $\psi(\tau, z) = u(\tau - vz)e^{i\mu z}$, is the only free parameter in this instance.
The Karlsson and Höök solution (2.6) is used as the initial guess for continuation defined with the following parameters : $\beta_2 = -0.1$, $\beta_4 = -1.0$, $\gamma = 1.0$, $\mu = 0.0096$. The emergence of transversal patterns in the solution with increasing quadratic dispersion

β_2 is confirmed and the variations of these patterns with the change in parameter μ is analyzed in the following.
Continuation is performed using pde2path [25] with a tangent predictor for arc-length and the residual tolerance is set to 10^{-14}. Since the system is defined as real and conservative, the solutions are always stable and for stationary solutions, the velocity is ensured to be negligible, i.e., $v \approx 0$.
In Fig. 3.1, the parameter space of μ versus β_2 is illustrated and the different regions classifying the tails of the solutions are highlighted using the critical value μ_0 of the parameter μ given in Eq. (3.4). For the region where $\mu < \mu_0$ and $\beta_2 > 0$ (grey shaded area), no pulse-like localized solutions could be obtained from continuation in this parameter space.
In the region where $\mu < \mu_0$ and $\beta_2 < 0$ (light green shaded area), conventional soliton-like solutions exist with exponentially decaying tails including the Karlsson and Höök family of solutions, marked by the green dashed line (KH) in Fig. 3.1. Another solution in this region, labeled (a) in Fig. 3.1, is shown in Fig. 3.2(a) which has exponentially decaying tails.

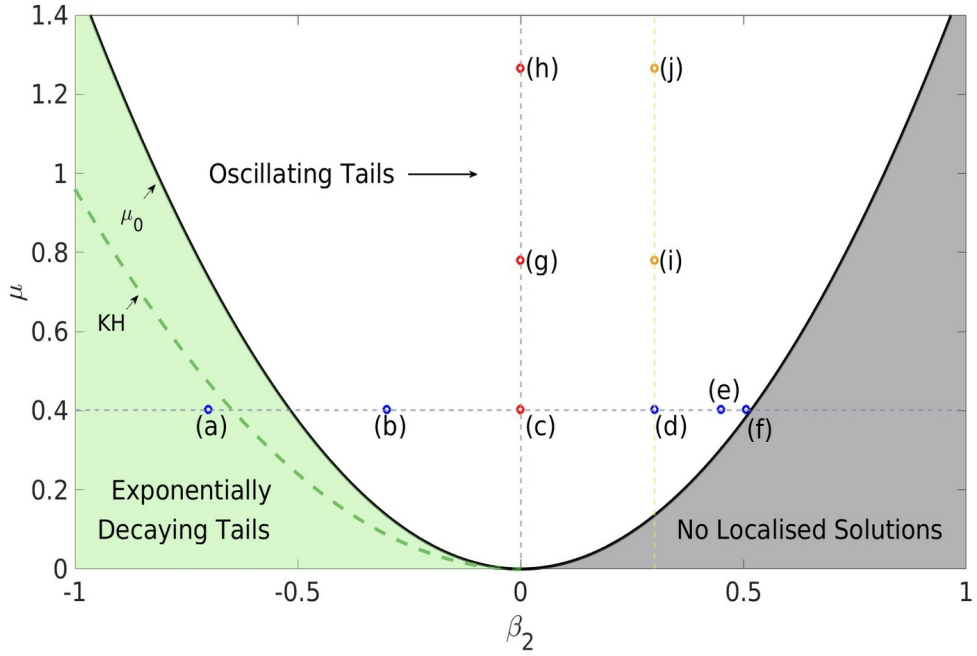

Figure 3.1: Solutions of Eq. (3.2) in the (μ, β_2) plane for fixed $\beta_4 = -1.0$ and $\gamma = 1.0$. The parabola (black) illustrates the critical value μ_0 in Eq. (3.4). The section under the parabola for $\beta_2 < 0$ (light green shaded area) is where exponentially decaying tails solutions exist like the KH solutions (green dashed line) and the soliton solution marked as (a). No localized solutions exists in the region under the parabola for $\beta_2 > 0$ (grey shaded area). The region above the parabola (white) consists of localized solutions that have increasingly oscillating tails as β_2 increases. The solutions marked in red circles (c, g, h) are Pure Quartic Solitons (PQS) for increasing μ, respectively. The solutions marked in blue circles (a, b, d, e, f) correspond to solutions with fixed $\mu = 0.4027$ and increasing β_2, respectively. The yellow circles (i, j) mark solutions with fixed positive $\beta_2 = 0.3$ and increasing μ, respectively.

The regime of interest in this parameter space is for $\mu > \mu_0$, i.e., the white region in Fig. 3.1, where solutions with oscillating tails or transversal patterns exist. Continuation in this parameter space confirms the analytical results discussed in the previous section. The profiles of the solutions labeled (a-f) in Fig. 3.1 are shown in Figs. 3.2(a-f) for a fixed value of $\mu = 0.4027$. As can be seen from the intensity profiles, with increasing β_2

values the solutions become more oscillatory until the critical value μ_0 is reached when localized solutions no longer exist. The corresponding power spectrum are given in Figs. 3.2(i-vi).

Starting from the intensity profile shown in Fig. 3.2(a) and its power spectrum in Fig. 3.2(i), with $\beta_2 = -0.7$, the solution falls below the critical value of μ_0 and has exponentially decaying tails along with single peak power in the Fourier domain. With increasing β_2, in Fig. 3.2(b) and its power spectrum in Fig. 3.2(ii), corresponding to $\beta_2 = -0.3$, some spectral broadening to the peak in Fourier space is observed while the peak intensity of the profile decreases slightly. Considering the Pure Quartic Soliton (PQS) solution with $\beta_2 = 0.0$ in Fig. 3.2(c) shows decreasing peak intensity, along with further broadening of the spectral peak in Fig. 3.2(iii).

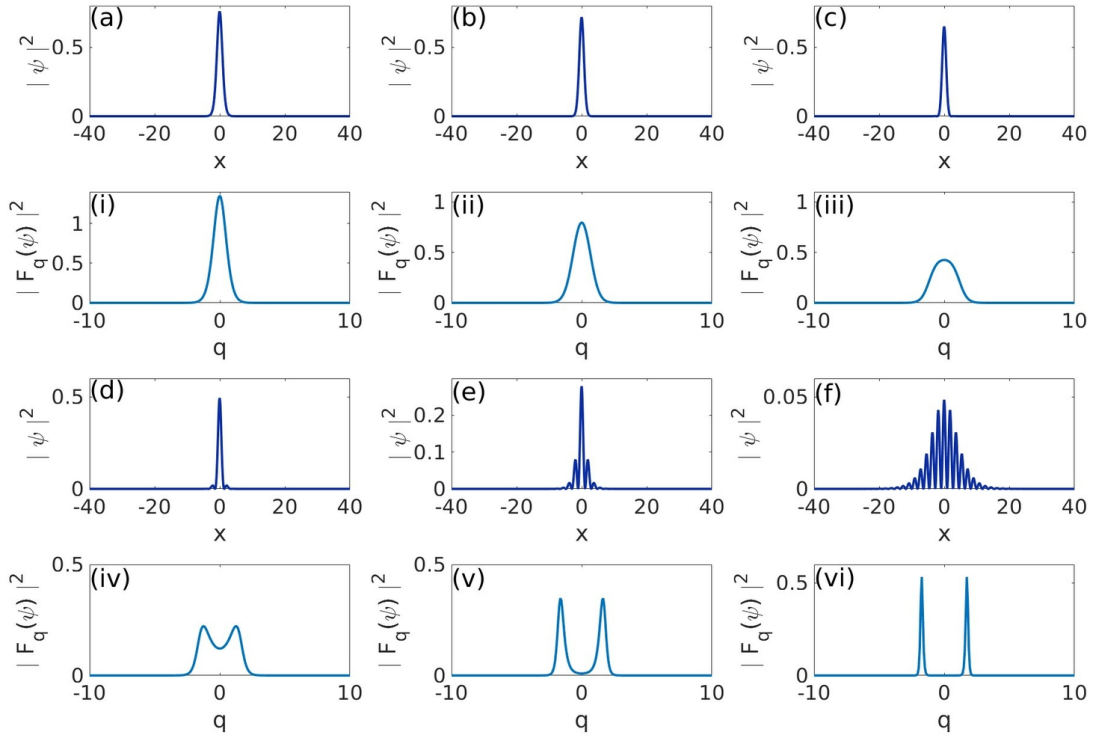

Figure 3.2: Intensity profiles and their corresponding power spectrum of the solutions marked in Fig. 3.1 for fixed $\mu = 0.4027$ and increasing β_2. Panels (a-f) show the profiles of the solutions for values of parameter $\beta_2 = (-0.7, -0.3, 0.0, 0.3, 0.45, 0.51)$, respectively. The panels (i-vi) are the corresponding power spectrum in Fourier domain of the solutions in (a-f), respectively. Other parameters are : $\beta_4 = -1.0, \gamma = 1.0$.

Fig. 3.2(d) shows the intensity profile for $\beta = 0.3$ where oscillating tails start to emerge in the solution and correspondingly the power spectrum peak starts to split two with spectral broadening in the Fourier space as shown in Fig. 3.2(iv). The solution for $\beta_2 = 0.45$ has oscillatory tails as shown in Fig. 3.2(e) and its power spectrum in Fig. 3.2(v) has two peaks that are symmetric about the frequency $q = 0$ in the Fourier domain. Finally, the solution for $\beta_2 = 0.51$ is shown in Fig. 3.2(e) along with its power spectrum in Fig. 3.2(vi). This solution is highly oscillatory since it lies very close to the critical value $\mu > \mu_0 = 0.39$ in the (μ-β_2) plane. Similarly, the power spectrum shows two symmetric narrow peaks of high spectral frequencies corresponding to the frequency shift of the oscillatory tails.

Therefore, in summary of the continuation results in the region $\mu > \mu_0$, for fixed value of

μ and increase in parameter β_2, one finds the resulting solutions to be increasingly oscillatory giving rise to transversal patterns along with decreasing peak intensities. Alongside, the power spectrum shows spectral broadening until it splits into two symmetric peaks with increasing spectral frequency shifts.

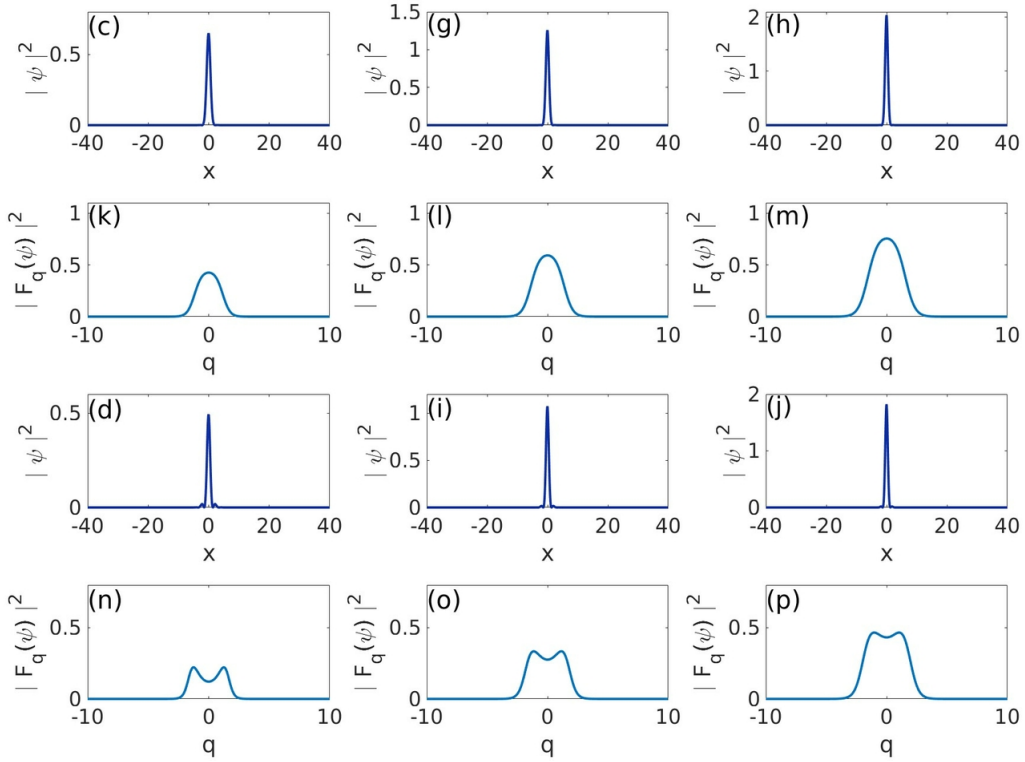

Figure 3.3: Intensity profiles and their corresponding power spectrum of the solutions marked in Fig. 3.1 with red and yellow circles corresponding to fixed β_2 values of (0.0 and 0.3), respectively, for increasing μ. The panels (c), (g), (h) shows the profiles of PQS solutions ($\beta_2 = 0$) for values $\mu = (0.4027, 0.7801, 1.2656)$, respectively together with their corresponding power spectrum in panels (k-m). The panels (d), (i), (j) shows the profiles of the solutions with fixed positive $\beta_2 = 0.3$ with increasing values of $\mu = (0.4027, 0.7801, 1.2656)$, respectively together with their power spectrum in panels (n-p). Other parameters are : $\beta_4 = -1.0, \gamma = 1.0$.

Figure 3.3 shows the solutions from path continuation for different values of μ while β_2 is kept fixed. The panels in Fig. 3.3(c), (g) and (h) are the intensity profiles of PQS solutions ($\beta_2 = 0$), for increasing values of μ, respectively. One can notice that the peak intensity of the profile depends on the value of μ, i.e., the intensity increases with the increase in μ. Their corresponding power spectrum is shown in Fig. 3.3(k-m) which is the typical power spectrum of solitons which are formed by the effects of only quartic dispersion and Kerr nonlinearity. However, some spectral broadening can be observed due to the increasing value of μ.

Another set of solutions for variable μ and fixed β_2 are shown in Figs. 3.3(d), (i) and (j). Here, a positive $\beta_2 = 0.3$ is kept fixed for the solutions while the values of parameter μ are : $(0.4027, 0.7801, 1.2656)$, respectively. Similarly for the PQS, the peak intensity increases with μ, on the other hand, the solution becomes less oscillatory as the distance from the critical value μ_0 increases in the parameter space as shown in Fig. 3.1. This phenomenon is reflected in the panels showing corresponding the power spectrum of the above solutions in Figs. 3.3(n-p).

The above results were achieved using a constant negative value of $\beta_4 = -1.0$. Varying

β_4 yielded similar trends in the solutions for μ and β_2 corresponding to a different critical value μ_0. Since the solutions are assumed to be real fields in a conservative system, the stability of these solutions cannot be analyzed. To overcome this difficulty, the system is extended into the complex regime where the stability information can be achieved from the eigenvalue spectrum.

3.2 Complex Field Implementation

In order to perform Arc-length Path Continuation of the Quartic Dispersion Nonlinear Schrödinger Equation for a complex field envelope $\psi(\tau, z) \in \mathbb{C}$ as solution, the procedure as described in Section 2.3.4 is used. Unlike for the real system, four system equations are used and hence, two auxiliary conditions, corresponding to phase shift symmetry and translational invariance, are applied which results in two free parameters, μ and v. Again, the Karlsson and Höök solution given in Eq. (2.6) is used as the initial guess with the complex components of the system variable vector set to zero, i.e., $u_2, u_4 = 0$. Parameters used for the initial guess are : $\beta_2 = -0.7$, $\beta_4 = -1.0$, $\gamma = 1.0$, $\mu = 0.4704$. Continuation is performed using pde2path [25] package with a secant arc-length predictor and the residual tolerance is set to 10^{-14}. The first 100 eigenvalues of the numerical Jacobian are used for checking the stability of the solution and for possible bifurcation detection along the continuation branch.
Some of the stable resulting solutions of continuation in the same branch are shown in Fig. 3.4. Along this stable solution branch from the intensity profiles shown in Figs. 3.4(a-d), one can observe that the tails of the solution becomes more oscillatory as β_2 increases, similar to the results obtained in the previous section for real field envelope solutions. Accordingly, the optical power peak in the spectral domain shown in Figs. 3.4(e-h) splits into two peaks corresponding to two peak spectral frequencies for highly oscillatory solutions. The parameter μ is a free parameter and hence the peak intensity for these solutions varies as continuation progresses.

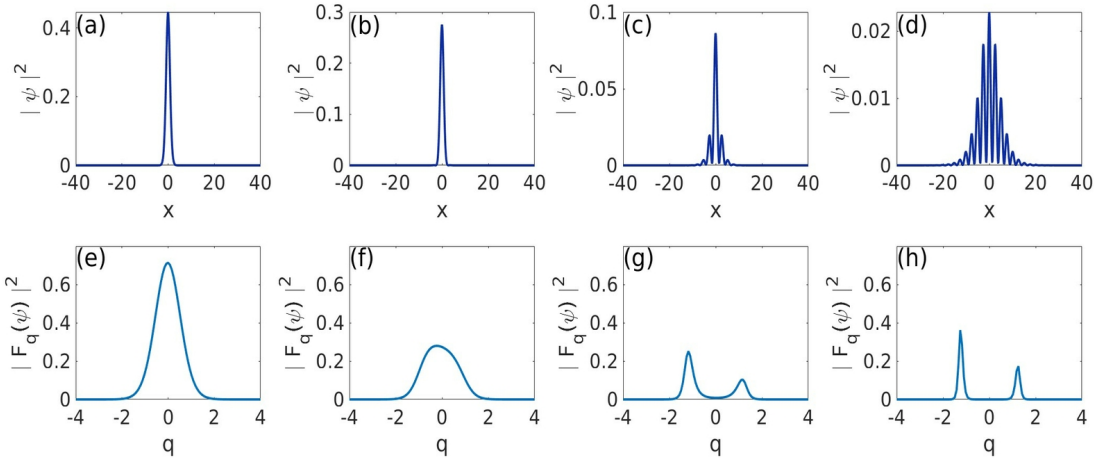

Figure 3.4: Intensity profiles of stable complex field envelope solutions and their corresponding power spectrum. The profile in (a) corresponds to the parameter values $\beta_2 = -0.3$ and $\mu = 0.2465$ with its power spectrum in panel (e). The profile in (b) corresponds to the parameter values $\beta_2 = 0.0$ and $\mu = 0.1716$ with its power spectrum in panel (f). The profile in (c) corresponds to the parameter values $\beta_2 = 0.2321$ and $\mu = 0.0808$ with its power spectrum in panel (g). The profile in (d) corresponds to the parameter values $\beta_2 = 0.256$ and $\mu = 0.0.9835$ with its power spectrum in panel (h). Other parameters : $\beta_4 = -1.0$ and $\gamma = 1.0$.

However, unlike in the results for the real system implementation, from the Figs. 3.4(g-

h), the power spectrum peaks are not symmetric about spectral frequency $q = 0$. For the solution shown in Fig. 3.4(d) and its spectrum in Fig. 3.4(h), one observes that the peak power corresponding to the negative spectral frequency is higher than for the positive spectral frequency.
Solutions from continuation along a different branch are shown in Fig. 3.5. Stable solutions that have symmetric power spectrum peaks also exist, however, during continuation along the branch, they quickly settle into one of the asymmetric solutions. In Fig. 3.5(a), another stable solution was found along a different branch that is highly oscillatory due to being close of the critical value μ in the parameter space. The corresponding power spectrum in Fig. 3.5(d) shows that the power peaks are asymmetric with the peak corresponding to the positive spectral frequency being higher than for the negative spectral frequency. It was found that the type of asymmetry, higher peak power for either the positive or negative spectral frequencies, depend on the oscillation frequency of the complex component of the solution.

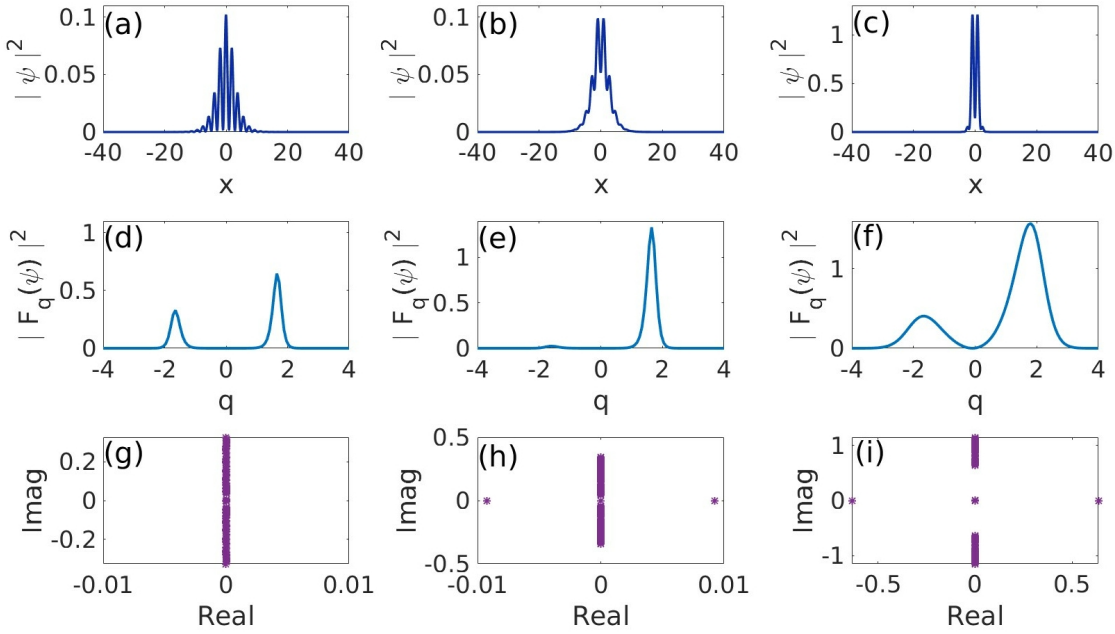

Figure 3.5: Intensity profiles of the complex field envelope solutions, their corresponding power spectrum and stability eigenvalues. The stable solution profile in (a) corresponds to the parameter values $\beta_2 = 0.4638$ and $\mu = 0.3607$ with its power spectrum in panel (d) and stability eigenvalues in (g). The quasi-stable solution profile in (b) corresponds to the parameter values $\beta_2 = 0.4481$ and $\mu = 0.369$ with its power spectrum in panel (e) and stability eigenvalues in (h). The unstable solution profile in (c) corresponds to the parameter values $\beta_2 = 0.5072$ and $\mu = 1.1977$ with its power spectrum in panel (f) and stability eigenvalues in (i). Other parameters : $\beta_4 = -1.0$ and $\gamma = 1.0$.

For the complex system implementation, unstable solutions also exist along the continuation branches, two examples of which are shown in Figs. 3.5(b-c). The profile of an unstable solution is shown in Fig. 3.5(c) along with its power spectrum in Fig. 3.5(f) which indicates spectral asymmetric power peaks. As can be observed from the stability eigenvalues in Fig. 3.5(i) for this unstable solution, a pair of real conjugate eigenvalues exist, the negative real eigenvalue of the Jacobian indicates instability.
In contrast, the stability eigenvalues of the stable solution in Fig. 3.5(a) in the same continuation branch, Fig. 3.5(g), the eigenvalues of the Jacobian are imaginary conjugate pairs, indicating stability of the solution. From the stability eigenvalues shown in Fig.

3.5(h) and (i) for the two unstable solutions, the higher magnitude of the negative real eigenvalue, the more unstable the solution becomes.
The instability of the solutions shown in Fig. 3.5 is confirmed by direct numerical simulation as described in Section 2.2 by analyzing the time evolution of each solution and the results are shown in Fig. 3.6. Each solution was simulated for time $t = 200$ with time steps $dt = 5 \times 10^{-5}$.

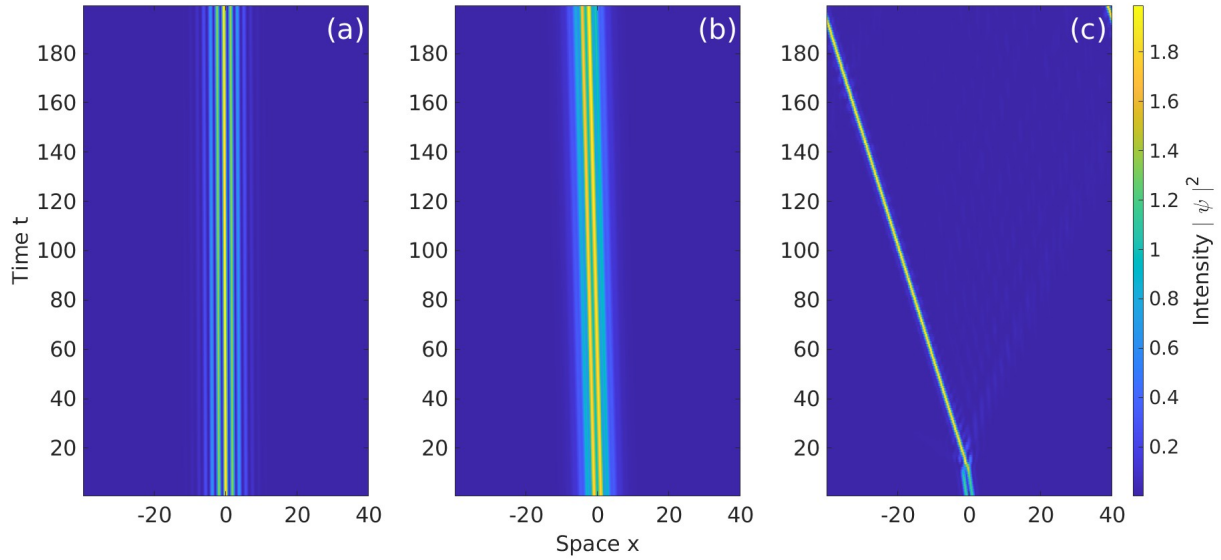

Figure 3.6: Time evolution of the solutions given in Fig. 3.5(a-c) by direct numerical simulation respectively in panels (a-c). Parameters for profile in panel (a) : $\beta_2 = 0.4638$ and $\mu = 0.3607$. Parameters for profile in panel (b) : $\beta_2 = 0.4481$ and $\mu = 0.369$. Parameters for profile in panel (c) : $\beta_2 = 0.5072$ and $\mu = 1.1977$. Other parameters : $\beta_4 = -1.0$ and $\gamma = 1.0$.

The panel in Fig. 3.6(a) shows the time evolution of the stable solution shown in Fig. 3.5(a). The intensity profile of the solution remains unchanged as time increases. The velocity of this solution which is a free parameter in the continuation system is $v = 0.0027$.
In the panel Fig. 3.6(b), the time evolution of solution in Fig. 3.5(b) is shown. This solution is unstable in time, as it shifts in the $-x$ spatial direction progressively in time due to the velocity of the solution being a magnitude higher than the stable solution at $v = 0.0167$. This explains the lower magnitude of the negative real stability eigenvalues of this solution. The intensity profile of the solution also evolves with time, but without dissipating completely.
Finally, the panel in Fig. 3.6(c) illustrates the time evolution of the unstable solution given in Fig. 3.5(c). The intensity profile of the solution continues to dissipate with time along with shifts along the $-x$ spatial direction until the solution leaves the domain entirely. Radiative losses can be seen on the right flank of the solution profile. The velocity of this unstable solution obtained from continuation $v = 0.0992$ confirms this result.
In conclusion, with the implementation of the complex system, the results obtained in the previous section for the real system for the emergence and dynamics of transversal pattern formation in the solutions are confirmed. Asymmetric spectral peak solutions along the continuation branches also exist. Additional instability in the solutions were found and tested with direct numerical analysis.

4 One-Dimensional MIXSEL model

4.1 Hermite Gauss Modes

The MIXSEL model equation described in Section 2.1.2 can be analytically solved by considering the underlying linear system within a perfect empty cavity. In Eq. (2.22), the PDE with one spatial transverse dimension is given for the transverse field envelope $A(x, \theta)$. This equation for a system in an empty cavity, i.e., $J_1 = J_2 = 0$ and $h = 2, \eta = 1$, leads to

$$\frac{\partial A}{\partial \theta} = \left(i\tilde{C}x^2 \; + \; i\tilde{B}\frac{\partial^2}{\partial x^2} \; + \; iS\frac{\partial^4}{\partial x^4} \right) A. \tag{4.1}$$

For monochromatic ansatz $A(x, \theta) = e^{-i\omega_n \theta}\tilde{A}(x)$, where ω_n is the frequency corresponding to the eigenmode, the above linear PDE transforms into an equivalent linear ODE for which analytical solutions exist. With boundary conditions requiring the solution to be bounded in $x \to \pm\infty$, forces the mode frequency ω_n to be within a specific range. Then, the effective linear ODE becomes

$$\left[\left(\tilde{C}x^2 + \omega_n \right) + \tilde{B}\frac{\mathrm{d}^2}{\mathrm{d}x^2} + S\frac{\mathrm{d}^4}{\mathrm{d}x^4} \right] \tilde{A} = 0. \tag{4.2}$$

Two different cases are considered in the following sections, to find an analytical solution of Eq. (4.2), a stable cavity without aberrations ($S = 0$) and an unstable cavity with aberrations ($S \neq 0$).

4.1.1 Stable Cavity

In a stable cavity with $S = 0$, the solutions of Eq. (4.2) are called Hermite-Gauss modes, $M_n = M_n(x)$ which are solutions to the ODE

$$\frac{\mathrm{d}^2 M_n}{\mathrm{d}x^2} + (2n + 1 - x^2)M_n = 0 \tag{4.3}$$

of the form $M_n(x) = H_n(x)\, \exp\left[-x^2/2\right]$, where $H_n(x)$ is the nth order Hermite polynomial. Bounded solutions $\tilde{A}(x)$ of the Eq. (4.2) exists if the waist σ of the solution is positive, which depends on the signs of the parameters $\tilde{B}$ and $\tilde{C}$ as

$$\sigma^2 = \sqrt{\frac{-\tilde{B}}{\tilde{C}}}. \tag{4.4}$$

Hence, the monochromatic bounded solutions for a system with weak nonlinearity and losses and no aberrations, in a stable cavity, are Hermite-Gauss modes with a specific eigenfrequency for the mode number n given below as

$$\tilde{A}(x) = M_n\left(\frac{x}{\sigma}\right), \tag{4.5}$$

$$\omega_n = \frac{\tilde{B}}{\sigma^2}(2n + 1). \tag{4.6}$$

4.1.2 Unstable Cavity

Bounded analytical solutions of the Eq. (4.2) do not exist for $S \neq 0$, however with ansatz given as

$$\tilde{A}(x) = \psi(x) \exp\{ik_\perp x\} \quad \text{with} \quad k_\perp = \sqrt{\frac{\tilde{B}}{2S}} \tag{4.7}$$

leads to the following ODE

$$\psi\left(\tilde{C}x^2 + \omega_n - \frac{\tilde{B}^2}{4S}\right) - 2\tilde{B}\frac{\mathrm{d}^2\psi}{\mathrm{d}x^2} + i\sqrt{8\tilde{B}S}\frac{\mathrm{d}^4\psi}{\mathrm{d}x^4} + S\frac{\mathrm{d}^4\psi}{\mathrm{d}x^4} = 0. \tag{4.8}$$

Neglecting the third and fourth order derivatives and assuming only lowest order solutions, that are also proportional to the small parameter S one obtains the equation

$$\psi\left(\tilde{C}x^2 + \omega_n - \frac{\tilde{B}^2}{4S}\right) - 2\tilde{B}\frac{\mathrm{d}^2\psi}{\mathrm{d}x^2} = 0 \tag{4.9}$$

which reduces the system equation into a Hermite-Gauss ODE of the form given in Eq. (4.3) in which the parameter $\tilde{B}$ is replaced by $-2\tilde{B}$ and, therefore, forms a stable cavity. The mode-frequencies ω_n are shifted by an additional term $\tilde{B}^2/(4S)$. Hence, the monochromatic bounded solutions for this system with weak nonlinearity and losses in addition to small aberrations are called tilted Hermite-Gauss modes and are described by the following equations.

$$A(x,\theta) = M_n\left(\frac{x}{\sigma}\right) \exp[i(k_\perp x - \omega_n\theta)], \tag{4.10}$$

$$\omega_n = \frac{\tilde{B}^2}{4S} - \frac{2\tilde{B}}{\sigma^2}(2n+1), \tag{4.11}$$

$$\sigma^2 = \sqrt{\frac{2\tilde{B}}{\tilde{C}}}. \tag{4.12}$$

Unlike for the case with $S = 0$, these tilted Hermite-Gauss modes require the parameters $\tilde{B}$ and $\tilde{C}$ to have the same sign in order to ensure a positive waist σ. The sign of S determines the regime where the cavity might be destabilized, since $k_\perp \in \mathbb{R}$, and decomposing each mode in Eq. (4.10) into two family of solutions preserves the symmetry of emission.

$$\Gamma_n(x,\theta) = M_n\left(\frac{x}{\sigma}\right)\cos(k_\perp x)\exp\{-i\omega_n\theta\}, \tag{4.13}$$

$$\Psi_n(x,\theta) = M_n\left(\frac{x}{\sigma}\right)\sin(k_\perp x)\exp\{-i\omega_n\theta\}. \tag{4.14}$$

The modes $\Gamma_n(x,\theta)$ and $\Psi_n(x,\theta)$ alternate between even and odd functions when the modal index n is changed.

4.2 Continuation Results

Arc-length Path Continuation of the 1D MIXSEL model equation given in Eq. (2.22) is performed for the tilted Hermite-Gauss modes using the system equations and constraints as described in Section 2.3.5. Since $k_\perp$ is inversely proportional to $\sqrt{S}$, each mode becomes less oscillatory when S increases and the peak frequencies in the Fourier domain power spectrum decreases. Using direct numerical simulation, as described in Section 2.2, a stable solution is obtained for a particular set of system parameters which is used as the initial guess for continuation to analyze the stability of the mode and the effects of variations in the gain bias J_1, the effective diffraction $\tilde{B}$, the effective curvature $\tilde{C}$ and the aberration parameter S.
For continuation using pde2path [25], the residual tolerance was set at 10^{-13} taking the first 150 eigenvalues of the analytical Jacobian, given in Section 2.3.5, to check for possible bifurcations points.

4.2.1 Fundamental Gaussian Mode

The fundamental Gaussian mode can be obtained from Eq. (4.5) with modal index $n = 0$ and is shown in Fig. 4.1 along with its power spectrum in the Fourier domain. Direct numerical simulation of this mode confirms it is stable with evolution in time for parameters : $\alpha_1 = 1.5$, $\alpha_2 = 0.5$, $J_1 = 0.1541$, $J_2 = -0.12$, $s = 15$, $h = 1.98$, $\eta = 0.833$, $d = 10^{-5}$. Since, this is a Hermite-Gauss mode, the sign of the parameters $\tilde{B}$ and $\tilde{C}$ have to be opposite, as well as aberration $S = 0$.

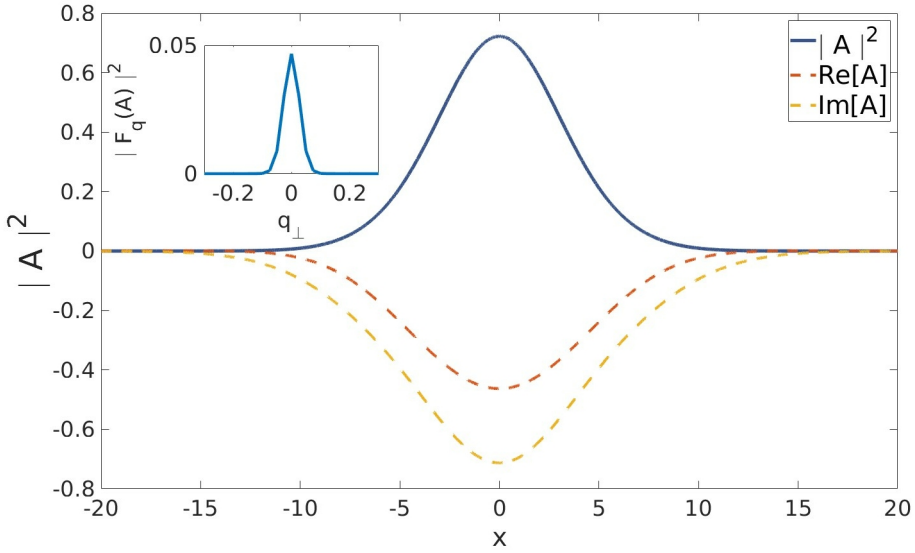

Figure 4.1: Intensity of the fundamental Gaussian mode as solution of Eq. (4.2) in a stable cavity. The real Re$\{A\}$ and imaginary Im$\{A\}$ components of the solution is shown in red and yellow dashed lines, respectively, while the intensity $|\ A\ |^2$ is shown in blue. The zoomed panel shows the corresponding power spectrum. Parameters : $\alpha_1 = 1.5$, $\alpha_2 = 0.5$, $J_1 = 0.1541$, $J_2 = -0.12$, $s = 15$, $h = 1.98$, $\eta = 0.833$, $d = 10^{-5}$, $\tilde{B} = 1.0$, $\tilde{C} = -1.5422 \times 10^{-3}$, $S = 0.0$, $\omega_0 = 0.2123$, $L_x = 40$.

In the following, we perform path continuation in the current J_1. The continuation branch for the fundamental Gaussian mode as a function of J_1/J_{th} is shown in Fig. 4.2(a) relative to the maximum of the field intensity I_{max}. The branch solutions are bi-stable in J_1, consisting of a higher intensity stable branch (solid) along with a lower intensity

unstable branch (dashed), connected via a saddle-node (cyan circle) bifurcation point, which bifurcates into the off-state as $J_1 \to J_{th}$, called threshold. The higher intensity branch also becomes unstable for increasing J_1 through a branching point (black circle) and instability increases further and multiple Andronov-Hopf (red squares) bifurcation points appear. In Fig. 4.2(b) the intensity profile of a sample solution on the stable branch is given as well as the corresponding power spectrum in Fig. 4.2(c) that shows the peak power at transverse wave number $q_\perp = 0$.

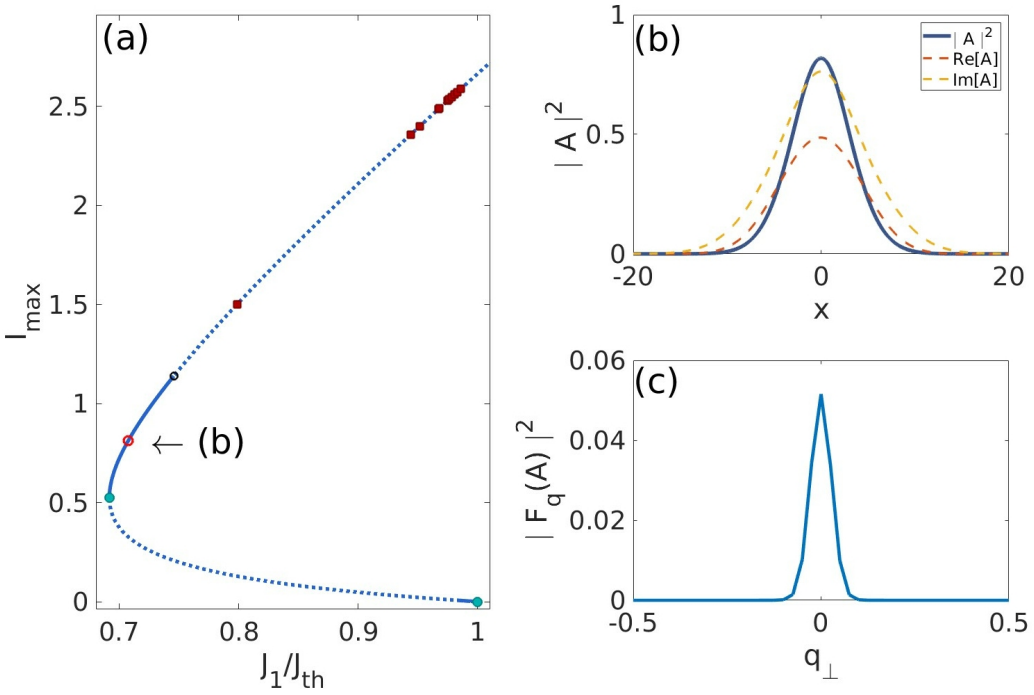

Figure 4.2: Continuation of the fundamental Gaussian mode as a function of J_1/J_{th}. (a) shows the bifurcation branch in the maximum intensity of the field I_{max}. Fold points (cyan circle), a branching point (open black circle) and Andronov-Hopf bifurcation points (red squares) separate the stable (solid blue) and unstable (dashed blue) regions of the continuation branch. The open red circle labels the position of a profile in the branch shown in panel (b). Intensity profile in panels (b) corresponds to $J_1/J_{th} = 0.7075$ and phase shift $\omega = 0.2107$. The panel (c) shows the corresponding power spectrum as a function of transverse wave number $q_\perp$.

4.2.2 Γ_0 Mode

The fundamental mode Γ_0 can be obtained numerically from Eq. (4.13) with modal index $n = 0$ and is shown in Fig. 4.3 along with the optical spectrum of the mode in Fourier space. In this figure, it can be seen from the real component $\mathrm{Re}\{\Gamma_0\}$ (red dashed line) of the field as well as the intensity (blue line) that the mode is symmetric and the tails are oscillatory due to the cosine function. Direct numerical simulation of this mode confirms that it is stable in time with parameters : $\alpha_1 = 1.5$, $\alpha_2 = 0.5$, $J_1 = 0.062$, $J_2 = -0.06$, $s = 15$, $h = 1.98$, $\eta = 0.95$, $d = 0.0001$. Therefore, path continuation is performed using this parameter set, the results of which are shown below.

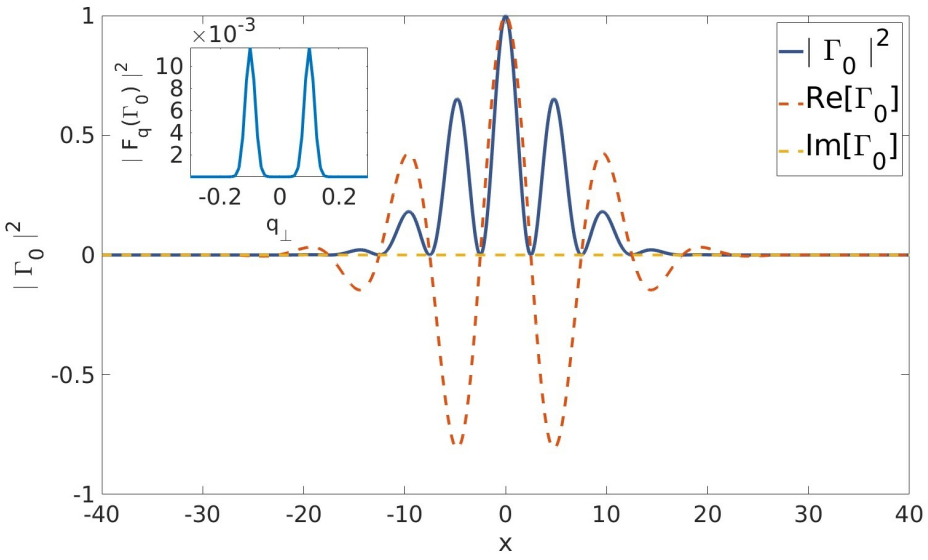

Figure 4.3: Intensity of the fundamental mode Γ_0 obtained numerically from Eq. (4.13) as a solution of Eq. (4.2). The real Re$\{\Gamma_0\}$ and imaginary Im$\{\Gamma_0\}$ components of the solution is shown in red and yellow dashed lines respectively while the intensity $|\ \Gamma_0\ |^2$ is shown in blue. The zoomed panel shows the corresponding power spectrum. Parameters : $\alpha_1 = 1.5$, $\alpha_2 = 0.5$, $J_1 = 0.062$, $J_2 = -0.06$, $s = 15$, $h = 1.98$, $\eta = 0.95$, $d = 0.0001$, $\tilde{B} = 0.7873$, $\tilde{C} = 4.97\times10^{-4}$, $S = 1.0$, $k_\perp = 0.6274$, $\omega_0 = 0.0$, $L_x = 80$.

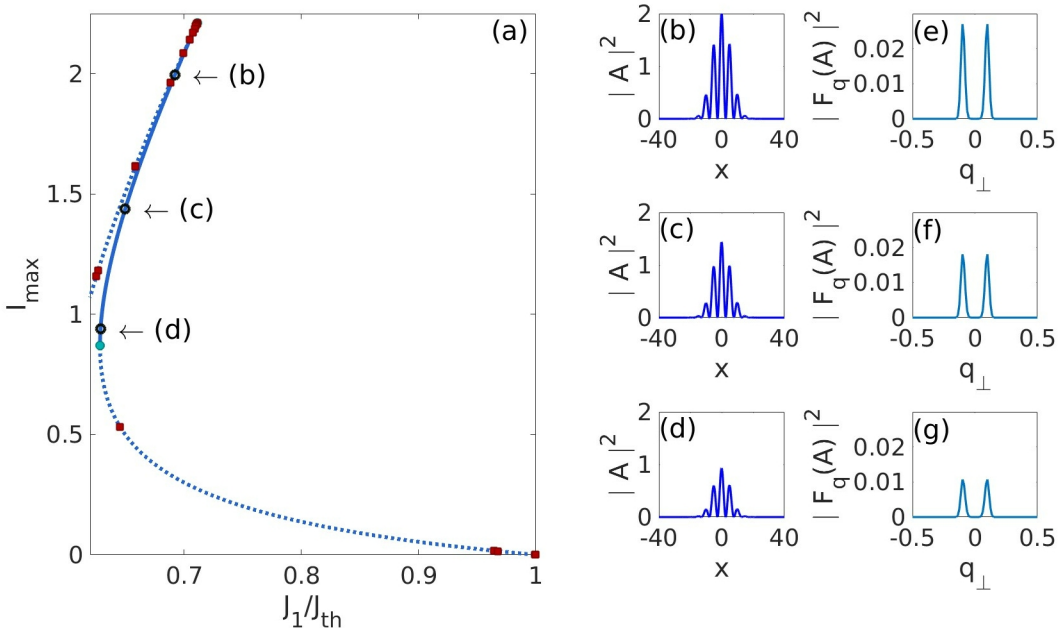

Figure 4.4: Continuation of the tilted Hermite-Gauss mode Γ_0 as a function of J_1/J_{th}. Panel (a) shows the bifurcation branch in the maximum intensity of the field I_{max}. A fold point (cyan circle) separates the stable (solid blue) and unstable (dashed blue) branches which further loses stability via Andronov-Hopf bifurcation points (red squares). Open black circles label the position of three profiles in the branch shown in panels (b-d). Intensity profiles in panels (b-d) correspond to values (0.6925, 0.6499, 0.6288) in J_1/J_{th} respectively. The panels (e-g) shows the corresponding power spectrum as a function of transverse wave number $q_\perp$. Other parameters : $\alpha_1 = 1.5$, $\alpha_2 = 0.5$, $J_2 = -0.06$, $s = 15$, $h = 1.98$, $\eta = 0.95$, $d = 0.0001$, $\tilde{B} = 0.7873$, $\tilde{C} = 4.97 \times 10^{-4}$, $S = 1.0$, $L_x = 80$.

In the following, path continuation is performed on the Γ_0 solution in some important control parameters, starting with the current J_1. The continuation branch for the Γ_0 mode as a function of J_1/J_{th} is shown in Fig. 4.4(a) in the maximum of the field intensity I_{max}. It can be seen that the mode is bi-stable in J_1, creating a high intensity stable branch (solid) along with a low intensity unstable branch (dashed) connected via a limiting saddle-node (cyan circle) bifurcation point. The high intensity branch remain stable till it loses stability through an Andronov-Hopf (red square) bifurcation point, while the lower intensity branch continues to remain unstable till it bifurcates from the off-state solution at threshold gain bias $J_1 = J_{th}$. This bi-stable bifurcation branch is a typical sub-critical diagram for this system which creates a separatrix along the branch with the stable off solution below threshold. The intensity profiles shown in Figs. 4.4(b-d) are in the stable high intensity branch for increasing values of J_1/J_{th} respectively. The intensity of the profiles increases with J_1. From the corresponding power spectrum in Figs. 4.4(e-g), it can be seen that with decreasing intensity of the field the peak power also decreases whereas the peak wave numbers remain unchanged.

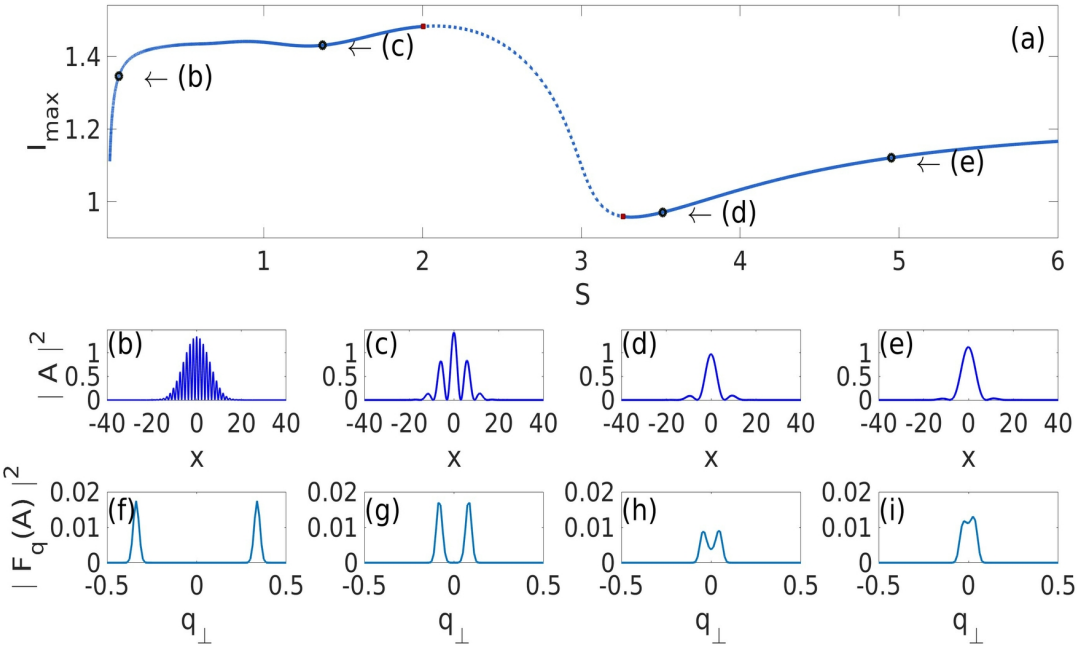

Figure 4.5: Continuation of the tilted Hermite-Gauss mode Γ_0 as a function of S. Panel (a) shows the bifurcation branch in the maximum of the field intensity I_{max}. The bifurcation branch becomes stable (solid blue) or unstable (dashed blue) via Andronov-Hopf bifurcation points (red squares). Open black circles label the position of four profiles shown in panels (b-e). These intensity profiles correspond to values (0.0869, 1.3686, 3.5111, 4.9500) in S respectively. The panels (f-i) show the corresponding power spectrum of fields (b-e) as a function of transverse wave number $q_\perp$. Other parameters : $\alpha_1 = 1.5$, $\alpha_2 = 0.5$, $J_1/J_{th} = 0.65$, $J_2 = -0.06$, $s = 15$, $h = 1.98$, $\eta = 0.95$, $d = 0.0001$, $\tilde{B} = 0.7873$, $\tilde{C} = 4.97 \times 10^{-4}$, $L_x = 80$.

The continuation branch of the Γ_0 mode as a function of the aberration parameter S is shown in Fig. 4.5(a) with respect to the maximum intensity I_{max} of the field. The mode branch is stable for smaller values of aberration S with a decay in maximum intensity I_{max} due to diffusion. Andronov-Hopf (red square) bifurcation points lead to a range of unstable solutions till the branch becomes stable again at a lower maximum intensity with further increase of S. The intensity profiles shown in Figs. 4.5(b-e) for increasing values of S indicate that the solution becomes less oscillatory for higher values of S.

In the corresponding power spectrum shown in Figs. 4.5(f-i), it can be noticed that the more oscillatory the solution (for smaller S), the higher the peak wave number. For sufficiently high values of S (see Fig. 4.5(e)), the solution loses its oscillatory tails leading to a stable single peak soliton solution. From the power spectrum in Fig. 4.5(i), it can be seen that stable asymmetric (in power spectrum) solutions also exist. Further, for small values of S, the solution is highly oscillatory with relatively higher peak wave numbers.

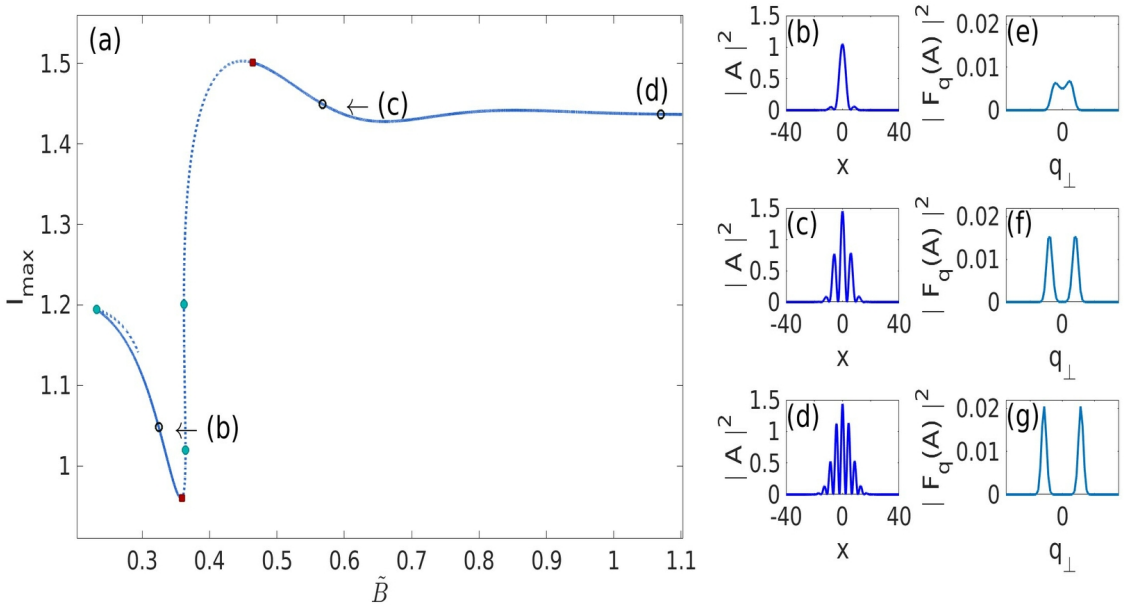

Figure 4.6: Continuation of the tilted Hermite-Gauss mode Γ_0 as a function of $\tilde{B}$. Panel (a) shows the bifurcation branch in the maximum intensity of the field I_{max}. The bifurcation branch becomes stable (solid blue) or unstable (dashed blue) via Andronov-Hopf bifurcation points (red squares) and fold points (cyan circles). Open black circles label the position of three profiles shown in panels (b-d). These intensity profiles correspond to values (0.3247, 0.5676, 1.070) in $\tilde{B}$ respectively. The panels (e-g) show the corresponding power spectrum of solutions in (b-e) as a function of transverse wave number $q_\perp$. Other parameters : $\alpha_1 = 1.5$, $\alpha_2 = 0.5$, $J_1/J_{th} = 0.65$, $J_2 = -0.06$, $s = 15$, $h = 1.98$, $\eta = 0.95$, $d = 0.0001$, $\tilde{C} = 4.97 \times 10^{-4}$, $S = 1.0$, $L_x = 80$.

The continuation branch for the Γ_0 mode as a function of $\tilde{B}$ is shown in Fig. 4.6(a) with respect to the maximum intensity I_{max} of the field. The bifurcation branch shows stable solutions for small values of $\tilde{B}$ with decaying intensity in between a saddle-node bifurcation point and an Andronov-Hopf bifurcation point which leads to instability. With further increase in $\tilde{B}$, the mode becomes stable again at a higher maximum intensity via another Andronov-Hopf bifurcation. In this region, the solution becomes increasingly oscillatory as $\tilde{B}$ increases, as shown in Figs. 4.6(c-d), along with increasing peak transverse wave number $q_\perp$ (see Figs. 4.6(f-g)). For low values of $\tilde{B}$, the stable solutions become less oscillatory with decreasing $\tilde{B}$ and the power spectrum peak wave number eventually shifts to 0 (see Fig. 4.6(e)).
The continuation branch for the Γ_0 mode as a function of $\tilde{C}$ is shown in Fig. 4.7(a) with respect to the maximum intensity I_{max} of the field. Narrow bands of stability can be observed in the branch through Andronov-Hopf bifurcation points with higher maximum intensity for smaller values of $\tilde{C}$. From the intensity profiles in Figs. 4.7(b-d), it can be seen that as $\tilde{C}$ decreases, the solutions become more oscillatory in nature. The power spectrum of these profiles shown in Figs. 4.7(e-g) confirms this as the peak

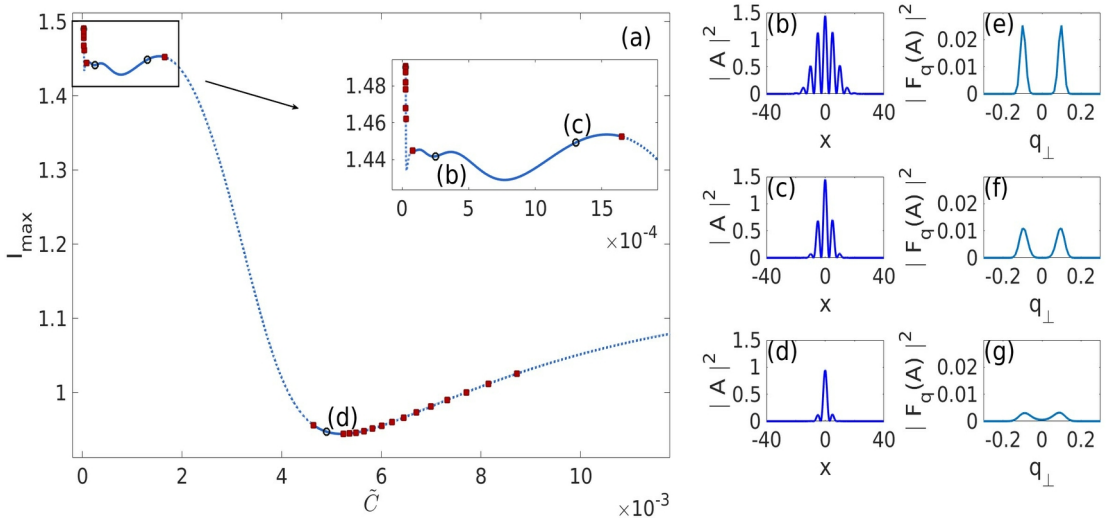

Figure 4.7: Continuation of the tilted Hermite-Gauss mode Γ_0 as a function of $\tilde{C}$. Panel (a) shows the bifurcation branch, stable (solid blue) or unstable (dashed blue), in the maximum intensity of the field I_{max}. The bifurcation branch gains narrow bands of stability via Andronov-Hopf bifurcation points (red squares) for positive values of $\tilde{C}$. Open black circles label the position of three profiles shown in panels (b-d). These intensity profiles correspond to values (0.2523, 1.3071, 4.9090)($\times 10^{-3}$) in $\tilde{C}$ respectively. The panels (e-g) show the corresponding power spectrum of fields (b-e) as a function of transverse wave number $q_\perp$. Other parameters : $\alpha_1 = 1.5$, $\alpha_2 = 0.5$, $J_1/J_{th} = 0.65$, $J_2 = -0.06$, $s = 15$, $h = 1.98$, $\eta = 0.95$, $d = 0.0001$, $\tilde{B} = 0.7873$, $S = 1.0$, $L_x = 80$.

transverse wave number also decreases accordingly. Additionally, as $\tilde{C}$ approaches 0, the bifurcation branch shifts back into $\tilde{C} > 0$ region via a saddle-node bifurcation point instead of traversing into $\tilde{C} < 0$ quadrant since the tilted Hermite-Gauss mode require $\tilde{B}$ and $\tilde{C}$ to have the same sign.

4.2.3 Ψ_0 Mode

The fundamental mode Ψ_0 is obtained from Eq. (4.14) with modal index $n = 0$ and shown in Fig. 4.8 along with its power spectrum in Fourier space. From the real component Re$\{\Psi_0\}$ (red dashed) of the field in this figure, one notices that the mode is asymmetric with oscillatory tails due to the sine function. With direct numerical simulation of this mode confirms this mode is stable in time with parameters : $\alpha_1 = 1.5$, $\alpha_2 = 0.5$, $J_1 = 0.062$, $J_2 = -0.06$, $s = 15$, $h = 1.98$, $\eta = 0.95$, $d = 0.0001$. Therefore, path continuation is performed using this parameter set, the results of which are shown below.

The continuation branch for the Ψ_0 mode as a function of the scaled current J_1/J_{th} is shown in Fig. 4.9(a) with respect to the maximum intensity I_{max} of the field. Similar to the Γ_0 mode, the sub-critical branches are bi-stable with the off-state, comprising of a high intensity stable branch and a low intensity unstable branch connected via a limiting saddle-node (cyan circle) bifurcation point. At threshold, the low intensity unstable branch bifurcates into the off solution branch via Andronov-Hopf bifurcation points, while the high intensity stable branch similarly loses stability as J_1 increases. In Figs. 4.9(b-d), the intensity profiles of stable solutions are shown where the maximum intensity of the modes decreases with decreasing J_1 and so does the peak powers in the corresponding power spectrum in Figs. 4.9(e-g).

The continuation branch for the Ψ_0 mode as a function of S is shown in Fig. 4.10(a)

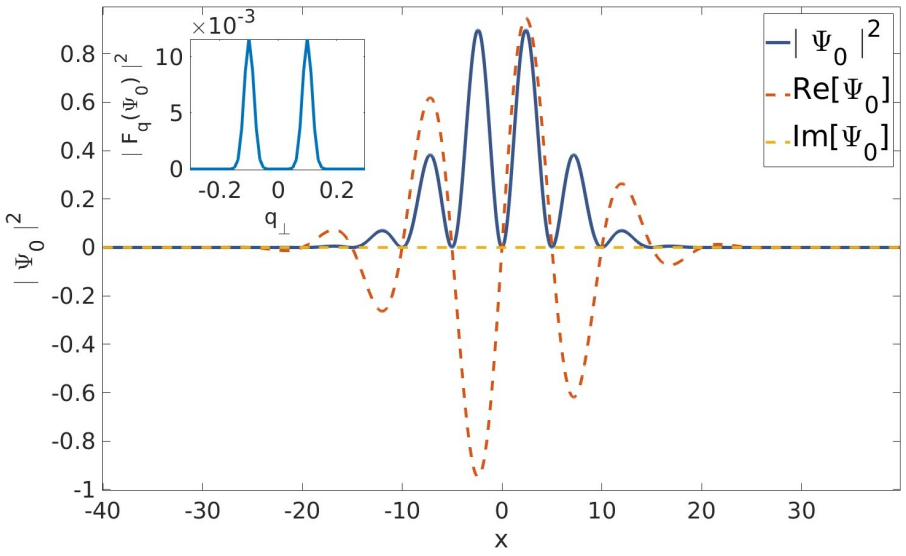

Figure 4.8: Intensity of the fundamental mode Ψ_0 obtained numerically from Eq. (4.14) as a solution of Eq. (4.2). The real Re$\{\Psi_0\}$ and imaginary Im$\{\Psi_0\}$ components of the solution is shown in red and yellow dashed lines respectively while the intensity $|\ \Psi_0\ |^2$ is shown in blue. The zoomed panel shows the corresponding power spectrum. Parameters : $\alpha_1 = 1.5$, $\alpha_2 = 0.5$, $J_1 = 0.062$, $J_2 = -0.06$, $s = 15$, $h = 1.98$, $\eta = 0.95$, $d = 0.0001$, $\tilde{B} = 0.7873$, $\tilde{C} = 4.97 \times 10^{-4}$, $S = 1.0$, $k_\perp = 0.6274$, $\omega_0 = 0.0$, $L_x = 80$.

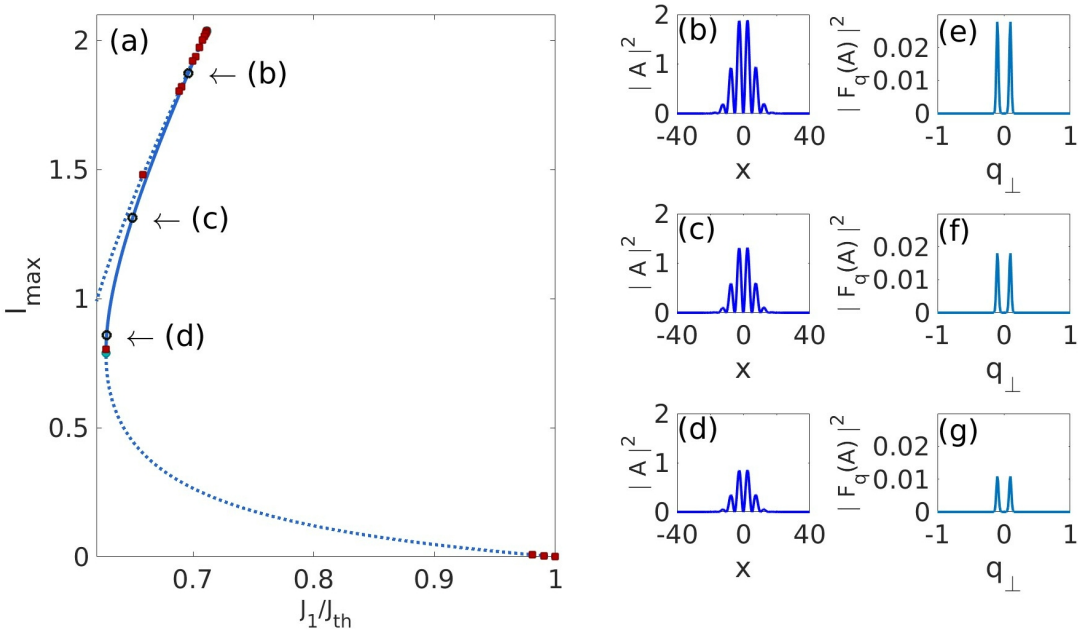

Figure 4.9: Continuation of the tilted Hermite-Gauss mode Ψ_0 as a function of J_1/J_{th}. Panel (a) shows the bifurcation branch, stable (solid blue) or unstable (dashed blue), in the maximum intensity of the field I_{max}. A fold point (cyan circle) separates the stable and unstable branches which further loses stability via Andronov-Hopf bifurcation (red square) points. Open black circles label the position of three profiles in the branch shown in panels (b-d). Intensity profiles in panels (b-d) correspond to values (0.6972, 0.6499, 0.6283) in J_1/J_{th} respectively. The panels (e-g) shows the corresponding power spectrum as a function of transverse wave number $q_\perp$. Other parameters : $\alpha_1 = 1.5$, $\alpha_2 = 0.5$, $J_2 = -0.06$, $s = 15$, $h = 1.98$, $\eta = 0.95$, $d = 0.0001$, $\tilde{B} = 0.7873$, $\tilde{C} = 4.97 \times 10^{-4}$, $S = 1.0$, $L_x = 80$.

with respect to the maximum intensity I_{max} of the field. The branch enters instability for higher values of S via multiple Andronov-Hopf (red square) bifurcation points. Within the stable region, the maximum intensity of the solution decreases for increasing S. The intensity profiles in Figs. 4.10(b-d) shows that as the aberration parameter S increases, the solutions become less oscillatory, along with decreasing peak power transverse wavenumbers in the corresponding power spectrum shown in Figs. 4.10(e-g).

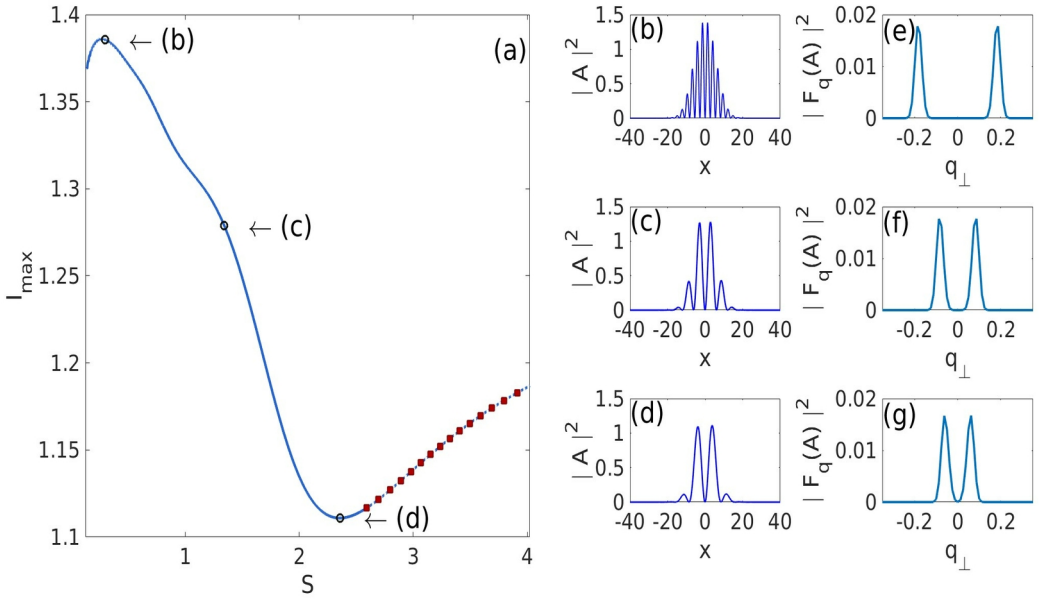

Figure 4.10: Continuation of the tilted Hermite-Gauss mode Ψ_0 as a function of S. Panel (a) shows the bifurcation branch, stable (solid blue) or unstable (dashed blue), in the maximum intensity of the field I_{max}. The bifurcation branch becomes stable via Andronov-Hopf bifurcation points (red squares) for higher values of S. Open black circles label the position of three profiles shown in panels (b-d). These intensity profiles correspond to values (0.2932, 1.3415, 2.3557) in S respectively. The panels (f-i) show the corresponding power spectrum of fields (b-e) as a function of transverse wave number $q_\perp$. Other parameters : $\alpha_1 = 1.5$, $\alpha_2 = 0.5$, $J_1/J_t h = 0.65$, $J_2 = -0.06$, $s = 15$, $h = 1.98$, $\eta = 0.95$, $d = 0.0001$, $\tilde{B} = 0.7873$, $\tilde{C} = 4.97 \times 10^{-4}$, $L_x = 80$.

The continuation branch for the Ψ_0 mode as a function of $\tilde{B}$ is shown in Fig. 4.11(a) with respect to the maximum intensity I_{max} of the field. It can be observed that the solutions remains stable for a large range of values, including small negative values of the parameter, becoming unstable via a branching point (black open circle) for negative $\tilde{B} \approx -0.2$, except for a narrow band of instability along the continuation branch. Similar to the results obtained for continuation of the Γ_0 mode, the solution becomes more oscillatory as $\tilde{B}$ increases (see Figs. 4.11(b-e)). The corresponding power spectrum in Figs. 4.11(f-i) of the illustrated solutions confirm this, since the magnitude of the peak power transverse wavenumbers increases for more oscillatory solutions. For small negative $\tilde{B}$, the solution takes the form as shown in Fig. 4.11(b) and its power spectrum (see Fig. 4.6(f) shows that it has asymmetric spectral power peaks in the Fourier domain indicating that symmetric spectral power peak solutions likely do not exist for this set of parameters. The profile shown in Fig. 4.11(c) corresponds to effective diffraction parameter $\tilde{B} \approx 0$. The intensity of the solution is only changed slightly along the continuation branch for the chosen range of values of $\tilde{B}$.

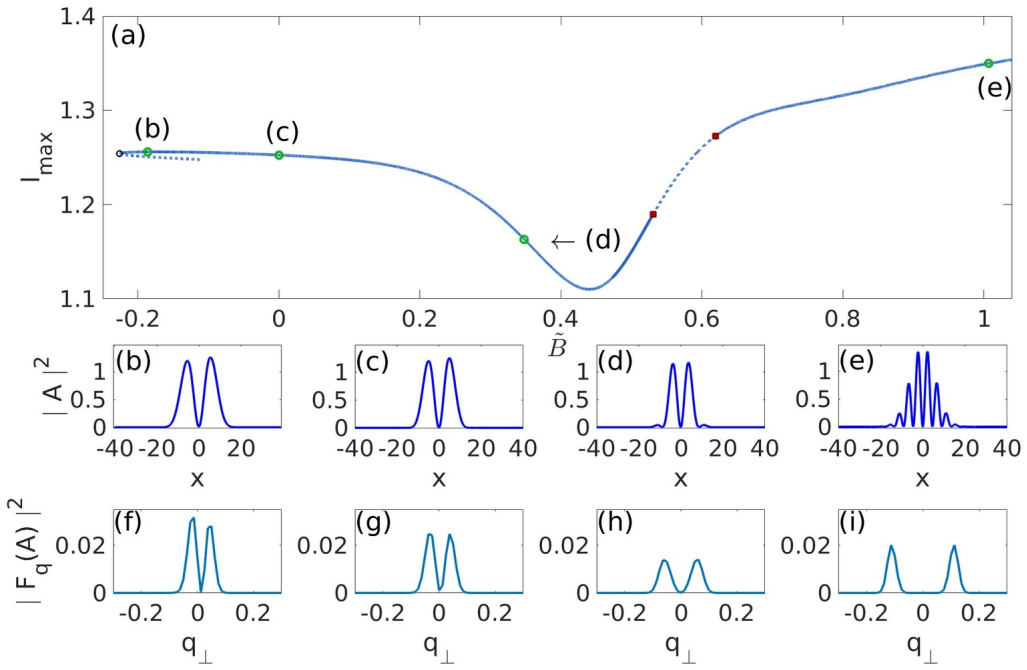

Figure 4.11: Continuation of the tilted Hermite-Gauss mode Ψ_0 as a function of $\tilde{B}$. Panel (a) shows the bifurcation branch, stable (solid blue) or unstable (dashed blue), in the maximum intensity of the field I_{max}. The bifurcation branch becomes unstable via Andronov-Hopf bifurcation points (red squares) and branching points (open black circle). Open green circles label the position of four profiles shown in panels (b-e). These intensity profiles correspond to values (-0.1859, 0.00007, 0.348, 1.007) in $\tilde{B}$ respectively. The panels (f-i) show the corresponding power spectrum of fields (b-e) as a function of transverse wave number $q_\perp$. Other parameters : $\alpha_1 = 1.5$, $\alpha_2 = 0.5$, $J_1/J_t h = 0.65$, $J_2 = -0.06$, $s = 15$, $h = 1.98$, $\eta = 0.95$, $d = 0.0001$, $\tilde{C} = 4.97 \times 10^{-4}$, $S = 1.0$, $L_x = 80$.

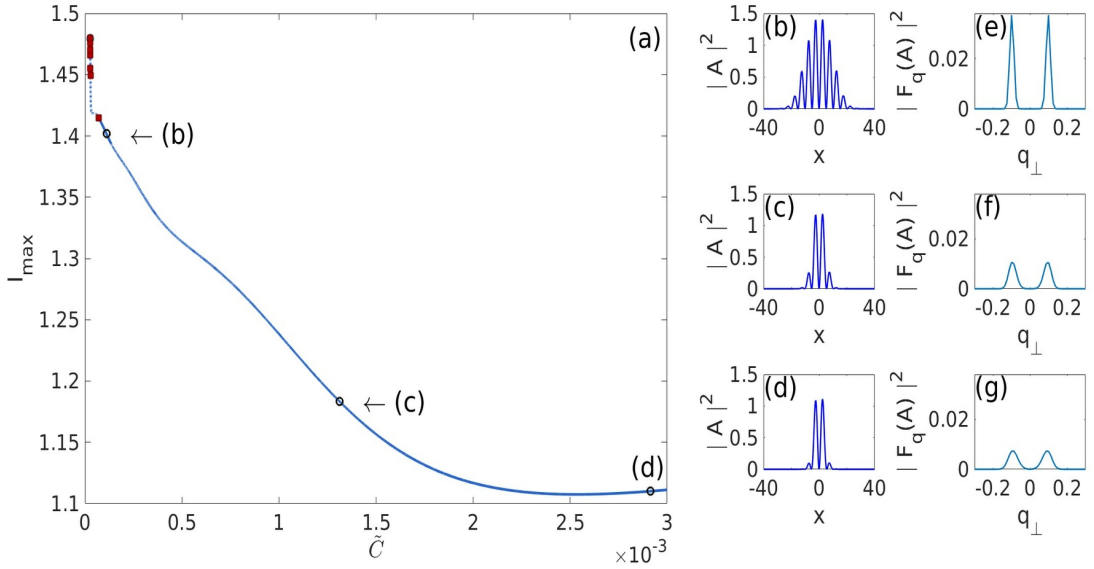

Figure 4.12: Continuation of the tilted Hermite-Gauss mode Ψ_0 as a function of $\tilde{C}$. Panel (a) shows the bifurcation branch, stable (solid blue) or unstable (dashed blue), in the maximum intensity of the field I_{max}. The bifurcation branch becomes unstable via Andronov-Hopf bifurcation points (red squares) as $\tilde{C} \to 0$. Open black circles label the positions of three profiles shown in panels (b-d). These intensity profiles correspond to values (0.1107, 1.3122, 2.9134)($\times 10^{-3}$) in $\tilde{C}$ respectively. The panels (e-g) show the corresponding power spectrum of fields (b-d) as a function of transverse wave number $q_\perp$. Other parameters : $\alpha_1 = 1.5$, $\alpha_2 = 0.5$, $J_1/J_t h = 0.65$, $J_2 = -0.06$, $s = 15$, $h = 1.98$, $\eta = 0.95$, $d = 0.0001$, $\tilde{B} = 0.7873$, $S = 1.0$, $L_x = 80$.

The continuation branch for the Ψ_0 mode as a function of $\tilde{C}$ is shown in Fig. 4.12(a) with respect to the maximum intensity I_{max} of the field. A narrow band of instability emerges on the continuation branch as $\tilde{C} \to 0$ which becomes stable through an Andronov-Hopf bifurcation (red square) as $\tilde{C}$ increases along with decreasing maximum intensity. The intensity profiles in Figs. 4.12(b-d) show that the solution becomes less oscillatory with increasing $\tilde{C}$, however in the corresponding power spectrum in Figs. 4.12(e-g), the peak wave number remains unchanged since the transverse wave vector $k_\perp$ does not depend on $\tilde{C}$ for the tilted Hermite-Gauss modes. Additionally, similar to the Γ_0 mode, the branch turns into $\tilde{C} > 0$ quadrant as it approaches 0 in order to maintain a positive value for the waist σ.

4.2.4 Γ_1 Mode

The mode Γ_1 is obtained from Eq. (4.13) with modal index $n = 1$ and shown in Fig. 4.13 along with its power spectrum in Fourier space. Unlike the fundamental mode Γ_0, this mode is asymmetric. The power spectrum of this mode shows twice the number of peaks at two different sets of peak transverse wave numbers $q_\perp$ due the increase in modal index. Direct numerical simulation of this mode confirms that it is remains stable in time with parameters : $\alpha_1 = 1.5$, $\alpha_2 = 0.5$, $J_1 = 0.062$, $J_2 = -0.06$, $s = 15$, $h = 1.98$, $\eta = 0.95$, $d = 0.0001$. Therefore, path continuation is performed using this parameter set, the results of which are shown below.

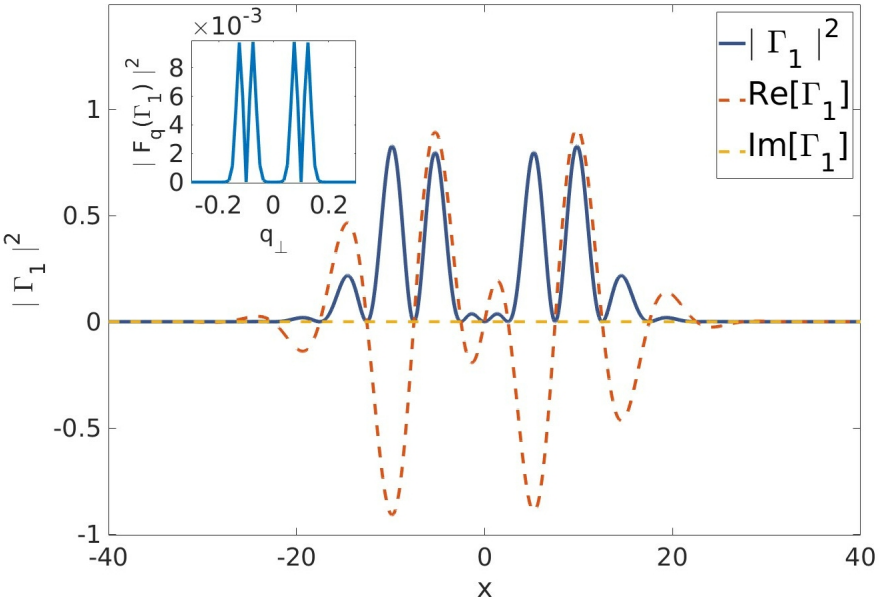

Figure 4.13: Intensity of the mode Γ_1 obtained numerically from Eq. (4.13) as a solution of Eq. (4.2). The real Re$\{\Gamma_1\}$ and imaginary Im$\{\Gamma_1\}$ components of the solution is shown in red and yellow dashed lines respectively while the intensity $|\ \Gamma_1\ |^2$ is shown in blue. The zoomed panel shows the corresponding power spectrum. Parameters : $\alpha_1 = 1.5$, $\alpha_2 = 0.5$, $J_1 = 0.062$, $J_2 = -0.06$, $s = 15$, $h = 1.98$, $\eta = 0.95$, $d = 0.0001$, $\tilde{B} = 0.7873$, $\tilde{C} = 4.97 \times 10^{-4}$, $S = 1.0$, $k_\perp = 0.6274$, $\omega_0 = 0.0$, $L_x = 80$.

The continuation branch for the Γ_1 mode as a function of the scaled current J_1/J_{th} is shown in Fig. 4.14(a) with respect to the maximum intensity I_{max} of the field. Similar to the two fundamental modes, this mode also forms sub-critical branches that are bi-stable with the off solution, and the intensity of the stable branch solution increases for increase

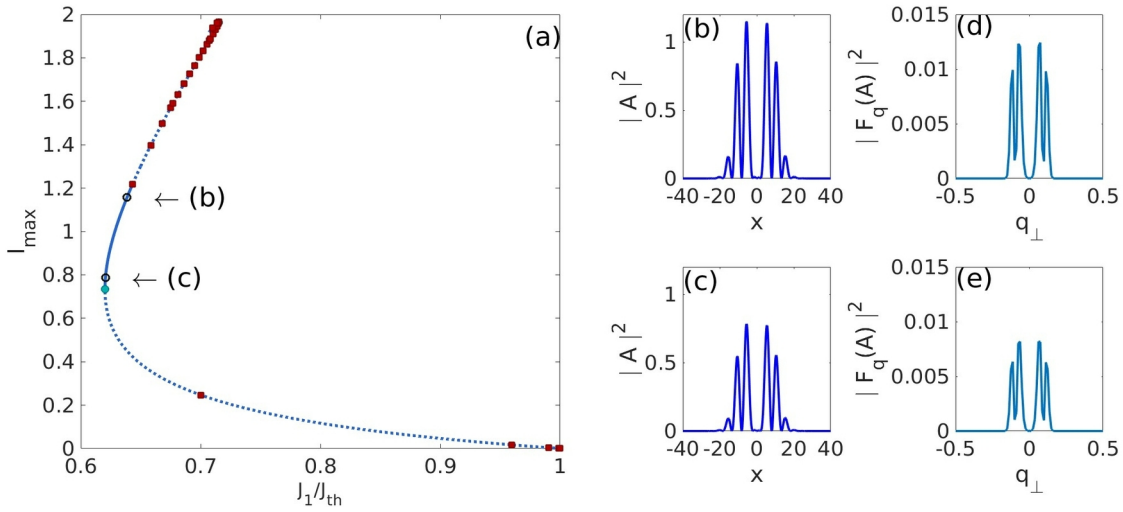

Figure 4.14: Continuation of the tilted Hermite-Gauss mode Γ_1 as a function of J_1/J_{th}. Panel (a) shows the bifurcation branch in the maximum intensity of the field I_{max}. A fold point (cyan circle) separates the stable (solid blue) or unstable (dashed blue) branches which further loses stability via Andronov-Hopf bifurcations (red square). Open black circles label the position of two profiles in the branch shown in panels (b-c). Intensity profiles in panels (b-c) correspond to values (0.6387,0.6207) in J_1/J_{th} respectively. The panels (d-e) show the corresponding power spectrum of solutions in panels (b-c) as a function of transverse wave number $q_\perp$. Other parameters : $\alpha_1 = 1.5$, $\alpha_2 = 0.5$, $J_2 = -0.06$, $s = 15$, $h = 1.98$, $\eta = 0.95$, $d = 0.0001$, $\tilde{B} = 0.7873$, $\tilde{C} = 4.97 \times 10^{-4}$, $S = 1.0$, $L_x = 80$.

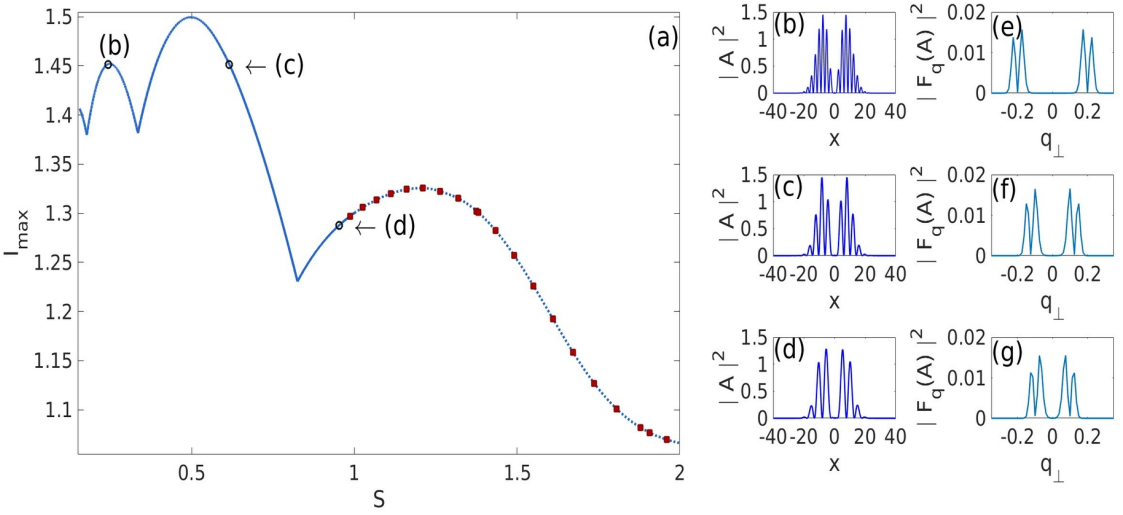

Figure 4.15: Continuation of the tilted Hermite-Gauss mode Γ_1 as a function of S. Panel (a) shows the bifurcation branch, stable (solid blue) or unstable (dashed blue), in the maximum intensity of the field I_{max}. The branch loses stability via Andronov-Hopf bifurcations (red squares) for higher values of S. Open black circles label the position of three profiles in the branch shown in panels (b-d). Intensity profiles in panels (b-d) correspond to values (0.2438, 0.6157, 0.9527) in S respectively. The panels (e-g) shows the corresponding power spectrum of the solutions in panels (b-d) as a function of transverse wave number $q_\perp$. Other parameters : $\alpha_1 = 1.5$, $\alpha_2 = 0.5$, $J_1/J_{th} = 0.65$, $J_2 = -0.06$, $s = 15$, $h = 1.98$, $\eta = 0.95$, $d = 0.0001$, $\tilde{B} = 0.7873$, $\tilde{C} = 4.97 \times 10^{-4}$, $L_x = 80$.

in J_1. However, for this higher order mode, the branch is stable for only a narrow range of values, then it becomes unstable passing through a saddle-node (cyan circle) bifurcation

point and finally bifurcating at threshold, $J_1 = J_{th}$ into the off-state solution. The saddle-node bifurcation point separating the two bi-stable branches occurs at a smaller value of J_1 relative to those for the fundamental modes Γ_0 and Ψ_0. Fig. 4.14(b-c) shows the intensity profiles of two stable solutions along with their corresponding power spectrum in Fig. 4.14(d-e).

The continuation branch for the Γ_1 mode as a function of S is shown in Fig. 4.15(a) with respect to the maximum intensity I_{max} of the field. Similar to the continuation results of the asymmetric fundamental mode Ψ_0 in parameter S, the branch for this mode becomes unstable through Andronov-Hopf bifurcations (red squares) for higher values of S. Within the stable region of the branch the maximum intensity I_{max} oscillates for small S due to the symmetric nature of the intensity profile and then decreases with further increase of S. From the intensity profiles in Fig. 4.15(b-d), it is seen that the stable solutions become more oscillatory for smaller values of S along with the increase of the peak wave numbers in the corresponding power spectrum given in Fig. 4.15(e-g). Although the difference between the two set of symmetric peak wavenumbers remain constant.

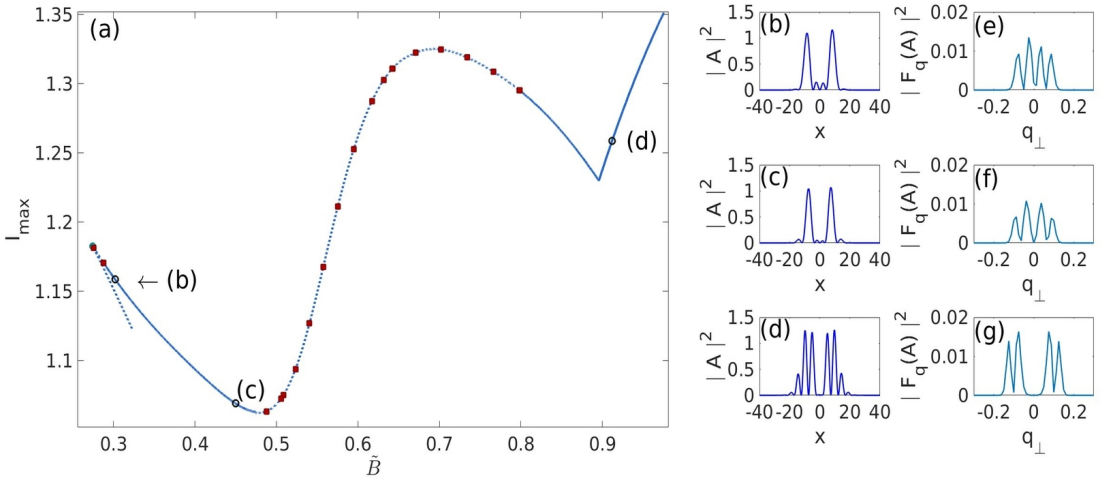

Figure 4.16: Continuation of the tilted Hermite-Gauss mode Γ_1 as a function of $\tilde{B}$. Panel (a) shows the bifurcation branch, stable (solid blue) or unstable (dashed blue), in the maximum intensity of the field I_{max}. The branch loses stability via Andronov-Hopf bifurcations (red squares). Open black circles label the position of three profiles in the branch shown in panels (b-d). Intensity profiles in panels (b-d) correspond to values (0.3020, 0.450, 0.91197) in $\tilde{B}$ respectively. The panels (e-g) shows the corresponding power spectrum of the solutions in panels (b-d) as a function of transverse wave number $q_\perp$. Other parameters : $\alpha_1 = 1.5$, $\alpha_2 = 0.5$, $J_1/J_{th} = 0.65$, $J_2 = -0.06$, $s = 15$, $h = 1.98$, $\eta = 0.95$, $d = 0.0001$, $\tilde{C} = 4.97 \times 10^{-4}$, $S = 1.0$, $L_x = 80$.

The continuation branch for the Γ_1 mode as a function of $\tilde{B}$ is shown in Fig. 4.16(a) with respect to the maximum intensity I_{max} of the field. From the bifurcation branch, it is observed that the solution is stable for two range of values in $\tilde{B}$. For larger $\tilde{B}$, the stable solutions are more oscillatory, along with larger transverse wave numbers in Fourier domain as can be seen from the intensity profile given in Fig. 4.16(d) and its corresponding power spectrum in Fig. 4.16(g). In case of smaller values of $\tilde{B}$, the stable solutions are less oscillatory as seen in Figs. 4.16(b-c) and correspondingly the peak wavenumbers in the Fourier space also decreases in Fig. 4.16(e-f). The exemplary solution and its power spectrum shown in Fig. 4.16(b,e) confirms the presence of stable asymmetric peak power solutions for this system.

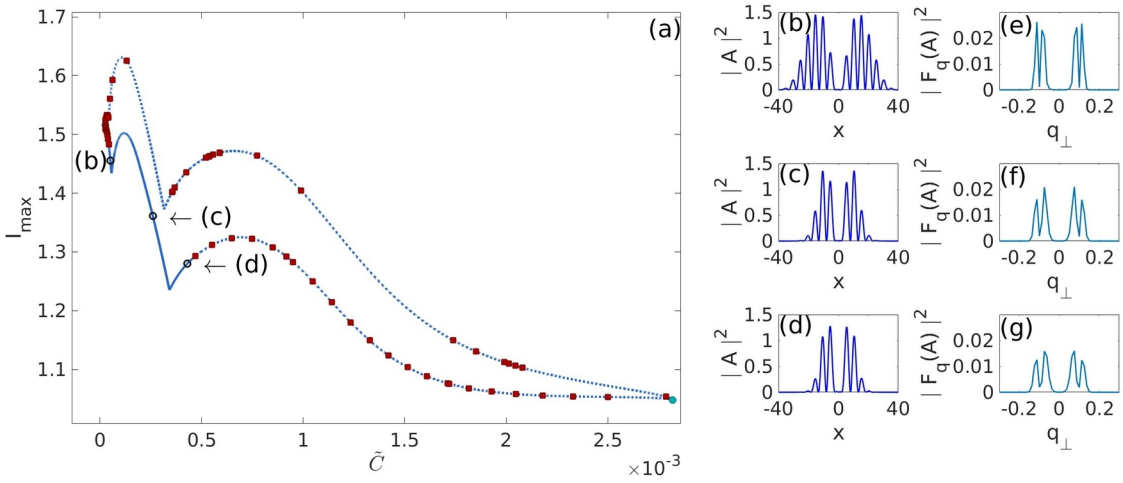

Figure 4.17: Continuation of the tilted Hermite-Gauss mode Γ_1 as a function of $\tilde{C}$. Panel (a) shows the bifurcation branch, stable (solid blue) or unstable (dashed blue), in the maximum intensity of the field I_{max}. The branch loses stability via Andronov-Hopf bifurcations (red squares). Open black circles label the position of three profiles in the branch shown in panels (b-d). Intensity profiles in panels (b-d) correspond to values $(0.5051,\ 2.5972,\ 4.2856)(\times 10^{-4})$ in $\tilde{C}$ respectively. The panels (e-g) shows the corresponding power spectrum of the solutions in panels (b-d) as a function of transverse wave number $q_\perp$. Other parameters : $\alpha_1 = 1.5$, $\alpha_2 = 0.5$, $J_1/J_{th} = 0.65$, $J_2 = -0.06$, $s = 15$, $h = 1.98$, $\eta = 0.95$, $d = 0.0001$, $\tilde{B} = 0.7873$, $S = 1.0$, $L_x = 80$.

The continuation branch for the Γ_1 mode as a function of $\tilde{C}$ is shown in Fig. 4.17(a) with respect to the maximum intensity I_{max} of the field. From the bifurcation diagram, it can be seen that the branch remains stable only for a narrow range of $\tilde{C}$ values, which eventually enters instability by Andronov-Hopf bifurcation points (red squares). Compared to the stable solutions obtained for the fundamental modes Γ_0 and Ψ_0, this higher order mode has stable solutions for lower values of the potential $\tilde{C}$ by one order of magnitude. As can be seen in Figs. 4.17(b-d), the intensity profile of these stable solutions become more oscillatory as $\tilde{C} \to 0$, while the peak wavenumbers in the corresponding power spectrum (see Figs. 4.17(e-g)) does not shift. However, some modulation is the power spectrum can be observed with the broadening of the peaks with increasing $\tilde{C}$, similar to other modes. The continuation branch remains within the $\tilde{C} > 0$ quadrant as required by tilted Hermite-Gauss modes.

4.2.5 Higher Order Modes

The higher order mode Γ_2 is obtained from Eq. (4.13) with modal index $n = 2$ and shown in Fig. 4.18 along with its power spectrum in Fourier space. The real component $\mathrm{Re}\{\Gamma_2\}$ of this mode is symmetric and the power spectrum has thrice the number of peaks, compared to the fundamental modes, at two different sets of conjugate peak transverse wave numbers $q_\perp$ corresponding to the modal index. Direct numerical simulation of this mode shows that it is quasi-stable with evolution in time given the parameters : $\alpha_1 = 1.5$, $\alpha_2 = 0.5$, $J_1 = 0.0639$, $J_2 = -0.06$, $s = 15$, $h = 1.98$, $\eta = 0.95$, $d = 0.0001$. Performing path continuation using this mode as initial solution does not yield stable solutions for the range of parameters used for other modes, however, this confirms the existence of unstable higher order modes for the given system under consideration.

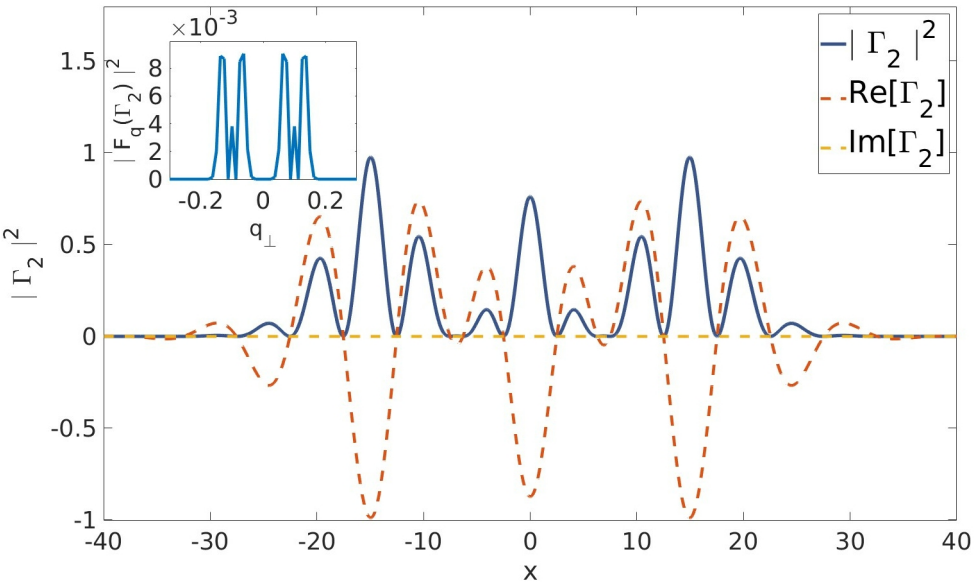

Figure 4.18: Intensity of the quasi-stable mode Γ_2 obtained numerically from Eq. (4.14) as a solution of Eq. (4.2). The real $\mathrm{Re}\{\Gamma_2\}$ and imaginary $\mathrm{Im}\{\Gamma_2\}$ components of the solution is shown in red and yellow dashed lines respectively while the intensity $\mid \Gamma \mid^2$ is shown in blue. The zoomed panel shows the corresponding power spectrum. Parameters : $\alpha_1 = 1.5$, $\alpha_2 = 0.5$, $J_1 = 0.0639$, $J_2 = -0.06$, $s = 15$, $h = 1.98$, $\eta = 0.95$, $d = 0.0001$, $\tilde{B} = 0.7873$, $\tilde{C} = 2.486 \times 10^{-4}$, $S = 1.0$, $k_\perp = 0.6274$, $\omega_0 = 0.001$, $L_x = 80$.

5 One-Dimensional Pattern Formation

5.1 Linear Stability Analysis

Stability analysis of the 1D MIXSEL model given in Eq. (2.22) for plane wave solutions against small perturbation can be performed by linearization of the corresponding equation and finding the eigenvalues of the resultant coefficient matrix of the system. For this analysis, the wavefront curvature parameter in the potential term in Eq. (2.22), is assumed to be zero ($\tilde{C} = 0$).
The 1D system equation in consideration, therefore, becomes

$$\begin{aligned}\frac{\partial A(x,\theta)}{\partial \theta} = \Big[(1 - i\alpha_1)\, J_1\, g\,(\mid A(x,\theta)\mid^2) \;+\; (1 - i\alpha_2)\, J_2\, g\,(s \mid A(x,\theta)\mid^2) - \; k \\ + \Big(d + i\tilde{B}\Big)\, \frac{\partial^2}{\partial x^2} \;+\; i\, S\, \frac{\partial^4}{\partial x^4}\Big] A(x,\theta).\end{aligned} \tag{5.1}$$

Using a plane wave ansatz for the transverse profile of the inter-cavity field, $A(x,\theta) = u(\theta)\exp\{i(qx - \omega\theta)\}$, where $u(\theta) \in \mathbb{C}$ is the amplitude profile, q is the transverse wavevector and ω denotes the frequency of the solution. With this substitution, the system equation turns into a nonlinear ODE

$$\begin{aligned}\frac{\mathrm{d}u}{\mathrm{d}\theta} = \Big[i\,\omega - \; k \; + (1 - i\alpha_1)\, J_1\, g\,(\mid u\mid^2) \;+\; (1 - i\alpha_2)\, J_2\, g\,(s \mid u\mid^2) \\ - d\, q^2 - i\, \tilde{B}\, q^2 + i\, S\, q^4\Big] u.\end{aligned} \tag{5.2}$$

Splitting the complex-valued $u(\theta)$ into its real and imaginary components as $u = u_1 + iu_2$, where $(u_1, u_2) \in \mathbb{R}$ and separating the real and imaginary terms results into two equivalent equations

$$\begin{aligned}\frac{\mathrm{d}u_1}{\mathrm{d}\theta} = (u_1 + \alpha_1 u_2)\, J_1\, g\,({u_1}^2 + {u_2}^2) + (u_1 + \alpha_2 u_2)\, J_2\, g\,(s({u_1}^2 + {u_2}^2)) \\ - \omega\, u_2 \;-\; k\, u_1 - \; d\, q^2\, u_1 + \tilde{B}\, q^2\, u_2 - S\, q^4\, u_2,\end{aligned} \tag{5.3}$$

$$\begin{aligned}\frac{\mathrm{d}u_2}{\mathrm{d}\theta} = (u_2 - \alpha_1 u_1)\, J_1\, g\,({u_1}^2 + {u_2}^2) + (u_2 - \alpha_2 u_1)\, J_2\, g\,(s({u_1}^2 + {u_2}^2)) \\ + \omega\, u_1 \;-\; k\, u_2 - \; d\, q^2\, u_2 + \tilde{B}\, q^2\, u_1 - S\, q^4\, u_1.\end{aligned} \tag{5.4}$$

For simplicity, the above two system equations can be expressed in matrix form, dividing the linear and nonlinear terms into two operators $\hat{L}$ and $\hat{N}$, respectively, as

$$\frac{\mathrm{d}U}{\mathrm{d}\theta} = \hat{N}(U) + \hat{L}U, \tag{5.5}$$

where the system variable vector U, linear operator $\hat{L}$, nonlinear operator $\hat{N}(U)$ are given as

$$U = \begin{pmatrix} u_1 \\ u_2 \end{pmatrix}, \quad \hat{L} = \begin{pmatrix} -d\, q^2 & \tilde{B}\, q^2 - S\, q^4 \\ -\tilde{B}\, q^2 + S\, q^4 & -d\, q^2 \end{pmatrix}, \quad \hat{N}(U) = \begin{pmatrix} f_1 \\ f_2 \end{pmatrix}. \tag{5.6}$$

The components f_1 and f_2 are derived from the effective nonlinearity function of Eq. (2.22), $f(P)$ for a pulse $P \in \mathbb{R}$:

$$f(P) = (1 - i\alpha_1)\, J_1\, g\,(P) \;+\; (1 - i\alpha_2)\, J_2\, g\,(s\,P) - k. \tag{5.7}$$

The nonlinear function $f(P)$ allows for spatially uniform steady solutions of the form, $A(x,\theta) = \sqrt{P}\exp\{i\omega\theta\}$, where ω is defined as the carrier frequency. These solutions solve the following equations

$$\mathrm{Re}\{f(P)\}P = [J_1\, g(P) + J_2\, g(s\,P) - k]P = 0, \tag{5.8}$$

$$\mathrm{Im}\{f(P)\} = \alpha\, J_1\, g(P) + \alpha\, J_2\, g(s\,P) = \omega. \tag{5.9}$$

The system equation is linearized for small perturbation using the Jacobian matrix, J_P, of the nonlinear operator, $\hat{N}$, obtained from the approximation in the first order of a Taylor expansion around these uniform steady state pulse solutions. Using the conditions in Eqs. (5.8) and (5.9), on the nonlinear terms of the equivalent system equations given in Eqs. (5.3) and (5.4), one obtains the following expressions for the Jacobian J_P :

$$J_P = \begin{pmatrix} \frac{\partial f_1}{\partial u_1} & \frac{\partial f_1}{\partial u_2} \\ \frac{\partial f_2}{\partial u_1} & \frac{\partial f_2}{\partial u_2} \end{pmatrix} = \begin{pmatrix} f_{11} & f_{12} \\ f_{21} & f_{22} \end{pmatrix}, \text{ with} \tag{5.10}$$

$$\begin{aligned}
f_{11} &= (u_1 + u_2\alpha_1)\, J_1\, \frac{\partial g(I)}{\partial u_1} + (u_1 + u_2\alpha_2)\, J_2\, \frac{\partial g(s\,I)}{\partial u_1}, \\
f_{12} &= (u_1 + u_2\alpha_1)\, J_1\, \frac{\partial g(I)}{\partial u_2} + (u_1 + u_2\alpha_2)\, J_2\, \frac{\partial g(s\,I)}{\partial u_2}, \\
f_{21} &= (u_2 - u_1\alpha_1)\, J_1\, \frac{\partial g(I)}{\partial u_1} + (u_2 - u_1\alpha_2)\, J_2\, \frac{\partial g(s\,I)}{\partial u_1}, \\
f_{22} &= (u_2 - u_1\alpha_1)\, J_1\, \frac{\partial g(I)}{\partial u_2} + (u_2 - u_1\alpha_2)\, J_2\, \frac{\partial g(s\,I)}{\partial u_2},
\end{aligned} \tag{5.11}$$

where $I = {u_1}^2 + {u_2}^2$.
The resultant coefficient matrix, $\hat{A}$, is obtained by combining the nonlinear Jacobian matrix, J_P and the linear operator, $\hat{L}$, for a small perturbation from the steady state solution

$$\hat{A} = \begin{pmatrix} -d\,q^2 + f_{11} & \tilde{B}\,q^2 - S\,q^4 + f_{12} \\ -\tilde{B}\,q^2 + S\,q^4 + f_{21} & -d\,q^2 + f_{22} \end{pmatrix}. \tag{5.12}$$

To solve the system of equations for small perturbation ΔU, given by

$$\frac{\mathrm{d}\Delta U}{\mathrm{d}\theta} = \hat{A}\,\Delta U, \tag{5.13}$$

the matrix method is used to find the eigenvalues, as follows

$$|\,\hat{A} - \lambda\hat{I}\,| = 0, \tag{5.14}$$

where $\hat{I}$ is the identity matrix. The eigenvalues $\lambda = (\lambda_1, \lambda_2)$ gives insight into the instabilities present in the system for plane periodic solutions. The real component of the eigenvalues when negative indicates instability for the set of parameters chosen.
In Fig. 5.1 the real parts of the eigenvalues (λ_1, λ_2) are plotted as a function of the transverse wavevector q. The left panel in the figure shows an unstable band at the long wavelength regime in the range $q \in [0, q_M]$. This corresponds to modulational

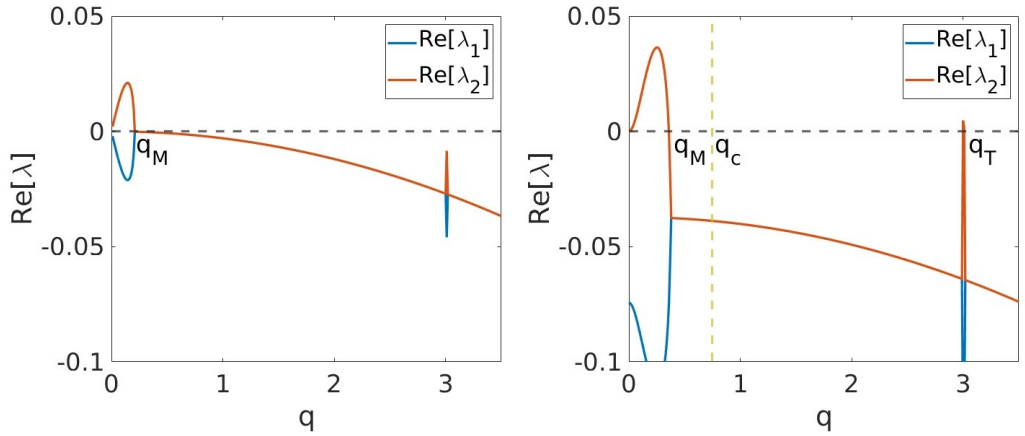

Figure 5.1: Dispersion relation of the uniform steady solutions for two different values of the bias current, J_1. The left panel corresponds to minimum intensity ($I = 0.37$) for the parameter set with $J_1/J_{th} = 0.661$. A band of long wavelength modulational instability is present in the range $q \in [0, q_M]$. The real component of the eigenvalues in the right panel is obtained for uniform intensity ($I = 1.0$) and $J_1/J_{th} = 0.78$. Along with the low frequency modulational instability, another narrow unstable band arises above low frequency cut-off (yellow dashed line), $q > q_c$, corresponding to Turing instability at $q_T = 3.0$. Parameters : $\tilde{B} = 1.0$, $\tilde{C} = 0$, $S = 0.11$, $\alpha_1 = 1.5$, $\alpha_2 = 0.5$, $J_2 = -0.12$, $k = 0.1$, $s = 15$, $d = 0.003$.

instability at low frequency range for the set of parameters chosen for the solution at minimum value of $J_1 = 0.145$, i.e., $J_1/J_{th} = 0.661$. However, it can be observed that another narrow band emerges at the finite wavelength regime in the real component of the stability eigenvalues but remains negative for the chosen parameters.
The right panel in Fig. 5.1, on the other hand, it is observed that for $J_1 = 0.171$, i.e., $J_1/J_{th} = 0.78$ and uniform intensity $I = 1.0$, a narrow unstable band at short wavelength along with the expected modulational instability at long wavelength. This unstable band corresponds to Turing instability that emerges due to the presence of the Bilaplacian operator approximating aberrations in Eq. (2.17) which renders possible the appearance of a Turing bifurcation. Turing instability in the eigenvalues at $q_T = 3.0$ in the figure indicates to the formation of modulated patterns. The occurrence of this Turing bifurcation depends on the parameters $\tilde{B}$ and S and is related to the Turing wavevector q_T as

$$q_T \simeq \sqrt{\frac{\tilde{B}}{S}}. \tag{5.15}$$

In order to control the development of one form of instability, i.e., to suppress the modulational instability such that Turing instability leads to the emergence of modulated patterns in the solution, the finite transverse size $L_\perp$ of the system is used which is possible due to the inherent discretization of the allowed wavevectors in a system. A low frequency cut-off $q_c = 2\pi/L_\perp$ is chosen such that it is larger than the maximum of the long wavelength modulational instability band, i.e., $q_M < q_c$. This results in formation of patterns in the solution only due to Turing instability since the modulational instability band occurs below the cut-off frequency q_c imposed by the finite size of the system and low spatial frequencies are inhibited.
To perform continuation on this system to enable formation of patterns due to Turing instability by tuning the transverse size $L_\perp$, one has to take into account the periodic boundary conditions imposed on the domain. Therefore, a resonant condition has to be

satisfied by the chosen low frequency cut-off q_c and the Turing wavevector q_T as

$$q_T = n\, q_c, \quad \text{with } n \in \mathbb{N}. \tag{5.16}$$

In Fig. 5.1, the right panel which satisfies the condition for Turing instability to arise in the system, the yellow dashed line marks the chosen low frequency cut-off at $q_c = 0.75$. With $q_T = 3.0$, the above resonant condition is satisfied as $q_T/q_c = 4$ and the finite transverse size is $L_\perp = 8.3776$. Setting the parameters according to these above condition, the emergence of modulated patterns is investigated by path continuation.

5.2 Continuation Results

Arc-length Path Continuation is performed on the 1D MIXSEL model as given in Eq. (2.22) for steady periodic and continuous wave solutions to analyze their stability as well as emergence of transversal patterns using the system equations and auxiliary conditions described in Section 2.3.5.

Firstly, the existence of stable periodic solutions for the system is confirmed through direct numerical analysis as described in Section 2.2. Continuation of such a periodic solution is performed to view the effects of variation in the gain bias J_1 and the effective curvature potential parameter $\tilde{C}$ on the stability of the solution.

Next, the formation of transversal patterns due to Turing instability is investigated by defining the system with parameters as described in the stability analysis above. The modulation of these pattern solutions under the effects of tuning the other system parameters is also considered.

For continuation using pde2path [25] package, the residual tolerance is set at 10^{-13} and the first 150 eigenvalues of the analytical Jacobian, given in Section 2.3.5, are used to check for possible bifurcation points along the branch.

5.2.1 Periodic Solution

A periodic solution of the form $A(x, \theta) = A_0 \cos(k_0 x) \exp\{i\omega\theta\}$ is chosen as an initial guess with constant amplitude $A_0 = 1.5$, wavevector $k_0 = 0.55$ and oscillation frequency ω to verify the existence of stable periodic solutions to the system equation given in Eq. (5.1). The transverse length of the system is chosen to be $L_\perp = 80$ for convenience.

The continuation results in the parameter J_1 is shown in Fig. 5.2, where the panel (a) shows a narrow band of stable solutions in the high intensity regime. It shows a narrow region of stable periodic solutions for a range of values of J_1 in the higher intensity or upper branch of the bifurcation diagram. The intensity profile of a sample stable periodic solution is shown in Fig. 5.2(b) along with its power spectrum in Fig. 5.2(c) which shows two peak powers at low spectral frequencies. The wavefront curvature parameter $\tilde{C}$ is assumed to be zero.

Furthermore, to investigate the effects of adding the potential term to the system, path continuation is performed in the effective curvature parameter $\tilde{C}$, the results of which are shown in Fig. 5.3. The continuation branch shown in Fig. 5.3(a) shows that the periodic solution is stable for small magnitudes of the effective curvature parameter $\tilde{C}$ for both negative and positive potential added to the system.

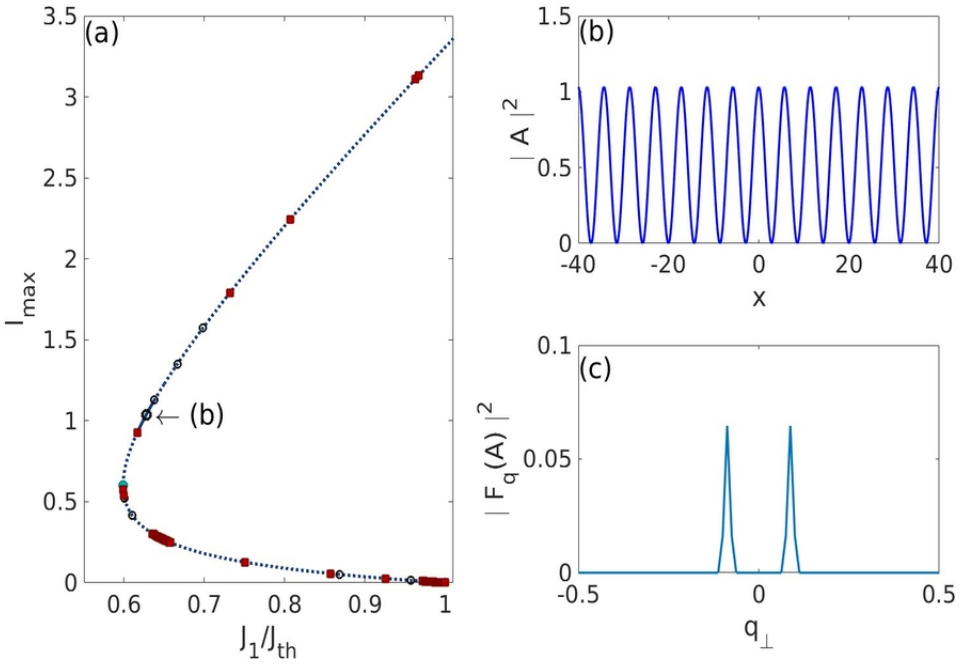

Figure 5.2: Continuation of a periodic solution as a function of J_1/J_{th}. Panel (a) show the solution branch, stable (solid blue) and unstable (dashed blue), in the maximum intensity of the solution I_{max}. A fold point (cyan circle), several branching points (black open circles) and Andronov-Hopf bifurcation points (red squares) are present along the branch. The intensity profile of the point marked (b), corresponding to $J_1/J_{th} = 0.6275$ and frequency shift $\omega = 0.2063$, in the narrow stable region of the branch is shown in panel (b). Panel (c) shows the power spectrum of the stable periodic solution shown in (b). Parameters : $\alpha_1 = 1.5$, $\alpha_2 = 0.5$, $J_2 = -0.06$, $s = 15$, $h = 1.98$, $\eta = 0.95$, $d = 0.0001$, $\tilde{B} = 0.7873$, $\tilde{C} = 0.0$, $S = 1.0$.

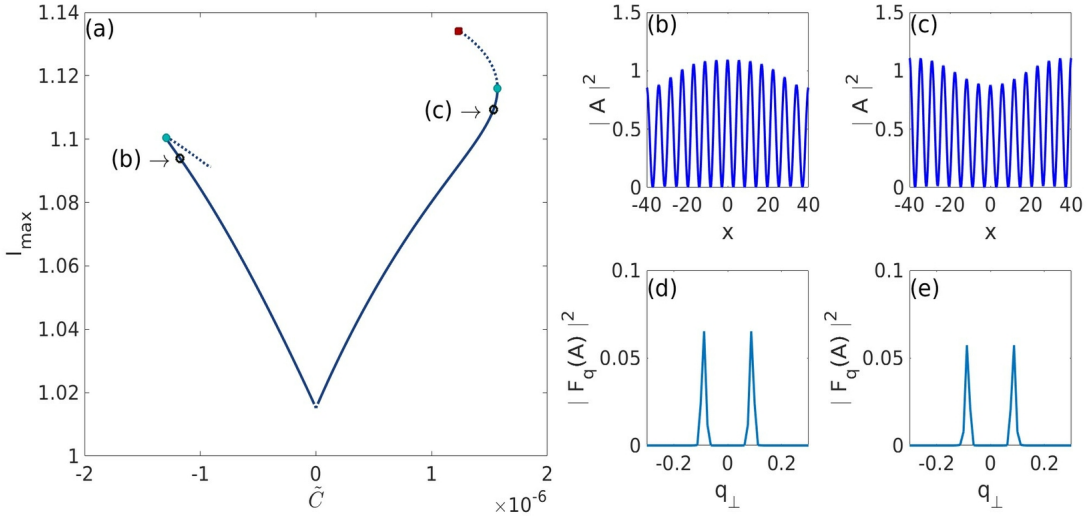

Figure 5.3: Continuation of a periodic solution as a function of $\tilde{C}$. Panel (a) show the bifurcation branches in the maximum intensity of the solution I_{max}. Fold points (cyan circle) separates the stable (solid blue) and unstable (dashed blue) region of the branches. Black open circles marks the solutions whose intensity profile is given in panels (b)-(c). The profile shown in (b) corresponds to a negative potential curvature parameter $\tilde{C} = -1.174 \times 10^{-6}$ and frequency shift $\omega = 0.2071$, while the profile in (c) is for $\tilde{C} = 1.534 \times 10^{-6}$ and $\omega = 0.2057$. The power spectrum of the solutions in (b-c) are shown in panels (d-c) respectively. Parameters : $\alpha_1 = 1.5$, $\alpha_2 = 0.5$, $J_1/J_{th} = 0.6252$, $J_2 = -0.06$, $s = 15$, $h = 1.98$, $\eta = 0.95$, $d = 0.0001$, $\tilde{B} = 0.7873$, $S = 1.0$.

The branches become unstable for magnitudes $|\tilde{C}| \gtrsim 10^{-6}$ through saddle-node bifurcation points (cyan circles). The intensity profiles of two stable periodic solutions are shown in Figs. 5.3(b-c) which illustrates the modulation of the amplitude of the solution due to the presence of corresponding negative or positive potential on the system. The panels in Fig. 5.3(d-e) shows the power spectrum of the solutions in Fig. 5.3(b-c) respectively. It can be noticed from the power spectrum that for the small magnitude values of the parameter $\tilde{C}$, the power peaks show negligible shift in spectral frequencies.

5.2.2 Turing Instability

As discussed in the previous section, the Linear Stability Analysis (LSA) of the system indicates the possibility of the emergence of modulated transversal patterns in a uniform steady state solution by tuning the state parameters such that Turing instability is induced. A uniform continuous wave solution of intensity $I = 1.0$ is considered for time evolution using direct numerical analysis as described in Section 2.3.5 with the system parameters chosen such that the resonant condition defined in Eq. (5.16) is satisfied for the transverse length $L_\perp$ and the condition given in Eq. 5.15 is satisfied for the parameters $\tilde{B}$ and S at an appropriate Turing wavevector q_T. It was seen that the solution leads to the emergence of periodic pattern over time as shown in Fig. 5.4(a). The intensity profile of the emergent periodic patterns can be seen in Fig. 5.4(b), while its corresponding power spectrum is shown in Fig. 5.4(c). Conversely, the periodic solution defined with wavevector equal to the Turing wavevector was found to be stable against time evolution.

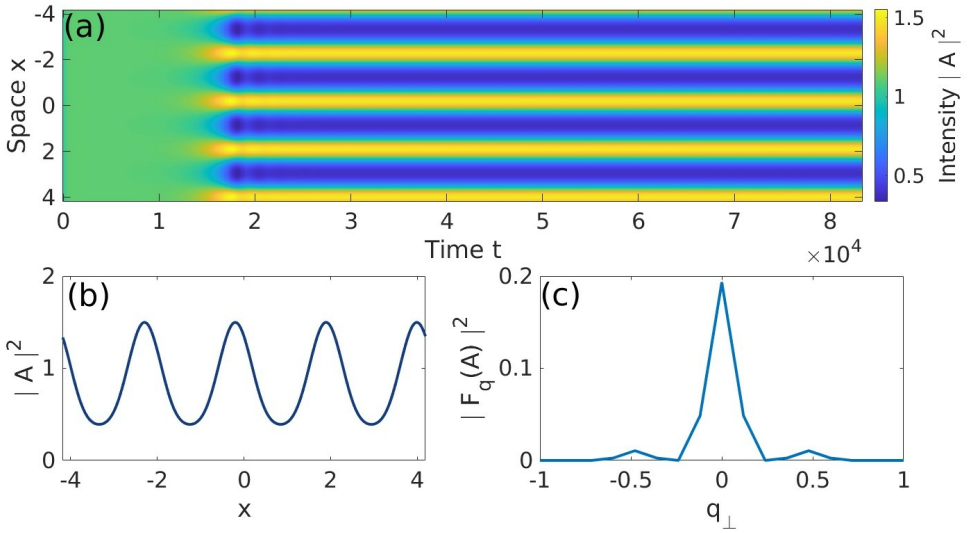

Figure 5.4: Time simulation of a uniform continuous solution in one dimension of Eq. (5.1) at Turing instability resulting in the emergence of transversal periodic patterns. Panel (b) shows the intensity profile of the final periodic solution and (c) shows its corresponding power spectrum. Parameters : $\alpha_1 = 1.5$, $\alpha_2 = 0.5$, $J_1/J_{th} = 0.8043$, $J_2 = -0.12$, $s = 15$, $h = 1.98$, $\eta = 0.833$, $d = 0.003$, $\tilde{B} = 0.99988$, $\tilde{C} = 0.0$, $S = 0.11$, $L_x = 8.3776$.

For arc-length continuation, the low frequency cut-off chosen is $q_c = 0.75$, as shown in Fig. 5.1, which corresponds to a transverse length $L_\perp = 8.3776$ and the resonant condition in Eq. (5.16) is met for Turing wavevector $q_T = 3.0$ with $q_T/q_c = 4$. With periodic boundary conditions assumed in the system, the domain length correspondingly is seen to be equivalent to 4 wavelengths of the periodic solution.

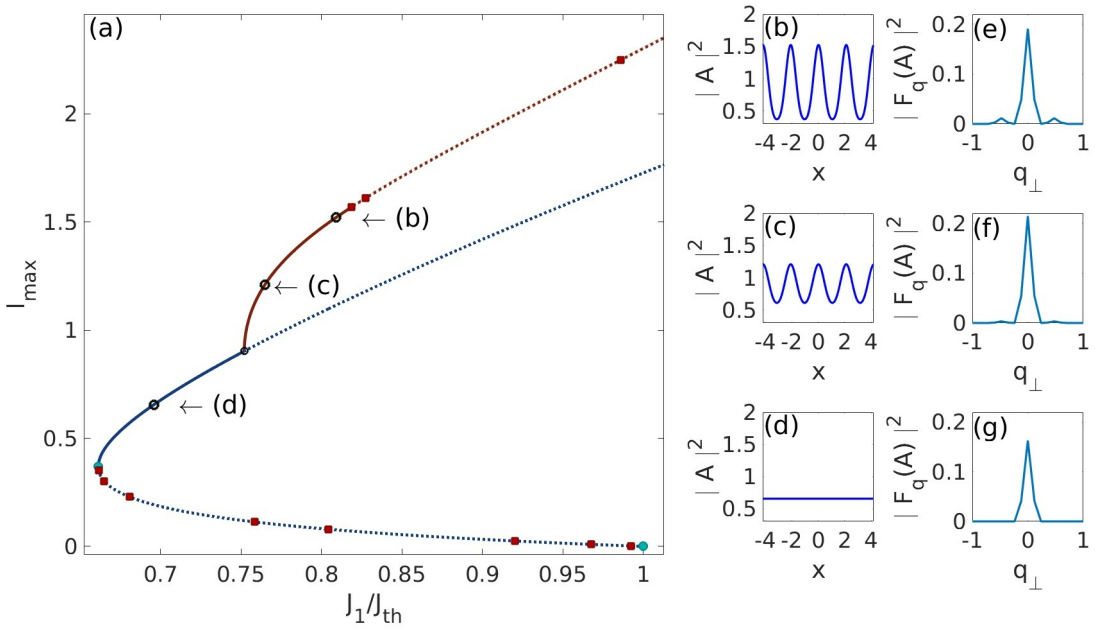

Figure 5.5: Continuation results of continuous wave (blue) and periodic (red) solutions of Eq. (5.1) as a function of J_1/J_{th}. Panel (a) show the bifurcation branches in the maximum intensity of the solutions I_{max}. Fold points (cyan circle) separates the stable (solid blue line) and unstable (dashed blue line) region of the continuous wave (CW) solution branch. A stable periodic solution bifurcates from the CW at the branching point(black open circle). Three sample solutions from the two branches are marked whose intensity profiles are given in panels (b)-(d). The profile shown in (b) corresponds to $J_1/J_{th} = 0.8091$ and frequency shift $\omega = 0.1733$, while the profile in (c) is for $J_1/J_{th} = 0.7647$ and $\omega = 0.1631$ and the profile in (d) is for a continuous wave solution for $J_1/J_{th} = 0.696$ and $\omega = 0.1625$. The power spectrum of the solutions in (b-d) are shown in panels (e-g) respectively. Parameters : $\alpha_1 = 1.5$, $\alpha_2 = 0.5$, $J_2 = -0.12$, $s = 15$, $h = 1.98$, $\eta = 0.833$, $d = 0.003$, $\tilde{B} = 0.99988$, $\tilde{C} = 0.0$, $S = 0.11$, $L_\perp = 8.3776$.

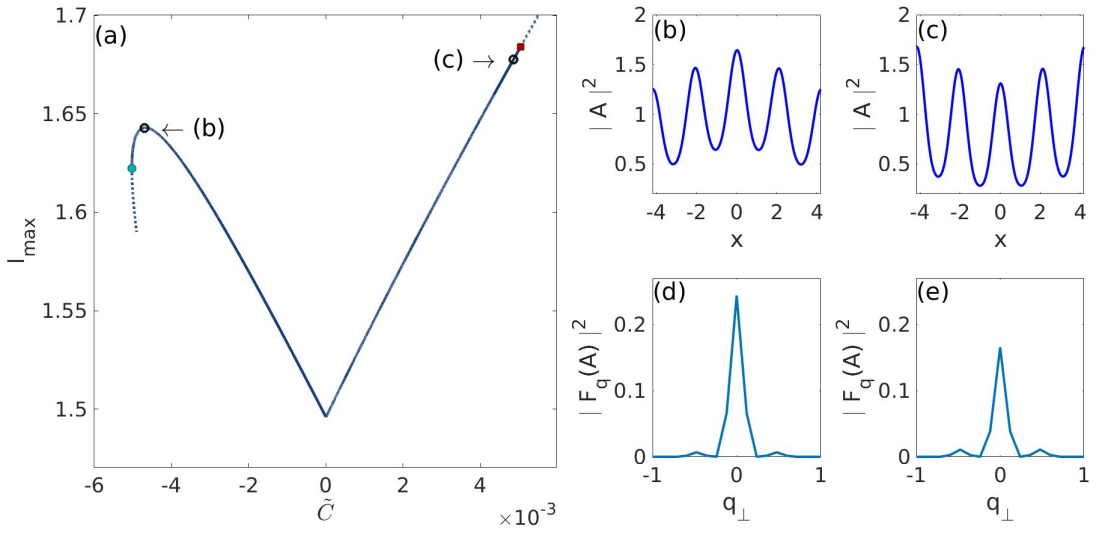

Figure 5.6: Continuation of a periodic solution of Eq. (5.1) as a function of $\tilde{C}$. Panel (a) show the bifurcation branches in the maximum intensity of the solution I_{max}. Fold point (cyan circle) and Andronov-Hopf bifurcation points (red square) separate the stable (solid blue line) and unstable (dashed blue line) region of the branches. Black open circles mark the solutions whose intensity profile is given in panels (b)-(c). The profile shown in (b) corresponds to a negative potential curvature parameter $\tilde{C} = -4.696 \times 10^{-3}$ and frequency shift $\omega = 0.1929$, while the profile in (c) is for $\tilde{C} = 4.859 \times 10^{-3}$ and $\omega = 0.144$. The power spectrum of the solutions in (b-c) are shown in panels (d-e) respectively. Parameters : $\alpha_1 = 1.5$, $\alpha_2 = 0.5$, $J_1/J_{th} = 0.8043$, $J_2 = -0.12$, $s = 15$, $h = 1.98$, $\eta = 0.833$, $d = 0.003$, $\tilde{B} = 0.99988$, $S = 0.11$, $L_\perp = 8.3776$.

In the Fig. 5.5, the continuation of the uniform solution as a function of parameter J_1 is shown. As can be observed in the bifurcation diagram in Fig. 5.5(a), the unstable branch of the uniform continuous wave solution (blue) bifurcates from the off state at threshold ($J_1 = J_{th}$) and becomes stable through a saddle-node bifurcation (cyan circle). Beyond the fold point, with increasing J_1 along the stable higher intensity branch of the continuous wave solution branch, a stable branch of a periodic wave solution (red) bifurcates via a branching point (black open circle) till it becomes unstable through an Andronov-Hopf bifurcation (red square).
The panels in Fig. 5.5(b-d) illustrates three intensity profiles for stable solutions of the system. In Fig. 5.5(d), the profile of the continuous wave solution is shown along with its power spectrum in Fig. 5.5(g). The emerging periodic pattern in the stable periodic wave solution branch is shown in Figs. 5.5(b-c). The intensity of the periodic pattern solution increases with increasing J_1 as expected. The corresponding power spectrum of the patterned solutions are shown in Fig. 5.5(e-f) respectively, which shows two power peaks emerging on either side of the central power peak at $q_\perp = 0$.
The condition defined in Eq. (5.15) was met for this continuation results with $\sqrt{\tilde{B}/S} = 3.015 \approx q_T$. The effective curvature parameter $\tilde{C}$ is zero as required by the assumption imposed on the system during the stability analysis.
However, the effects of applying a small potential to the system on the periodic pattern solution is also investigated via path continuation in the parameter $\tilde{C}$ and the results are presented in Fig. 5.6.
The bifurcation diagram shown in Fig. 5.6(a) shows the solutions are stable for small values of parameter $\tilde{C} \lesssim 5 \times 10^{-3}$. The intensity of the solution increases as the magnitude of the parameter $\tilde{C}$ increases. The branch becomes unstable through a saddle-node bifurcation (cyan circle) in the negative $\tilde{C}$ regime while in the positive $\tilde{C}$ region instability in the branch occurs via a Andronov-Hopf bifurcation point (red square). The intensity profiles of two illustrative solutions is shown in Fig. 5.6(b-c) which displays the modulation of the intensity profile due to the potential term depending on the sign of the parameter $\tilde{C}$. The corresponding power spectrum of the two intensity profiles in Fig. 5.6(b-c) are shown in Fig. 5.6(d-e) respectively.
Since the Turing wavevector q_T depends on the tuning parameters $\tilde{B}$ and S for the periodic pattern solutions, path continuation was performed on these two parameters as well whose results are presented in Figs. 5.7 and 5.8. In the Fig. 5.7(a), the continuation branch of the periodic solution as a function of $\tilde{B}$ shows that the solution remains stable for two narrow range of values of the parameter, the branch becoming unstable via multiple saddle-node bifurcation points as well as Andronov-Hopf bifurcation points. The intensity profiles of three stable solutions along the continuation branch are shown in Fig. 5.7(b-d) along with their power spectrum in Fig. 5.7(e-g) respectively.
An interesting formation of periodic transversal patterns emerges while tuning the parameter for the smaller values of $\tilde{B}$, that are stable solutions of the system as shown in Fig. 5.7(b). The intensity profile diverges from the plane periodic wave solution of Fig. 5.7(d) and the parameter set further tunes the condition given in Eq. (5.15), $\sqrt{\tilde{B}/S} = 3.00525 \approx q_T$. For the profile shown in Fig. 5.7(c), one observes the gradual dissipation of this periodic pattern as $\tilde{B}$ slightly decreases and the tuning condition becomes $\sqrt{\tilde{B}/S} = 3.00477$. Comparing the power spectrum of the solution profile in Fig. 5.7(b) in panel (e), to those of the other solutions, one observers the increase in peak power corresponding to the secondary spectral frequency peaks on either side of the central power peak.

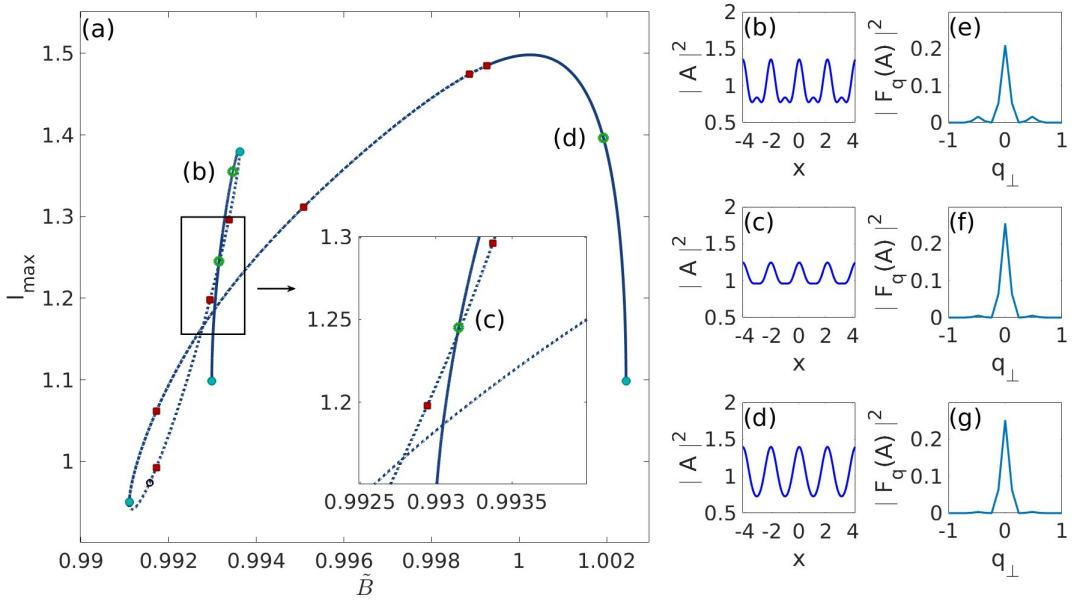

Figure 5.7: Continuation results of a periodic solution of Eq. (5.1) as a function of $\tilde{B}$. Panel (a) show the bifurcation branch in the maximum intensity of the solutions I_{max}. Fold points (cyan circle) and Andronov-Hopf bifurcation points (red squares) separates the stable (solid blue line) and unstable (dashed blue line) region of the solution branch. Three sample solutions are marked with green circles whose intensity profiles are given in panels (b)-(d). The profile shown in (b) corresponds to $\tilde{B} = 0.99347$ and frequency shift $\omega = 0.168$, the profile in (c) is for $\tilde{B} = 0.99315$ and $\omega = 0.1604$, and the profile in (d) is for $\tilde{B} = 1.0019$ and $\omega = 0.1617$. The power spectrum of the solutions in (b-d) are shown in panels (e-g) respectively. Parameters : $\alpha_1 = 1.5$, $\alpha_2 = 0.5$, $J_1/J_{th} = 0.8043$, $J_2 = -0.12$, $s = 15$, $h = 1.98$, $\eta = 0.833$, $d = 0.003$, $\tilde{C} = 0.0$, $S = 0.11$, $L_\perp = 8.3776$.

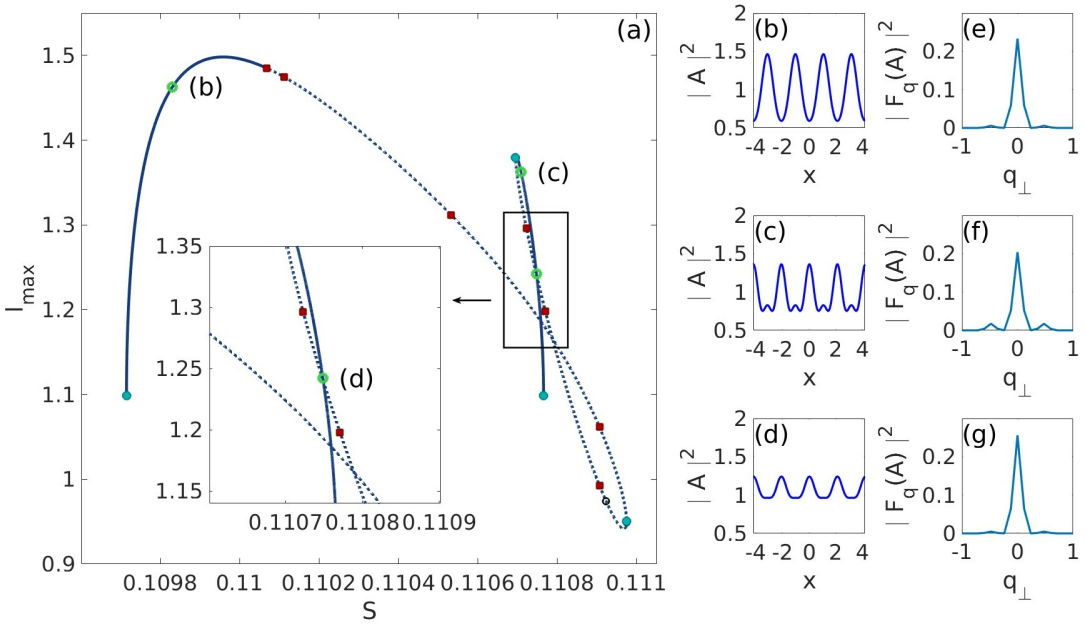

Figure 5.8: Continuation results of a periodic solution of Eq. (5.1) as a function of S. Panel (a) show the bifurcation branch, stable (solid blue) and unstable (dashed blue), in the maximum intensity of the solutions I_{max}. Fold points (cyan circle) and Andronov-Hopf bifurcation points (red squares) separates the stable and unstable region of the solution branch. Three sample solutions are marked with green circles whose intensity profiles are given in panels (b)-(d). The profile shown in (b) corresponds to $S = 0.10983$ and frequency shift $\omega = 0.1652$, the profile in (c) is for $S = 0.11071$ and $\omega = 0.169$, and the profile in (d) is for $S = 0.11075$ and $\omega = 0.1603$. The power spectrum of the solutions in (b-d) are shown in panels (e-g) respectively. Parameters : $\alpha_1 = 1.5$, $\alpha_2 = 0.5$, $J_1/J_{th} = 0.8043$, $J_2 = -0.12$, $s = 15$, $h = 1.98$, $\eta = 0.833$, $d = 0.003$, $\tilde{B} = 0.99988$ $\tilde{C} = 0.0$, $L_\perp = 8.3776$.

Similarly, with continuation of the periodic solution in the parameter S, as shown in Fig. 5.8(a), it is observed that there are two narrow stable regions on the continuation branch where the stable region corresponding to the higher value of parameter S results in the emergence of periodic patterns as the profile in Fig. 5.7(b). The solution profile in Fig. 5.8(c) corresponds to $\sqrt{\tilde{B}/S} = 3.00525 \approx q_T$ and its corresponding power spectrum in Fig. 5.8(f) is similar to the power spectrum of the solution in Fig. 5.7(e). As S increases along the continuation branch this specific patterned solution dissipates into the profile shown in Fig. 5.8(d) with tuning condition resulting to $\sqrt{\tilde{B}/S} = 3.00471$.
In contrast, the stable region of the continuation branch for lower value of S in Fig. 5.8(a) consists of stable periodic solutions of the form shown in Fig. 5.8(b) along with its power spectrum in Fig. 5.8(e).
The two emerging periodic pattern solutions obtained by tuning the parameters $\tilde{B}$ and S, shown in Figs. 5.7(b) and 5.8(c), are of interest and in the following, further continuation is performed in the parameters J_1 and $\tilde{C}$ on these solutions to confirm their stability with variation in those parameters.
The continuation results on the periodic pattern solution shown in Fig. 5.7(b) in the parameter J_1 is given in Fig. 5.9. As can be observed from the bifurcation diagram in Fig. 5.9(a), the solution becomes stable via a saddle-node bifurcation around $J_1/J_{th} \approx 0.78$ and continues to remain stable well beyond the threshold gain bias J_{th}. With increase in the parameter J_1, the maximum intensity I_{max} increases almost monotonically for a large range of J_1.

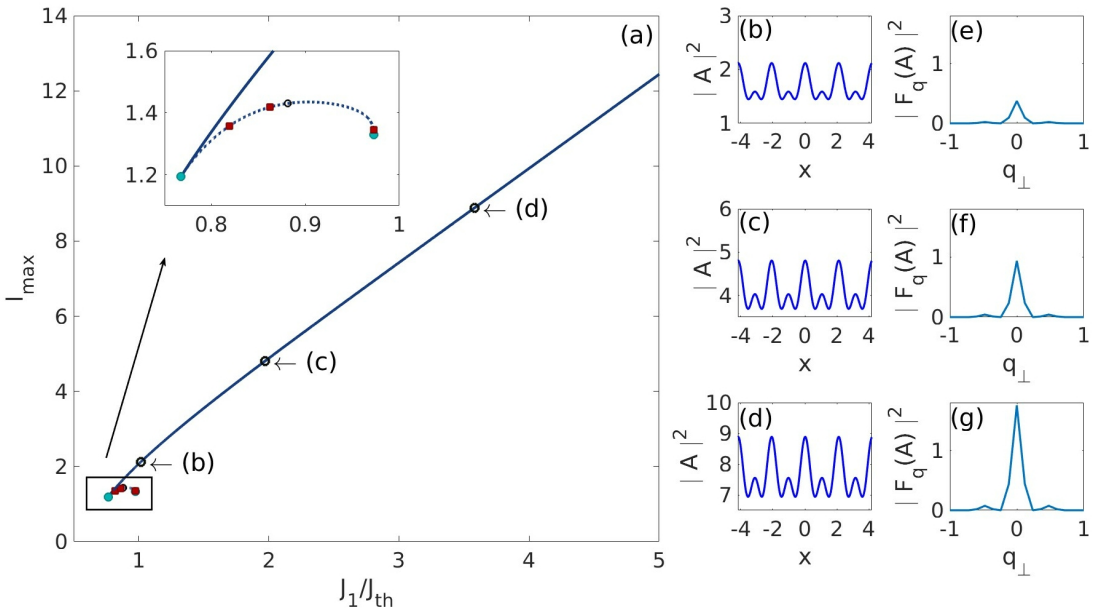

Figure 5.9: Continuation of the periodic pattern solution from tuning the parameter $\tilde{B}$ shown in Fig. 5.7 as a function of J_1/J_{th}. Panel (a) show the bifurcation branch, stable (solid blue) and unstable (dashed blue), in the maximum intensity of the solution I_{max}. Fold points (cyan circle), and several Andronov-Hopf bifurcation points (red squares) are present along the continuation branch. The intensity profiles of the three stable solutions along the continuation branch marked in black open circles are shown in panels (b-d). The profile in (b) corresponds to $J_1/J_{th} = 1.0153$ and frequency shift $\omega = 0.1627$, the solution profile in (c) is for $J_1/J_th = 1.9692$ and $\omega = 0.1581$, and the profile in (d) is for $J_1/J_th = 3.58$ and $\omega = 0.1569$. The corresponding power spectrum are shown in panels (e-g). Parameters : $\alpha_1 = 1.5$, $\alpha_2 = 0.5$, $J_2 = -0.012$, $s = 15$, $h = 1.98$, $\eta = 0.833$, $d = 0.003$, $\tilde{B} = 0.99347$, $\tilde{C} = 0.0$, $S = 0.11$, $L_\perp = 8.3776$.

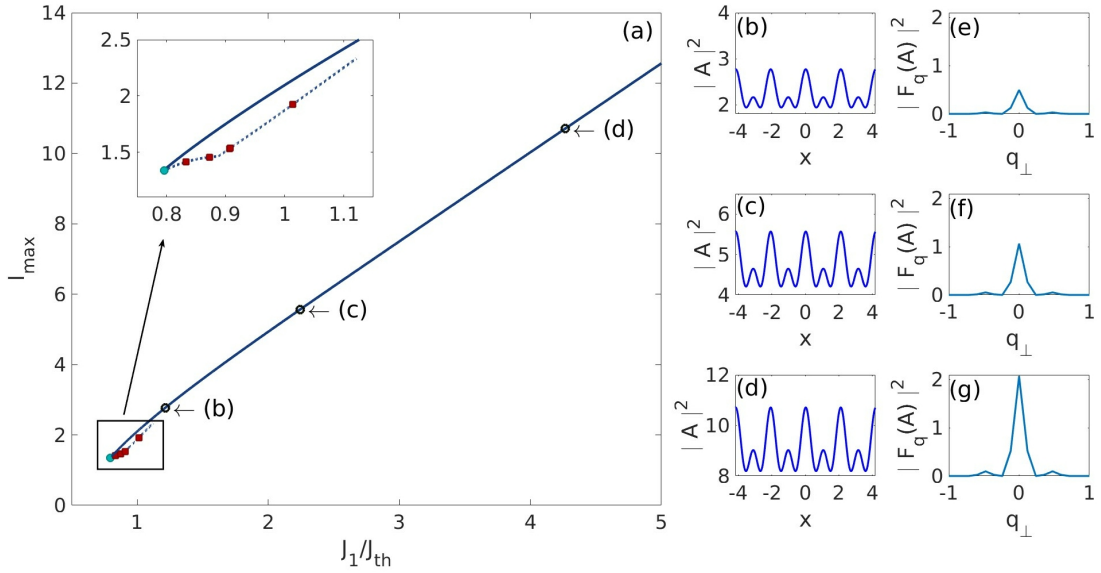

Figure 5.10: Continuation of the periodic pattern solution from tuning the parameter S shown in Fig. 5.8 as a function of J_1/J_{th}. Panel (a) show the bifurcation branch, stable (solid blue) and unstable (dashed blue), in the maximum intensity of the solution I_{max}. Fold points (cyan circle), and several Andronov-Hopf bifurcation points (red squares) are present along the continuation branch. The intensity profiles of the three stable solutions along the continuation branch marked in black open circles are shown in panels (b-d). The profile in (b) corresponds to $J_1/J_{th} = 1.2138$ and frequency shift $\omega = 0.1617$, the solution profile in (c) is for $J_1/J_th = 2,2427$ and $\omega = 0.1585$, and the profile in (d) is for $J_1/J_th = 4.2665$ and $\omega = 0.1574$. The corresponding power spectrum are shown in panels (e-g). Parameters : $\alpha_1 = 1.5$, $\alpha_2 = 0.5$, $J_2 = -0.012$, $s = 15$, $h = 1.98$, $\eta = 0.833$, $d = 0.003$, $\tilde{B} = 0.99988$, $\tilde{C} = 0.0$, $S = 0.11071$, $L_\perp = 8.3776$.

The intensity profiles of three stable solutions along the continuation branch are shown in Figs. 5.9(b-d) for increasing values of J_1 respectively. The profile of the periodic pattern solution is maintained during continuation without any dissipation in the modulated intensity profile, while the intensity of the periodic solution continues to increase. Similar trend is also observed in the respective power spectrum of the solution in Fig. 5.9(e-g) where the peak power increases with increase in J_1.

The continuation results on the periodic pattern solution shown in Fig. 5.8(c) in the parameter J_1 is given in Fig. 5.10. The bifurcation in Fig. 5.10(a) shows that through a saddle-node bifurcation (cyan circle) the solution becomes stable at around $J_1/J_{th} \approx 0.8$ and remains stable for a large range of values of J_1 beyond the threshold gain bias value $J_th = 0.22$. Similar to the results obtained in Fig. 5.9, the intensity of the solution increases monotonically with the increase in gain bias J_1.

Three stable solutions along the continuation branch marked in Fig. 5.10(a) have their intensity profiles given in Figs. 5.10(b-d) which shows that for periodic pattern solutions for the other set of tuning parameter values also maintain the modulation in the intensity of the solution with increasing values of J_1. The corresponding power spectrum shown in Figs. 5.10(e-g) confirm these findings.

The continuation results on the periodic pattern solution shown in Fig. 5.7(b) in the parameter $\tilde{C}$ is given in Fig. 5.11. From the continuation branch in Fig. 5.11, it can be observed that the solution remains stable for small magnitudes of the effective curvature parameter $\tilde{C}$, i.e., small effective potential on the domain of the system. For negative $\tilde{C}$, the solution remains stable for slightly lower magnitude than for positive $\tilde{C}$.

The intensity profiles of two stable solutions are shown in Fig. 5.11(b-c) which have mod-

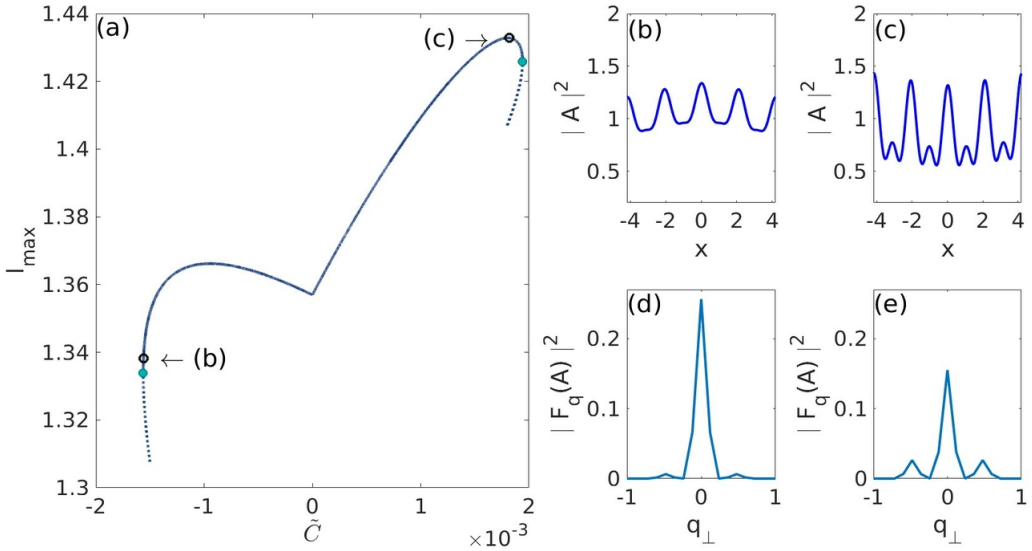

Figure 5.11: Continuation of the periodic pattern solution from tuning the parameter $\tilde{B}$ shown in Fig. 5.7 as a function of $\tilde{C}$. Panel (a) show the bifurcation branches, stable (solid blue) and unstable (dashed blue), in the maximum intensity of the solution I_{max}.The continuation branch becomes unstable via fold points (cyan circles). Black open circles mark the solutions whose intensity profile is given in panels (b)-(c). The profile shown in (b) corresponds to a negative potential curvature parameter $\tilde{C} = -1.5598 \times 10^{-3}$ and frequency shift $\omega = 0.1704$, while the profile in (c) is for $\tilde{C} = 1.821 \times 10^{-3}$ and $\omega = 0.1664$. The power spectrum of the solutions in (b-c) are shown in panels (d-e) respectively. Parameters : $\alpha_1 = 1.5$, $\alpha_2 = 0.5$, $J_1/J_{th} = 0.8043$, $J_2 = -0.12$, $s = 15$, $h = 1.98$, $\eta = 0.833$, $d = 0.003$, $\tilde{B} = 0.99347$, $S = 0.11$, $L_\perp = 8.3776$.

ulated amplitudes due to the presence of the potential term in the system parameters according to the sign of $\tilde{C}$ as observed for other periodic solutions. The profile corresponding to positive $\tilde{C}$ in Fig. 5.11(c) shows that the solution maintains the periodic patterns despite the effects of non-zero effective curvature parameter. The corresponding power spectrum in Fig. 5.11(e) is similar to the initial solution given in Fig. 5.7(b) used for continuation.

However, this changes in the continuation branch in the negative $\tilde{C}$ region where the intensity profile, shown in Fig. 5.11(b), illustrates that the periodic patterns of the solution slowly dissipates with increasing $\mid \tilde{C} \mid$, similarly to the solution shown in Fig. 5.7(c). The power spectrum of this solution is shown in Fig. 5.11(d) which shows relatively higher central peak power than the power spectrum for the solution with positive $\tilde{C}$ given in Fig. 5.11(e) despite the intensity profile indicating decrease in intensity.

The continuation results on the periodic pattern solution shown in Fig. 5.8(c) in the parameter $\tilde{C}$ is given in Fig. 5.12. For the continuation branch in Fig. 5.12(a), stable solutions exist for both positive and negative values of $\tilde{C}$, however the branch remain becomes unstable via saddle-node bifurcations for much smaller magnitudes of $\tilde{C}$ in the positive potential regime compared to negative potential.

Intensity profiles of two stable solutions along the branch are given in Fig. 5.12(b-c) with modulated amplitudes according to the sign of the curvature potential parameter $\tilde{C}$. As with the continuation results shown in Fig. 5.11, the stable solution corresponding to positive $\tilde{C}$ maintains the periodic pattern intensity profile of the solution and the power spectrum of this solution in Fig. 5.12(e) shows secondary power peaks on either side of the central peak.

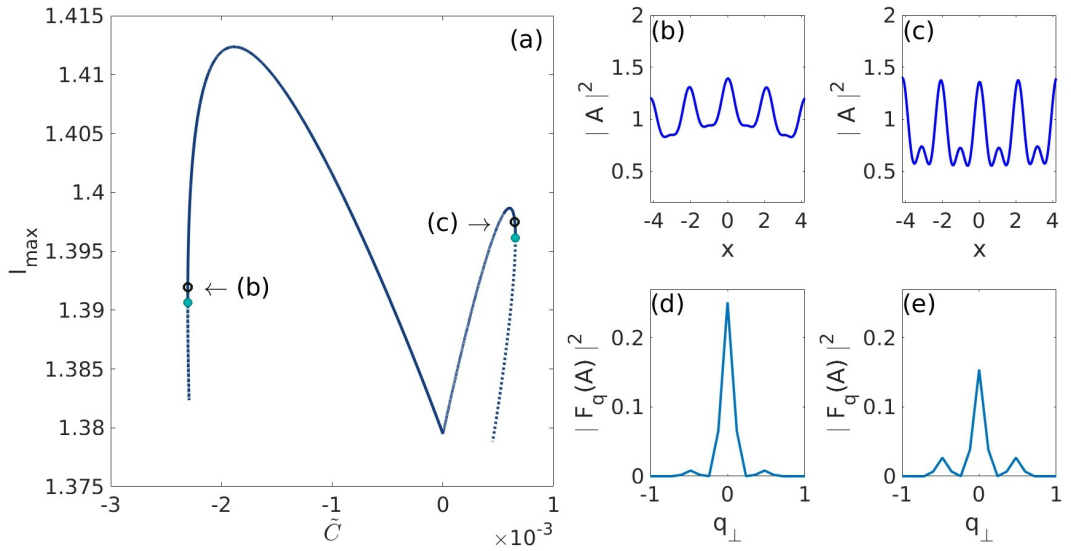

Figure 5.12: Continuation of the periodic pattern solution from tuning the parameter S shown in Fig. 5.8 as a function of $\tilde{C}$. Panel (a) show the bifurcation branches, stable (solid blue) and unstable (dashed blue), in the maximum intensity of the solution I_{max}.The continuation branch becomes unstable via fold points (cyan circles). Black open circles mark the solutions whose intensity profile is given in panels (b)-(c). The profile shown in (b) corresponds to a negative potential curvature parameter $\tilde{C} = -2.304 \times 10^{-3}$ and frequency shift $\omega = 0.1759$, while the profile in (c) is for $\tilde{C} = 0.649 \times 10^{-3}$ and $\omega = 0.1745$. The power spectrum of the solutions in (b-c) are shown in panels (d-e) respectively. Parameters : $\alpha_1 = 1.5$, $\alpha_2 = 0.5$, $J_1/J_{th} = 0.8043$, $J_2 = -0.12$, $s = 15$, $h = 1.98$, $\eta = 0.833$, $d = 0.003$, $\tilde{B} = 0.99988$, $S = 0.11071$, $L_\perp = 8.3776$.

The intensity profile in Fig. 5.12(b) shows the solution for negative $\tilde{C}$. This solution illustrates that with increasing magnitude of $\mid \tilde{C} \mid$, the periodic pattern of the solution slowly dissipates, similar to the solution shown in Fig. 5.8(d). The corresponding power spectrum of this solution is given in Fig. 5.12(d) also has higher central power peak, despite the decrease in intensity, compared to the solution for positive $\tilde{C}$.
With these continuation results the findings of the stability analysis of the system equation in Eq. (5.1) for periodic and uniform steady state solutions are confirmed. The emergence of modulated periodic patterns due to Turing instability as well as periodic pattern formation in the solutions by tuning the system parameters was observed. The stability of these solutions under the effects of the potential term are also detailed.

6 Two-Dimensional Pattern Formation

6.1 Two-Dimensional Turing Instability

As discussed previously, in Section 5.1, the dispersion relation of the eigenvalues of the coefficient matrix of the 1D MIXSEL model Equation (2.22) indicate a narrow band of Turing instability for high frequencies that can lead to emergence of spatially periodic solutions. For the two-dimensional system of the MIXSEL model Equation (2.17) with wavefront curvature parameter $\tilde{C} = 0$, a similar linear stability analysis shows that instead of a fixed Turing wavevector q_T, only the magnitude of the unstable wave-vector $\mid q_T \mid$ is fixed. This leads to a various unstable wave-vectors in the two-dimensional plane $q_\perp = (q_x, q_y)$ that satisfy the condition for Turing instability.
Depending on the system parameters used as well as the finite transverse dimension sizes L_x and L_y, various patterns modulated two-dimensional patterns can emerge from the numerical simulation of uniform solutions. Various simulation results at different system parameters are shown below considering the Turing wave-vector $q_T \approx 3$.
The resonant condition given in Eq. (5.16) is satisfied as $q_T/q_c = 4$ for the cut-off frequency $q_c = (2\pi)/L_x$ such that the transverse dimension size in the $x-$direction is

$$L_x = 4\frac{2\pi}{q_T}. \tag{6.1}$$

With this set of parameters, two different types of domain sizes in the $y-$direction is considered. A square domain is when $L_x = L_y$ for the sizes of the transverse dimensions, while hexagonal domain is when $L_y = (\sqrt{3}/2)L_x$.
For direct numerical simulation of a uniform solution with intensity $I = 1.0$, the method described in Section 2.2 is used for two transverse dimensions $r_\perp = (x, y)$ to investigate the dynamics at the spectral frequencies that induce Turing instability. Tuning the parameters $\tilde{B}$ and S gives rise to different forms of two-dimensional patterns in the solutions as per Eq. (5.15).
Simulation results of two-dimensional uniform solutions within a square domain are given in Figs. 6.1 and 6.2 corresponding to two stripped patterned solutions, as well as Fig. 6.3 which shows square patterns in the solution. In Fig. 6.1, the pattern that emerges for the particular set of tuning parameters for a square domain are vertical stripes in the two-dimensional intensity profile in Fig. 6.1(b). The corresponding power spectrum, in the log scale, is given in Fig. 6.1(c) which shows the expected distribution of spectral frequencies in the Fourier domain for such a patterned solution.

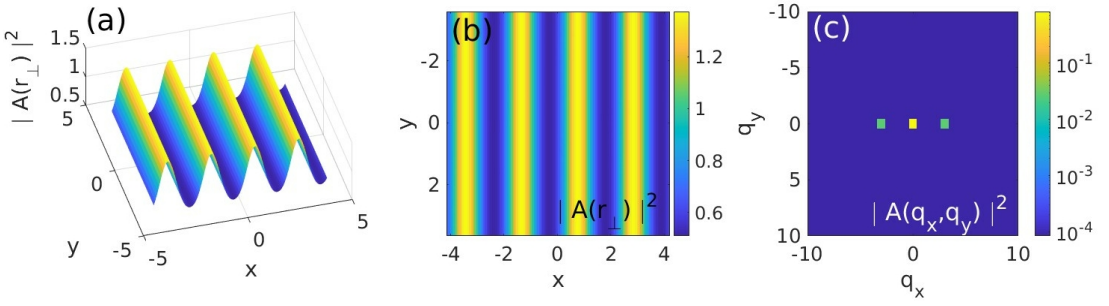

Figure 6.1: Stable solution of Eq. (2.17) in two dimensions by direct numerical simulation. Panel (a) and (b) shows the intensity profile of the solution and the power spectrum (log scale) is shown in panel (c). The profile shows the emergence of stripes in the square domain. Parameters: $\alpha_1 = 1.5$, $\alpha_2 = 0.5$, $J_1/J_{th} = 0.777$, $J_2 = -0.12$, $s = 15$, $h = 1.98$, $\eta = 0.833$, $d = 0.003$, $\tilde{B} = 0.99988$, $S = 0.11$, $L_x = L_y = 8.3776$.

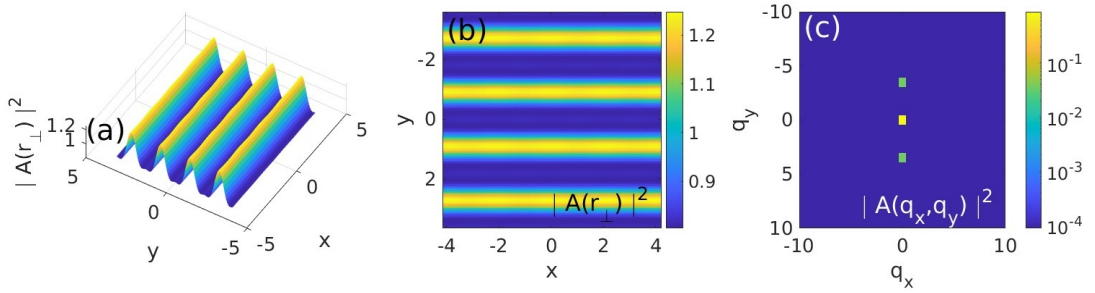

Figure 6.2: Stable solution of Eq. (2.17) in two dimensions by direct numerical simulation. Panel (a) and (b) shows the intensity profile of the solution and the power spectrum (log scale) is shown in panel (c). The profile shows the emergence of stripes in the square domain. Parameters: $\alpha_1 = 1.5$, $\alpha_2 = 0.5$, $J_1/J_{th} = 0.777$, $J_2 = -0.12$, $s = 15$, $h = 1.98$, $\eta = 0.833$, $d = 0.003$, $\tilde{B} = 0.99988$, $S = 0.11071$, $L_x = L_y = 8.3776$.

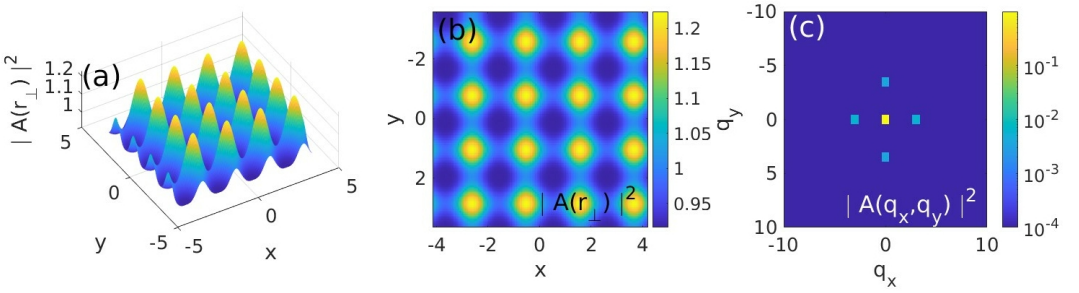

Figure 6.3: Stable solution of Eq. (2.17) in two dimensions by direct numerical simulation. Panel (a) and (b) shows the intensity profile of the solution and the power spectrum (log scale) is shown in panel (c). The profile shows the emergence of square patterns in the square domain. Parameters : $\alpha_1 = 1.5$, $\alpha_2 = 0.5$, $J_1/J_{th} = 0.777$, $J_2 = -0.12$, $s = 15$, $h = 1.98$, $\eta = 0.833$, $d = 0.003$, $\tilde{B} = 0.99347$, $S = 0.11$, $L_x = L_y = 8.3776$.

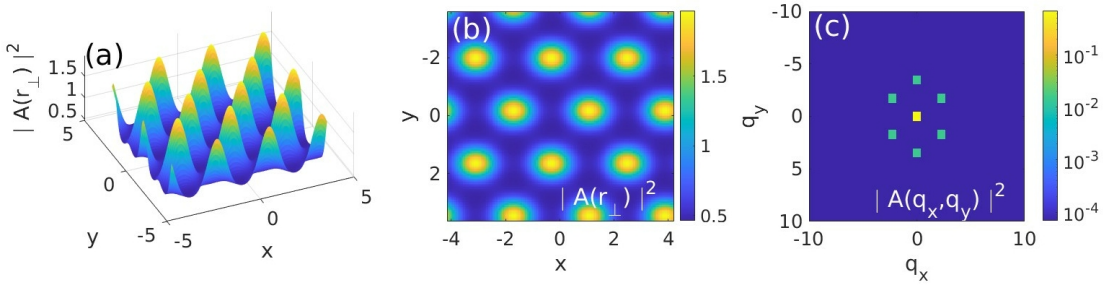

Figure 6.4: Stable solution of Eq. (2.17) in two dimensions by direct numerical simulation. Panel (a) and (b) shows the intensity profile of the solution and the power spectrum (log scale) is shown in panel (c). The profile shows the emergence of hexagons in the hexagonal domain. Parameters : $\alpha_1 = 1.5$, $\alpha_2 = 0.5$, $J_1/J_{th} = 0.777$, $J_2 = -0.12$, $s = 15$, $h = 1.98$, $\eta = 0.833$, $d = 0.003$, $\tilde{B} = 0.99988$, $S = 0.11$, $L_x = 8.3776$, $L_y = 7.2552$.

Similarly, another solution is shown in Fig. 6.2 for the system in the square spatial domain where the patterns that emerge from the uniform solution are horizontal stripes, see Fig. 6.2(a). The power spectrum in the Fourier domain, Fig. 6.2(c) is also typical spectrum expected from the horizontal stripped patterns. This solution is obtained by slight tuning in the aberration parameter S from the parameter state defined for the solution given in Fig. 6.2.

However, the results shown in Fig. 6.3 correspond to the emergence of square patterns within the spatial domain as shown in Fig. 6.3(b) and is also obtained by slightly tuning the parameter $\tilde{B}$. The power spectrum of the square pattern solution, shown in Fig. 6.3(c) is characteristically different from those of the stripes with additional spectral frequency peaks.
In the case for the system defined with a hexagonal domain, the primary patterns that emerge from simulation of uniform solutions around q_T are hexagons. Some examples of such hexagonal solutions are shown in Figs. 6.4, 6.5 and 6.6 obtained from direct numerical simulation in two dimensions.

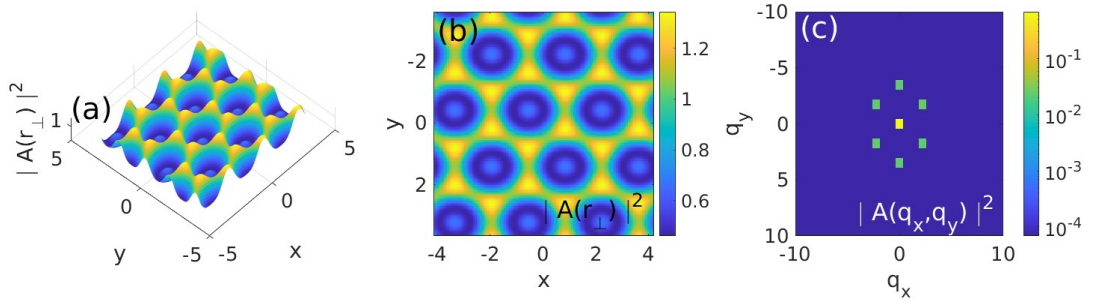

Figure 6.5: Stable solution of Eq. (2.17) in two dimensions by direct numerical simulation. Panel (a) and (b) shows the intensity profile of the solution and the power spectrum (log scale) is shown in panel (c). The profile shows the emergence of inverse hexagons in the hexagonal domain. Parameters : $\alpha_1 = 1.5$, $\alpha_2 = 0.5$, $J_1/J_{th} = 0.777$, $J_2 = -0.12$, $s = 15$, $h = 1.98$, $\eta = 0.833$, $d = 0.003$, $\tilde{B} = 0.99347$, $S = 0.11$, $L_x = 8.3776$, $L_y = 7.2552$.

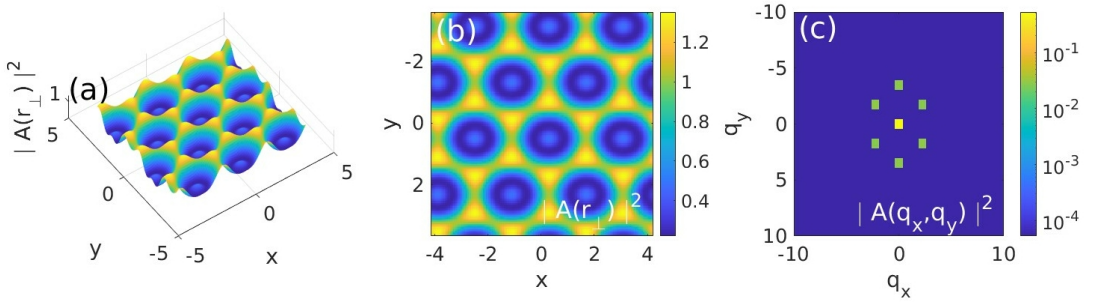

Figure 6.6: Stable solution of Eq. (2.17) in two dimensions by direct numerical simulation. Panel (a) and (b) shows the intensity profile of the solution and the power spectrum (log scale) is shown in panel (c). The profile shows the emergence of inverse hexagons in the hexagonal domain. Parameters : $\alpha_1 = 1.5$, $\alpha_2 = 0.5$, $J_1/J_{th} = 0.777$, $J_2 = -0.12$, $s = 15$, $h = 1.98$, $\eta = 0.833$, $d = 0.003$, $\tilde{B} = 0.99988$, $S = 0.11071$, $L_x = 8.3776$, $L_y = 7.2552$.

In Fig. 6.4, the emergent patterns are hexagons whose intensity profile is shown in Fig. 6.4(b). The corresponding power spectrum in Fig. 6.4(c) is the typical Fourier domain spectral peaks for hexagonal solutions in two dimensions.
Two other solutions from direct numerical simulation are obtained by tuning the parameters $\tilde{B}$ and S that resulted into hexagonal patterns, given in Figs. 6.5 and 6.6. However, the intensity profile of these solutions are inverted as compared to the solution in Fig. 6.4(b), while the power spectrum of all three solutions have similar spectral frequency peaks in the Fourier space.
The hexagonal pattern in the spatial intensity profile in Fig. 6.5(a) and 6.6(a) is clearly observed. The difference between the profiles in Fig. 6.5(b) and 6.6(c) is simply the relative orientation in the hexagonal patterns in the defined transverse spatial domain.

These simulation results of modulated patterns emerging from steady solutions of uniform intensity confirms the results of the linear stability analysis performed on the two-dimensional system in Section 5.1. While the results obtained from linear stability analysis predict instability and wavelength of the solution, the pattern selection is dependent on the nonlinearity. The nonlinearity due to light-matter interaction in the MIXSEL model Eq, (2.17) favors the formation of hexagonal patterns in the solution.

7 Conclusion

In this thesis, the dynamics of transversal patterns that can emerge in optical micro-cavities due to the interaction of two different types of nonlinear effects along a fourth-order partial derivative were studied and presented. The first part deals with the Quartic Dispersion Nonlinear Schrödinger Equation (QDNLSE) (2.5) which has multiple families of pulse solutions called Generalized Dispersion Kerr Solitons (GDKS) [12]. In the second part, the dynamics of the solutions of a MIXSEL model Equation (2.17) that describes the effects of light matter interaction in an gain-absorber integrated system along with effects of micro-cavities with small chromatic dispersion coupled with an external feedback.

The Split-Step Method for direct numerical simulation using spectral techniques for the two nonlinear PDEs were described in Chapter 2, along with two different schemes, Semi-Implicit Euler and Second Order Split-Step, for integrating the two differential equations. This method of direct analysis was used for select solutions to analyze stability of the solutions and their dynamics in later chapters.

Furthermore, the principles of arc-length Path Continuation were discussed in Chapter 2 which is another method of analyzing steady solutions to differential equations and their stability. The MATLAB [24] package pde2path [25] that was used to perform path continuation on the two nonlinear system equations was described and the implementation for path continuation on the two PDEs was given in detail. The method for implementation of nonlinear PDEs with higher order partial derivatives for continuation in pde2path is a generalized technique and can be used for other nonlinear PDEs as well.

In Chapter 3, the results of continuation of the Generalized Dispersion Kerr Solitons were presented. First, a general analysis was performed on the QDNLSE such that the only real field solutions were allowed. This led to the eigenvalue equation (3.3) and the critical value of the phase parameter μ_0 that divided the parameter plane of the system into sections corresponding to the nature of the oscillating tails of the solution. Arc-length Path continuation performed on the system equation (3.2) confirmed the existence of these families of soliton solutions called GDKS.

It was confirmed that for negative values of the second order dispersion parameter and phase parameter below the critical value, the solutions are soliton-like with exponentially decaying tails. However, when the phase parameter goes above the critical value, patterns in the solution start to emerge that have oscillating tails, becoming more oscillatory as the second order dispersion parameter becomes more positive. Whereas, no localized solutions were found, either by direct simulation or through continuation for positive second order dispersion parameter values with below critical values of the phase parameter. A special family of GDKS solutions called Pure Quartic Solitons [7], that correspond to zero second order dispersion, was also presented.

Next, the system was extended into the complex regime to analyze the stability of these solutions to the QDNLSE (2.5) by Arclength Path Continuation. The resulting solutions presented in Chapter 3, were for complex field profiles. Stable steady state solutions were found in confirmation of the results for the real field implementation. Oscillatory transverse patterns were observed in the solutions for positive second order dispersion above the critical value of the phase parameter. Spectrally asymmetric solutions were also found that were stable.

The eigenvalues of these complex field steady state solutions were analyzed and unstable complex envelope solutions were found. The stability of the solutions as obtained from the eigenvalues of the Jacobian during continuation was confirmed later via direct

numerical simulation as well. Two unstable solutions had been discussed, one that was a traveling wave solution and the other being a dissipative solution that had modulated intensity due to radiative losses. Thus, in contrast to the Nonlinear Schrödinger Equation (2.1), it was found that adding a quartic dispersion term to the system led to the steady state solutions with oscillating tails for certain parameter regimes.

In Chapter 4, the 1D MIXSEL model Eq. (2.22) was analytically solved, assuming weak nonlinearity and losses, which led to a class of solutions called Hermite-Gauss modes for the ODE system (4.2) in a stable cavity with no aberrations. In an unstable cavity with aberrations, tilted Hermite-Gauss modes are the analytical solutions that shifts the mode-frequencies. The wavevectors of these tilted Hermite-Gauss modes are determined by the values of the effective diffraction and the aberration parameters, as well as determine the parameter regime where the cavity becomes stable. Direct numerical analysis on these modes confirmed the analytical results as stable steady state solutions of the system. The tilted Hermite-Gauss modes were classified into two sub-classes and continuation was performed with each of the fundamental modes as well as of higher order modes.

The continuation results with the gain bias current as the control parameter on the three modes yielded similar trends in the bifurcation diagrams. The solution branch bifurcates from the stable off-state solution at threshold via an Andronov-Hopf bifurcation and becomes unstable as the gain bias current decreases. It again becomes stable via a saddle-node bifurcation as the branch turns and gain bias current increases. This leads to bi-stability of the solution since for every value of the gain bias current, there exists one low intensity unstable solution and a high intensity stable solution. From the relation for the gain current in Eq. (2.19), bi-stable solutions was expected along with the stable off-state.

For continuation on the aberration parameter as the control for these modes, it was found that the oscillatory tails of the mode always become more oscillatory as aberration approached zero, along with higher spectral frequencies in the power spectrum of the mode. This result is consistent with the analytical expression for the wave-vector of these modes given in Eq. (4.7) which indicated that for smaller aberration parameter values the transverse spectral frequencies increase in magnitude and the modes become highly oscillatory.

In contrast, relation (4.7) indicates that for smaller values of the effective diffraction parameter, the spectral frequencies decrease in magnitude and, hence, the mode loses its highly oscillatory transverse patterns. This finding was also confirmed via continuation with the effective diffraction parameter as the control parameter for the three modes. The effects of the potential term on the spatial domain was also analyzed from the bifurcation diagrams with the wavefront curvature as the control parameter. The three tilted Hermite-Gauss modes were found we be stable for relatively small values of the wavefront curvature parameter, forming more oscillatory transversal patterns in the solution modes as the parameter values decreased. Other higher modes were found to be unstable by direct numerical simulation.

In Chapter 5, linear stability analysis of the MIXSEL model Eq. (2.17) with the wavefront curvature parameter being zero, i.e., no potential effect on the spatial domain, is presented. The eigenvalues obtained from the effective coefficient matrix of the linearized system indicated the presence of modulational instabilty for the long wavelength regime in the dispersion relation. However, for certain set of parameter values, the dispersion relation showed the presence of a narrow band of Turing instability in the system. The wavevector at which the Turing instability was present, called Turing wavevector, gave

rise to a resonant condition with the finite transverse domain length (5.16) as well as a tuning condition dependent on the effective diffraction and aberration parameter (5.15). This Turing instability that leads to the emergence of periodic patterns in a uniform continuous wave solution was confirmed by continuation with the gain bias as the control parameter at the defined parameter regime, where the bifurcation diagram shows the branching of a periodic solution branch from the uniform solution branch. The emergence of patterns in uniform solution was also confirmed with direct numerical simulation. Furthermore, with continuation in the tuning parameters, various periodic pattern solutions were also observed.

The effects of adding potential to the transverse spatial domain of the periodic pattern solution was also investigated by continuation with wavefront curvature parameter as control. As can be expected, the potential term modulated the solution depending on the sign of the wavefront curvature parameter. The results indicated that the periodic pattern solutions of the MIXSEL model were stable for small values of potential, both negative and positive. For positive potential to the system, the periodic pattern solutions maintained their modulated amplitudes while for negative potential the solutions slowly lost their periodic pattern profile.

In Chapter 6, the dispersion relation obtained from the linear stability analysis for the 1D MIXSEL model Eq. (5.1) was extended to the two-dimensional transverse spatial domain and the effects of Turing instability was investigated. From direct numerical simulation of uniform intensity two-dimensional transverse profiles, various steady periodic pattern solutions emerged dependent on the two-dimensional transverse domain sizes that were defined for the system.

Stripes and square patterns were found in a system with equal domain sizes of the two spatial dimensions, while for a hexagonal domain, hexagons were the preferred intensity pattern of the steady state solutions. Different patterns were found to emerge from direct numerical simulation by tuning the effective diffraction and aberration parameters, confirming the validity of the relation in Eq. (5.15).

Therefore, the different kinds of transversal patterns that might emerge in the solutions of differential equations describing two types of optical micro-cavities were presented and their dynamics were analyzed in this thesis.

8 References

[1] Katsunari Okamoto. *Fundamentals of Optical Waveguides*. Second Edition. Academic Press, 2006. DOI: https://doi.org/10.1016/B978-0-12-525096-2.X5000-4.

[2] Hermann Haus et al. "Optical resonators and filters". In: *Optical Microcavities. Series: Advanced Series in Applied Physics, ISBN: 978-981-238-775-2. WORLD SCIENTIFIC, Edited by Kerry Vahala, vol. 5, pp. 1-37* (2004). DOI: https://doi.org/10.1142/9789812565730_0001.

[3] "Optical Fibers". In: *Fiber-Optic Communication Systems*. John Wiley & Sons, Ltd, 2010. Chap. 2, pp. 24–78. ISBN: 9780470918524. DOI: https://doi.org/10.1002/9780470918524.ch2.

[4] Govind P. Agrawal. *Nonlinear Fiber Optics (Fifth Edition)*. Fifth Edition. Optics and Photonics. Boston: Academic Press, 2013. DOI: https://doi.org/10.1016/B978-0-12-397023-7.00005-X.

[5] T. I. Lakoba and G. P. Agrawal. "Effects of third-order dispersion on dispersion-managed solitons". In: *J. Opt. Soc. Am. B* 16.9 (1999), pp. 1332–1343. DOI: https://doi.org/10.1364/JOSAB.16.001332.

[6] Michel Piché, Jean-François Cormier, and Xiaonong Zhu. "Bright optical soliton in the presence of fourth-order dispersion". In: *Opt. Lett.* 21.12 (1996), pp. 845–847. DOI: https://doi.org/10.1364/OL.21.000845.

[7] Blanco-Redondo Andrea et al. "Pure-quartic solitons". In: *Nature Communications* 7 (1 2016), p. 10427. ISSN: 2041-1723. DOI: https://doi.org/10.1038/ncomms10427.

[8] Brandon G. Bale et al. "Effects of fourth-order fiber dispersion on ultrashort parabolic optical pulses in the normal dispersion regime". In: *Journal of the Optical Society America B* 28.9 (2011), pp. 2059–2065. DOI: https://doi.org/10.1364/JOSAB.28.002059.

[9] J. Javaloyes. "Cavity Light Bullets in Passively Mode-Locked Semiconductor Lasers". In: *Phys. Rev. Lett.* 116 (4 2016), p. 043901. DOI: https://doi.org/10.1103/PhysRevLett.116.043901.

[10] Kçstutis Staliūnas and Victor J. Sánchez-Morcillo. *Transverse Patterns in Nonlinear Optical Resonators*. First Edition. Springer Berlin, Heidelberg, 2003. DOI: https://doi.org/10.1007/3-540-36416-1.

[11] Magnus Karlsson and Anders Höök. "Soliton-like pulses governed by fourth order dispersion in optical fibers". In: *Optics Communications* 104.4 (1994), pp. 303–307. ISSN: 0030-4018. DOI: https://doi.org/10.1016/0030-4018(94)90560-6.

[12] Kevin K. K. Tam et al. "Generalized dispersion Kerr solitons". In: *Phys. Rev. A* 101 (4 2020), p. 043822. DOI: https://doi.org/10.1103/PhysRevA.101.043822.

[13] D. Maas et al. "MIXSELs - a new class of ultrafast semiconductor lasers". In: (2007). DOI: https://doi.org/10.1109/CLEOE-IQEC.2007.4386010.

[14] Orazio Svelto. *Principles of Lasers*. Fifth Edition. Springer New York, NY, 2010. DOI: https://doi.org/10.1007/978-1-4419-1302-9.

[15] H.A. Haus. "Mode-locking of lasers". In: *IEEE Journal of Selected Topics in Quantum Electronics* 6.6 (2000), pp. 1173–1185. DOI: https://doi.org/10.1109/2944.902165.

[16] Jan Hausen et al. “How carrier memory enters the Haus master equation of mode-locking”. In: *Opt. Lett.* 45.22 (2020), pp. 6210–6213. DOI: https://doi.org/10.1364/OL.406136.

[17] P. Camelin et al. “Electrical addressing and temporal tweezing of localized pulses in passively-mode-locked semiconductor lasers”. In: *Phys. Rev. A* 94 (6 2016), p. 063854. DOI: https://doi.org/10.1103/PhysRevA.94.063854.

[18] Christian Schelte et al. “Dispersive Instabilities in Passively Mode-Locked Integrated External-Cavity Surface-Emitting Lasers”. In: *Phys. Rev. Appl.* 13 (5 2020), p. 054050. DOI: https://doi.org/10.1103/PhysRevApplied.13.054050.

[19] C. Palma and V. Bagini. “Extension of the Fresnel transform to ABCD systems”. In: *J. Opt. Soc. Am. A* 14.8 (1997), pp. 1774–1779. DOI: https://doi.org/10.1364/JOSAA.14.001774.

[20] G. New. “Pulse evolution in mode-locked quasi-continuous lasers”. In: *IEEE Journal of Quantum Electronics* 10.2 (1974), pp. 115–124. DOI: https://doi.org/10.1109/JQE.1974.1145781.

[21] S. V. Gurevich and J. Javaloyes. “Spatial instabilities of light bullets in passively-mode-locked lasers”. In: *Phys. Rev. A* 96 (2 2017), p. 023821. DOI: https://doi.org/10.1103/PhysRevA.96.023821.

[22] Bernd Krauskopf, Hinke M. Osinga, and Jorge Galán-Vioque. *Numerical Continuation Methods for Dynamical Systems*. First Edition. Understanding Complex Systems. Springer Dordrecht, 2014. DOI: https://doi.org/10.1007/978-1-4020-6356-5.

[23] Rüdiger Seydel. *Practical Bifurcation and Stability Analysis*. Third Edition. Interdisciplinary Applied Mathematics. NY: Springer New York, 2012. DOI: https://doi.org/10.1007/978-1-4419-1740-9.

[24] The MathWorks Inc. *MATLAB version: 9.13.0 (R2022b)*. Natick, Massachusetts, United States, 2022. URL: https://www.mathworks.com.

[25] Hannes Uecker, Daniel Wetzel, and Jens D. M. Rademacher. “pde2path - A Matlab Package for Continuation and Bifurcation in 2D Elliptic Systems”. In: *Numerical Mathematics: Theory, Methods and Applications* 7.1 (2014), 58–106. DOI: https://doi.org/10.1017/S1004897900000295.

[26] Dietrich Braess. *Finite Elements*. Third Edition. Cambridge University Press, 2007. DOI: https://doi.org/10.1017/CBO9780511618635.

Declaration of Academic Integrity

I hereby confirm that this thesis, entitled Dynamics of transversal patterns in optical micro-cavities is solely my own work and that I have used no sources or aids other than the ones stated. All passages in my thesis for which other sources, including electronic media, have been used, be it direct quotes or content references, have been acknowledged as such and the sources cited. I am aware that plagiarism is considered an act of deception which can result in sanction in accordance with the examination regulations.

_____
(date, signature of student)

I consent to having my thesis cross-checked with other texts to identify possible similarities and to having it stored in a database for this purpose.

I confirm that I have not submitted the following thesis in part or whole as an examination paper before.

_____
(date, signature of student)